STUDY OF BROADBAND PLANAR DUAL-POLARIZATION ANTENNAS FOR WIRELESS COMMUNICATIONS

TERENCE SEE SHIE PING
(B. Eng. (Hons), NUS)

A THESIS SUBMITTED

FOR THE DEGREE OF MASTER OF ENGINEERING

DEPARTMENT OF ELECTRICAL AND COMPUTER ENGINEERING

NATIONAL UNIVERISTY OF SINGAPORE

2004

ACKNOWLEDGEMENTS

I would like to express my sincere gratitude to my supervisors, Dr. Chen Zhi Ning, from the Institute for Infocomm Research (I^2R), and Prof. Li Le-Wei from the National University of Singapore (NUS), for their guidance throughout the duration of my research as well as in giving me the opportunity to pursue such a challenging research topic. Also, I would like to thank Mr. Abdul Jalil from the Electrical and Computer Engineering Department, NUS, for assisting me with the fabrication of the antennas.

I greatly appreciate the tremendous support from my family, colleagues and friends who have inspired and helped me in one way or another in making this research project a success.

CONTENTS

SUMMARY

In this Thesis, various designs of stacked planar elements and arrays with dual-linear polarization characteristics were presented. The stacked configuration has been chosen to increase the bandwidth of the designs. The designs satisfy the requirements for a base station and capable of having a broad bandwidth for the VSWR ≤ 1.5, covering the 2.4GHz ISM band. The measured radiation patterns of the element and arrays have exhibited dual-linear polarization characteristics, with high front-to-back radiation ratios, stable gain, and almost unchanging half-power beamwidth across the well-matched bandwidths. An alternative array structure that makes use of the offset patches coupled to the radiating patch has been proposed. A prototype was fabricated for testing based on the optimised values from simulations. The losses due to the feeding network have been significantly reduced due to its simplicity. The measured radiation patterns have demonstrated the stable, symmetrical, and $\pm 45^{o}$-linear polarization characteristics with the absence of side-lobes as well as high front-to-back radiation ratios.

In order to combat multipath fading and improve overall system performance, diversity techniques are implemented through the use of additional antennas. In this Thesis, the polarization diversity performances of microstrip patch antennas were investigated. The diversity performance was evaluated based on the far-field coupling or orthogonality, output power correlation coefficient, as well as the diversity gain. The far-field coupling was calculated by using the amplitudes of the vertically and horizontally polarized far-field radiation levels. The output power correlation takes into account the effect of the cross-polar discrimination which has been shown in this Thesis to be primarily dependent on the antenna design, and not only on the fading

channel characteristics. The received signals from the branches are processed using maximal ratio combining (MRC). The diversity gain was calculated based on the cumulative distribution function for two-branch MRC at a 99% reliability, with reference to a vertically polarized antenna.

In this Thesis, the stacked and gap-coupled configurations of a polarization diversity antenna were presented. Good consistency with the simulation results at the lower, center, and upper frequencies of the bandwidth has been achieved. For the stacked configuration, degradation in the diversity gain occurs at the upper frequency but is still capable of achieving good diversity gain of at least 5dB within a 120° sector. In order to examine the effects of cross-polar discrimination brought about by the antenna design, ideal channel conditions with the absence of fading and multipath effects have been assumed. For the gap-coupled antennas, the diversity gain coverage is wider than the stacked configurations. It has been found to be easier to perform impedance matching for the suspended gap-coupled antenna, which is capable of achieving a good diversity gain within a 140° coverage. Another distinct advantage of using the suspended gap-coupled antenna is that the diversity gain does not degrade at the higher frequency of the impedance bandwidth.

LIST OF SYMBOLS AND ABBREVIATIONS

E	electric field
HPBW	half-power beamwidth
SNR	signal-to-noise ratio
VSWR	voltage standing wave ratio
V	voltage
I	current
ζ_0	intrinsic impedance in free space
k_0	propagation constant in free space
λ_0	operating wavelength in free space
σ	far-field coupling
ρ	output power correlation coefficient
χ	cross-polar discrimination
Γ	average signal-to-noise ratio
ε_r	relative permittivity
x	rectangular coordinate
y	rectangular coordinate
z	rectangular coordinate
θ	azimuth
ϕ	azimuth

LIST OF FIGURES

LIST OF TABLES

Chapter 1

INTRODUCTION

1.1 Background

Over the recent years, one of the advances in wireless communications is the introduction of new wireless protocols for indoor communications such as the Bluetooth [Haa00], IEEE 802.11b, and wireless local area network (WLAN) have brought about great challenges to antenna designs. Both the WLAN and Bluetooth utilize the industrial, scientific and medical (ISM) frequency band of 2.4GHz – 2.485GHz. The IEEE 802.11b specification sets up 11 channels within the 2.4GHz band, centered between 2.412GHz and 2.462GHz. Besides the WLAN and Bluetooth technology, the introduction of the third generation (3G) cellular services known as Universal Mobile Telecommunications System (UMTS) or IMT-2000 has sustained higher data rates of up to 2Mbps in a fixed or stationary wireless environment and 384Kbps in a mobile environment, thereby opening the door to many internet style applications.

As microstrip antennas in their basic forms are known to have narrow bandwidth and low efficiency, bandwidth enhancement techniques are developed. Typically, one can either excite several resonant modes of a single patch or use several radiating structures closely coupled to each other but resonating slightly at different frequencies by using stacked [Smi87][Lee90][Cro90][Cro91][Ven98] or parasitic patches [Sch79][Kum84] [Kum85][Pri85][Aan86] that are incorporated in the designs of the antennas. Other factors that are to be taken into consideration in the designs of WLAN

base station antennas include the gain, beamwidth, and front-to-back ratio. A typical base station antenna has a gain of less than 22dBi, with a minimum half-power beamwidth (HPBW) of 30° in both E and H planes and a front-to-back ratio greater than 20dB. In order to achieve these, arrays could be used as the gain need to be increased with a corresponding reduction in the HPBW as compared to the single patch element [Leg94].

In the design of base station antennas, the demand for good spectrum efficiency in narrow band systems can be eased by the application of antenna diversity. Diversity exploits the random nature of radio propagation by finding independent signal paths for communication. By having more than one channel to select from, both the instantaneous and average signal to noise ratios (SNRs) at the receiver may be improved by as much as 20dB to 30dB. The need to improve the SNR arises from the fact that the radio path from the mobile to the base station is often physically blocked by buildings, trees, and other terrain features. As a mobile user moves through the environment, the signal received at the base station varies with time as the amplitudes and phases of the directly received signal and multiple reflected signal change. For a certain proportion of time, the received signal may fall to an unacceptably low level and the resulting increase in bit error rate (BER) will cause a loss of effective communication.

Diversity possibilities for counteracting short-term fading effects were first experimented using spaced receiving antennas. By having sufficient spacing of several wavelengths between antennas, the short term fading fluctuations of the signal received at one antenna tend to be independent of the fluctuations of the signal

received on the other antennas [Lee71][Lee73][Rhe74]. However, over the years, other mechanisms for achieving independently fading signals have been examined in depth. These include frequency, angle, polarization and time diversity. Of these, there has been an increasing interest in polarization diversity systems [Lee72][Wah97][Lem98] because as compared to space diversity, the two receiving antennas can be physically co-located. This results in cost-savings and a smaller visual profile for the base station. The methods to combine the signals in the branches include selection, equal gain, switched and maximal ratio combining [Bre59][Vau90][Egg93][Lot96]. Maximal ratio combining has been known to be the most effective method in a multipath environment, as it makes optimal use of the total signal power received in the branches at any instant.

Therefore, in the design of a polarization diversity antenna for base station applications, besides characterizing the performance in terms of the return loss at each port, the port isolation and the power in both the vertical and horizontal polarizations, it is also important to examine three parameters that will determine the overall diversity performance of the antenna. First, the far-field coupling or orthogonality describes the difference between the horizontal and vertical polarized powers. Second, the output power correlation, which is a function of the cross-polarization discrimination and the far-field coupling, describes the degree, which the two signals are correlated. Third, the diversity gain is the improvement in SNR in a Rayleigh fading or non-fading channel.

1.2 Motivation

Dual-polarized antennas are useful as they can receive both horizontally and vertically polarized signals, especially in a multipath environment, where the presence of scatterers causes the depolarization of the vertically polarized transmitted signals. Also, changes in the orientation of the mobile will change the transmitted polarization as well. On the other hand, microstrip antenna designs suffer from the narrow bandwidth. Therefore, in the design of dual-polarized patch antennas, it will be necessary to broaden the impedance bandwidth. By using stacked patches, the bandwidth can be enhanced since the presence of the top substrate layer reduces the Q-value. Therefore, by implementing the stacked configuration in dual-polarized antennas, the antennas can be designed to cover the desired bandwidth.

In environments where there are many obstacles, the coverage of the antennas will be reduced. As such, it will be necessary to increase the gain (or directivity) by forming an array. In this work, the stacked single element design will be extended to include a two-element linear array as well as a 2×2 planar array. Most of the previous literatures on antenna designs evaluate the radiation performance only at the center frequency. However, the radiation patterns at the upper frequency may be seriously degraded due to the distortion of the current distributions. In order to ensure that the radiation patterns for both the vertical and horizontal polarizations are acceptable, especially at the upper frequency, the radiation patterns will be analyzed at three frequencies corresponding to the lower, center, and upper frequencies of the impedance bandwidth.

Arrays often face the disadvantages of having high fabrication cost and considerable losses caused by the feeding network. In order to minimize the losses from the feeding network, offset patches have been used [Leg94][Raj02]. Besides having a simple feeding network, other benefits such as increased gain and impedance bandwidth can be obtained. Therefore, a stacked offset array, capable of dual-polarization operation, will be proposed and analyzed in this Thesis and compared with the other array designs. As an example, the antennas are designed to operate in the 2.4GHz ISM band. The simulations are carried out using the commercial EM simulator Ansoft Ensemble based on the Method of Moments (MoM).

In indoor or outdoor environments where there is a blocked line of sight, the use of dual-polarization antennas with a single feed configuration will not be efficient since if a signal experiences deep fading, the message will be decoded wrongly and the communication quality will be greatly reduced. Although the transmit power can be increased at times when a low signal strength is received, most wireless communication systems are low in power and unable to counter the fading effects. As such, an increase in reliability can be achieved with diversity by having two or more ports. In this Thesis, the two-branch polarization diversity for two antenna configurations, namely the stacked and gap-coupled configurations will be examined. As an example, the stacked configuration has been designed to operate at 1.98GHz and the gap-coupled configuration at 2.4GHz. The simulations for the polarization diversity antennas are carried out using the commercial EM simulator Zeland IE3D based on the MoM.

The performance of a diversity antenna is dependent on the combining technique used. In this work, the maximal ratio combining will be chosen since it provides the greatest

improvement in signal-to-noise ratio. The diversity performance of the antenna will be assessed in terms of the far-field coupling, output power correlation coefficient, as well as the diversity gain. The calculations will be performed using the simulated and measured amplitudes of radiation patterns. An interesting point to note is that, the cross-polar discrimination, which is the ratio between the vertical and horizontal polarizations, is often regarded to be primarily dependent on the fading channel characteristics. However, this study seeks to examine the influence of the antenna design on the cross-polar discrimination. In order to do so, the measurements on the radiation will be conducted in an anechoic chamber, where multipaths are absent.

1.3 Scope

The organization of the Thesis can be divided into six chapters. The designs and measurements of the single-feed dual-polarized patch element as well as arrays for WLAN applications are documented in Chapter 2. In Chapter 3, the definitions and concepts of diversity systems used in the later chapters of this Thesis are introduced. The various combining techniques used to process the received signals are examined. In Chapter 4, a mathematical formulation of the various diversity parameters used in the analysis of the diversity performance of the antennas is presented. In addition, the chapter details the designs and performance analysis of the stacked ±45°-polarized antennas for 3G and WLAN applications. With the measured and simulated radiation patterns, the calculated diversity performances of the gap-coupled ±45°-polarized antennas across the impedance bandwidth are detailed in Chapter 5. Finally, Chapter 6 summarizes the results presented in this Thesis.

Chapter 2

DESIGN OF STACKED PATCH ANTENNAS

2.1 Introduction

Wireless networking uses radio frequencies originally set aside for unlicensed "Industrial Scientific and Medical" (ISM) use. There are three bands: 902MHz – 928MHz, 2400MHz – 2483.5MHz, and 5725MHz – 5850MHz. The two wireless systems that have experienced the most rapid evolution and popularity are the wireless local area networks (WLANs), identified as IEEE 802.11b and Bluetooth technology for wireless personal area networks (WPANs).

WLANs are designed to cover large areas such as buildings or offices. The basic service set (BSS) is the fundamental block of the network, comprising of several wireless stations and one fixed access point. The access point provides connection to the wired network [Cro97]. WLANs operate at bit rates as high as 11Mb/s and uses either frequency hopping spread spectrum (FHSS) or a direct sequence spread spectrum (DSSS). In the case of FHSS systems, hopping sequences span over 79 channels while DSSS systems use an 11-chip Barker sequence and the bandwidth is about 20MHz [Kam97].

Bluetooth is a technology specification designed to eliminate the cables and infrared links used to connect disparate devices. Its aim is to provide small design, low-cost, short-range wireless interconnectivity between mobile phones, laptop computers,

digital cameras, etc. It also enables close-range applications in public areas like e-cash transactions. It is based on low-power radio frequency technology using 2.4GHz spectrum with a power level of 10mW, the bit rate is almost 1Mb/s and the coverage range is about 10m. The technology enables the users to connect to a wide range of computing and telecommunication devices easily without the need to carry and connect cables.

The tremendous demand generated over the years for WLANs and Bluetooth has renewed interests in both PCMCIA cards in portable devices and base station antenna designs, especially at the ISM bands. In this Chapter, four dual-linear polarization antenna configurations, designed to operate in the 2.4GHz ISM band for base station applications will be presented. The base station antenna specifications are shown in Table 2.1.1.

Table 2.1.1: Base station specifications

Frequency	2400MHz – 2485MHz
VSWR	≤ 1.5:1
Impedance	50Ω
Gain	< 22dBi
Front-to-back ratio	> 20dB
Power rating	100W
E-plane HPBW (min.)	8 – 30°
H-plane HPBW (min.)	30 – 70°
Polarization	Dual-linear

2.2 Antenna Designs for WLAN/Bluetooth Base Stations

In this section, the concept of dual-linear polarization will be defined. Some common techniques to realize dual-linear polarization characteristics and their feed methods will be discussed. The use of stacked patches to enhance the bandwidth will also be briefly introduced.

2.2.1 Dual-linear Polarization Techniques

When a signal illuminates on an object, it is reflected and its polarization is scattered. In most environments, there exists a mixture of horizontally and vertically polarized signals. Hence, it will be ideal if the designed antenna is able to have dual linear polarization characteristics. Surface currents on patch antennas can flow along orthogonal directions, and are therefore able to produce two linearly polarized waves with perpendicular polarization planes. The surface currents in both directions can be simultaneously excited either by a single or dual-feed structure.

Dual linear polarization can be achieved in the following ways:

(i) Corner-fed configuration [Che03][Cru91].

With a single-feed structure, two orthogonal modes of a patch resonating at slightly different frequencies are excited. The cavity model shows that the internal field is the sum of the two degenerate modes with equal amplitudes, i.e. (0,1) and (1,0) [Jam89].

(ii) Dual-feed network configuration [Mat02].

The two polarizations are excited with a dual-feed circuit, using either a connection through pins, direct transmission line feeds on the patch substrate, coupled lines on two sides of the patch or orthogonal coupling slots.

(iii) Array with uniformly spaced elements [Bra95].

Two arrays, each having elements with a single linear polarization is used. The vertical and horizontal polarized elements are interleaved.

For (ii) and (iii), in order for the polarizations to be in phase, the length of the feeding network to the feed point must be kept the same.

2.2.2 Feeding Configurations

The microstrip patch can be fed by using a slot feed (aperture feed) or a stripline feed. When using the slot feed, the slot cut on the ground plane must be non-resonant to avoid spurious radiation towards the back of the antenna, resulting in high front-to-back ratios. The structure is more complex to fabricate as it involves two dielectric layers bonded on both sides of a conductor. However, there is no need to drill holes in the dielectric or to solder conducting wires. This feed method of feeding is popularly used in antenna designs as the bandwidth can be increased.

Alternatively, the stripline feed is the simplest feed method and is conducive to array designs. Impedance matching can be achieved by cutting an inset in the patch hence eliminating the need for additional matching elements. However, the bandwidth is not

as broad as the aperture feed. Therefore, bandwidth enhancement techniques are often used in conjunction with stripline feed.

2.2.3 Stacked Patches

One of the ways to increase the bandwidth is through the use of stacked patches [Smi87][Cro90][Cro91][Tsa98][Ven98]. The stacked patches can be broadly classified into two types:

(i) Normal configuration – The patch of the top layer is exposed to air.

(ii) Inverted configuration – The patches of the top and bottom layer are facing each other. The bandwidth is broader as compared to the normal configuration mentioned in (i), where the presence of the top substrate layer increases the Q-value of the antenna.

The parameters of interest include the sizes of the top and bottom patches, the thickness, the spacing between the dielectric as well as the type of dielectric used. Broad bandwidths can be achieved by adjusting the spacing between the dielectric.

The choice of feed is an important consideration for the stacked patch antenna design. Besides the slot feed and stripline feed, stacked antenna designers also use the coaxial feed method. This feed method minimizes the intrinsic radiation from the coaxial feed and can be neglected for thin substrates but it becomes significant as the substrate gets thicker. It also requires delicate operations that require careful handling as holes need to be drilled through the substrate, especially for high frequencies.

With the understanding of the various dual-polarization techniques as well the design of stacked patch antennas, a prototype with a microstrip line feed and inverted stacked configuration was designed, simulated, and tested. The measurement results are presented in the next section. Here, it must be noted that the finite size of the ground plane and dielectric substrate may bring about a disparity in the results obtained from simulations and measurements. The simple patch element design makes it easier for the implementation of arrays in order to enhance the gain and further improve the front-to-back ratio. Furthermore, the design can be extended to dual-feed dual linear polarization antenna with good isolation characteristics.

2.3 Single Patch Element

In this section, the analysis of the dual-linear polarization stacked element is presented. The geometry and measurement results of the antenna are provided in Sections 2.3.1 and 2.3.2, respectively.

2.3.1 Geometry

The design consists of two layers of dielectric, the bottom layer is made up of a 60mil-thick substrate (Rogers 4003, $\varepsilon_r = 3.38$) having dimensions of 100mm × 100mm. The top layer is made up of a 60mil-thick substrate (FR4, $\varepsilon_r = 4.4$) and having dimensions of 100mm × 100mm. The bottom of the Rogers 4003 substrate is entirely covered with foil and grounded. Two square patches are, respectively, etched onto the bottom of the top layer and the top of the bottom layer. The spacing between the two layers of dielectric supported by four plastic stands is *h* and the two concentric patches are

parallel to, and facing each other as shown in Fig. 2.3.1. The dimensions for the top ($l_t \times l_t$) and the bottom ($l_b \times l_b$) patches are selected such that the resonances occur within the 2.4GHz ISM band. The lower patch is diagonally fed at the corner by a 50Ω microstrip line of a 3.45-mm width.

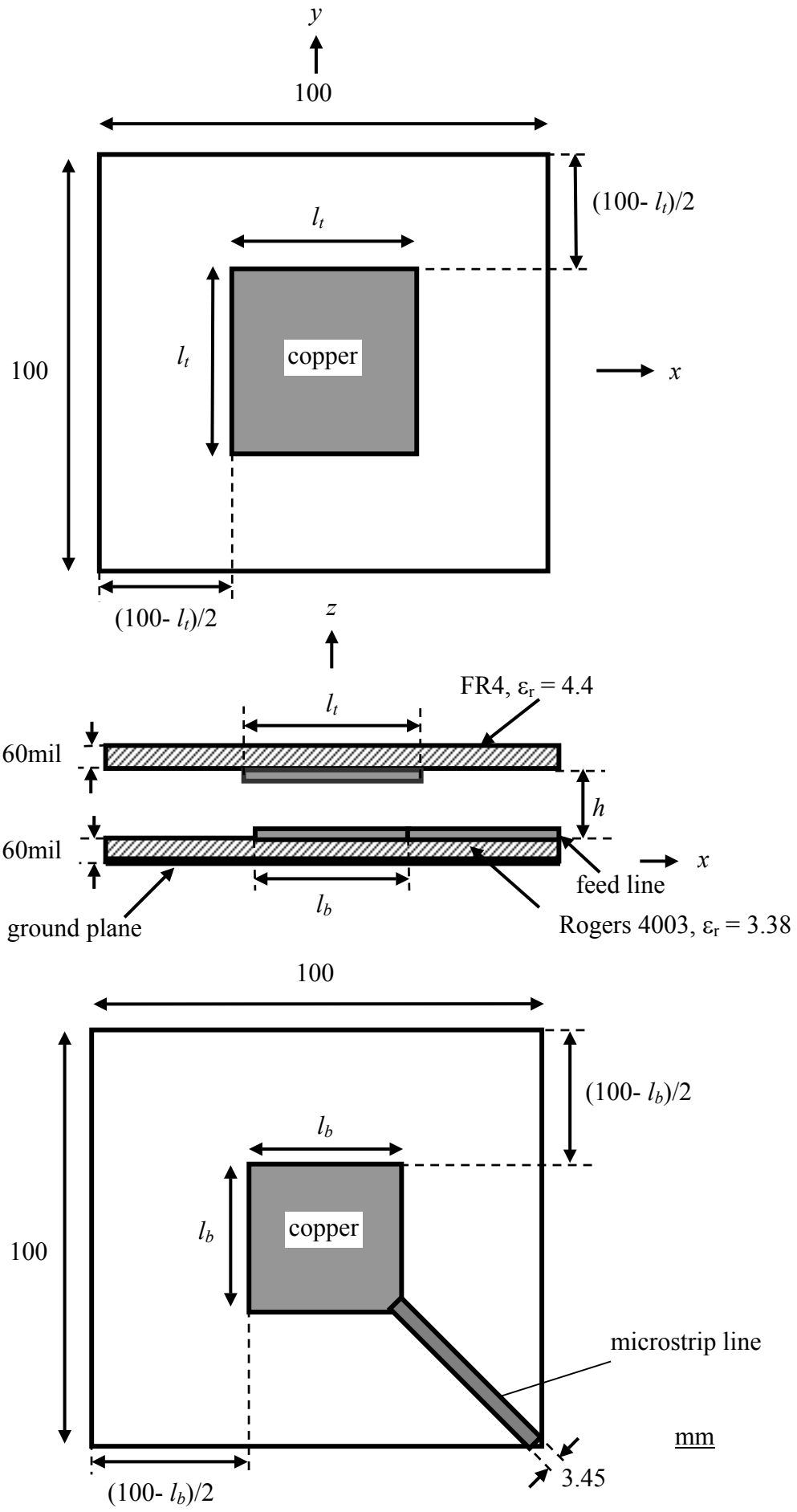

Fig. 2.3.1: Geometry of a stacked patch antenna

2.3.2 Measured Results

The input impedance was measured by an HP8753D Network Analyzer. Fig. 2.3.2 shows the measured VSWR for the proposed antenna. The optimised antenna configuration occurs when l_t = 40mm, l_b = 33mm, and h = 8mm. The measured results show that the antenna achieves a 1.5:1 VSWR bandwidth of 13% at a center frequency of 2.45GHz, covering the whole 2.4GHz ISM band well.

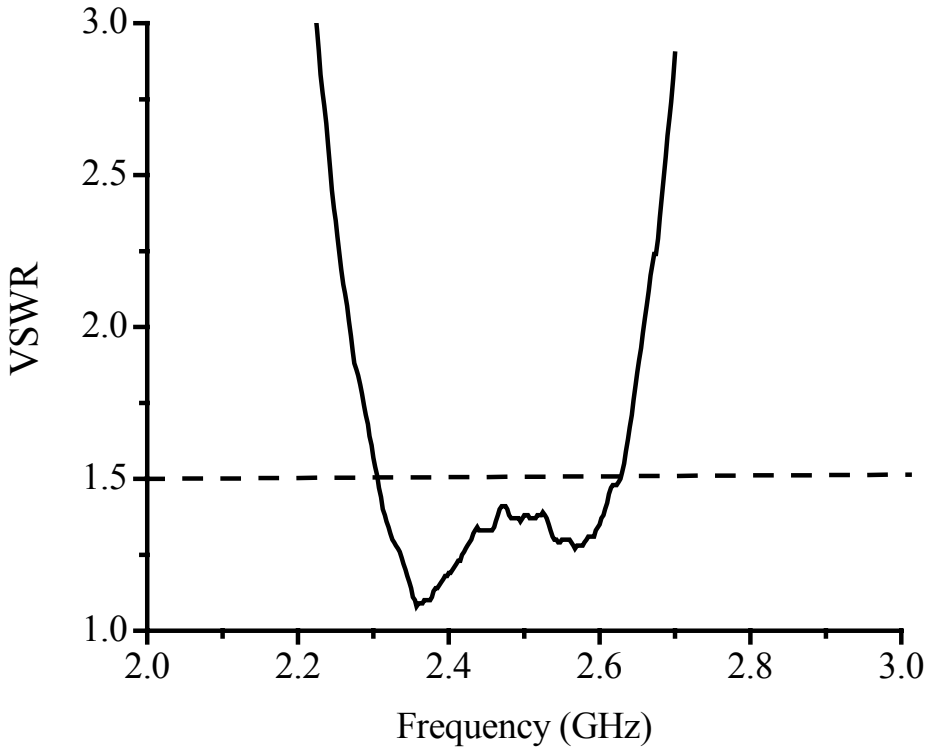

Fig. 2.3.2: Measured VSWR

The radiation patterns were then measured in an anechoic chamber at three primary frequencies, namely, 2.4GHz, 2.45GHz, and 2.5GHz. Figs. 2.3.3 – 2.3.6 display the patterns in the *x*-*z* and *y*-*z* planes. In each plane, the radiation level at each frequency was normalized by the maximum value.

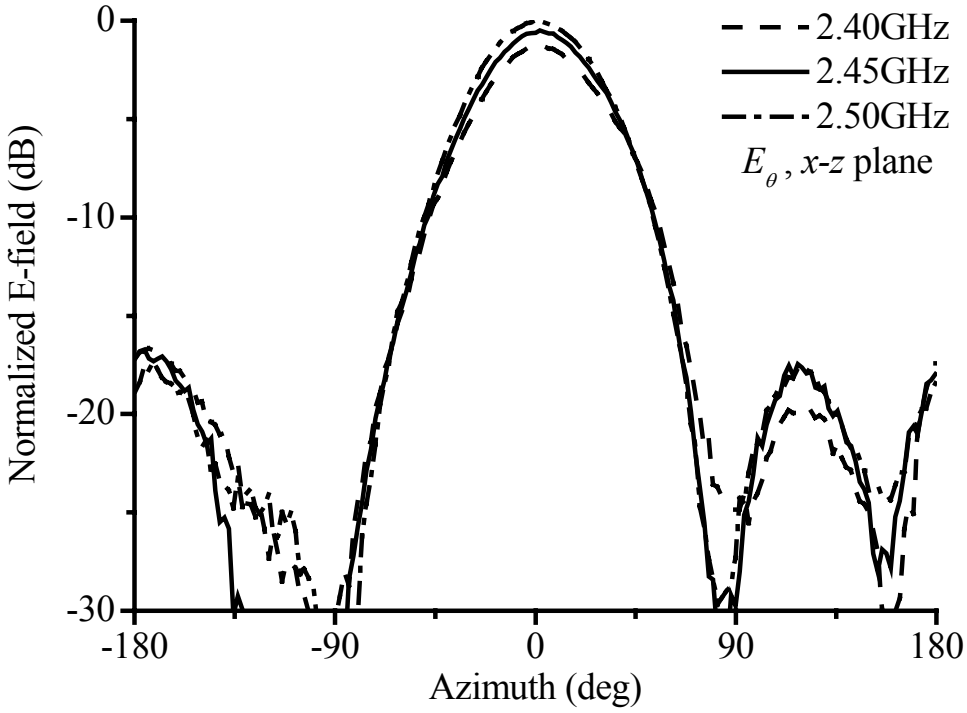

Fig. 2.3.3: Measured E_θ in the *x-z* plane

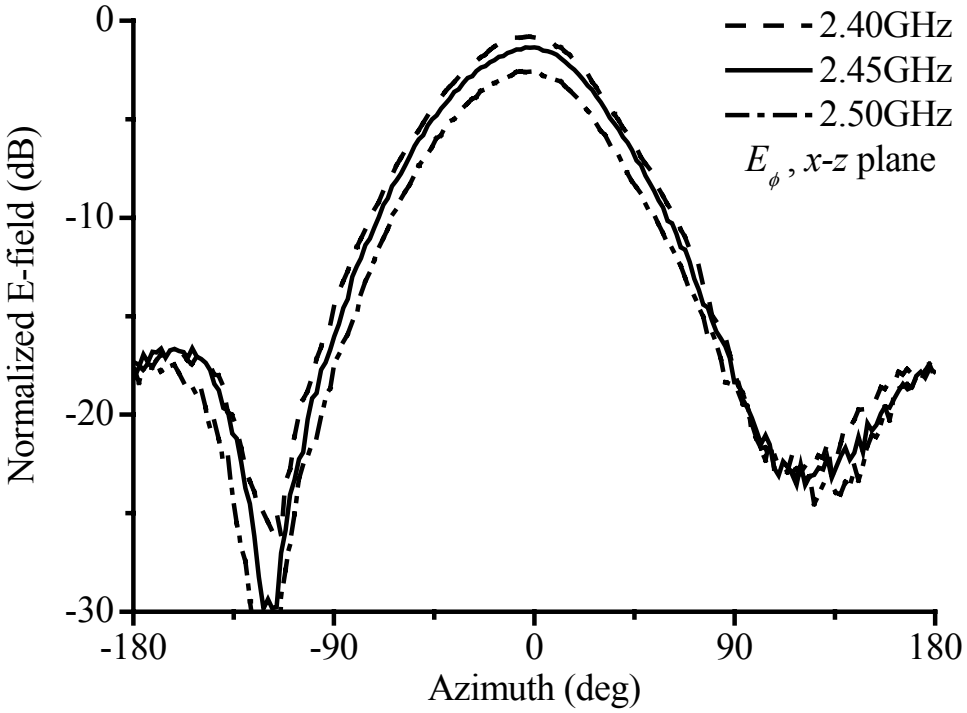

Fig. 2.3.4: Measured E_ϕ in the *x-z* plane

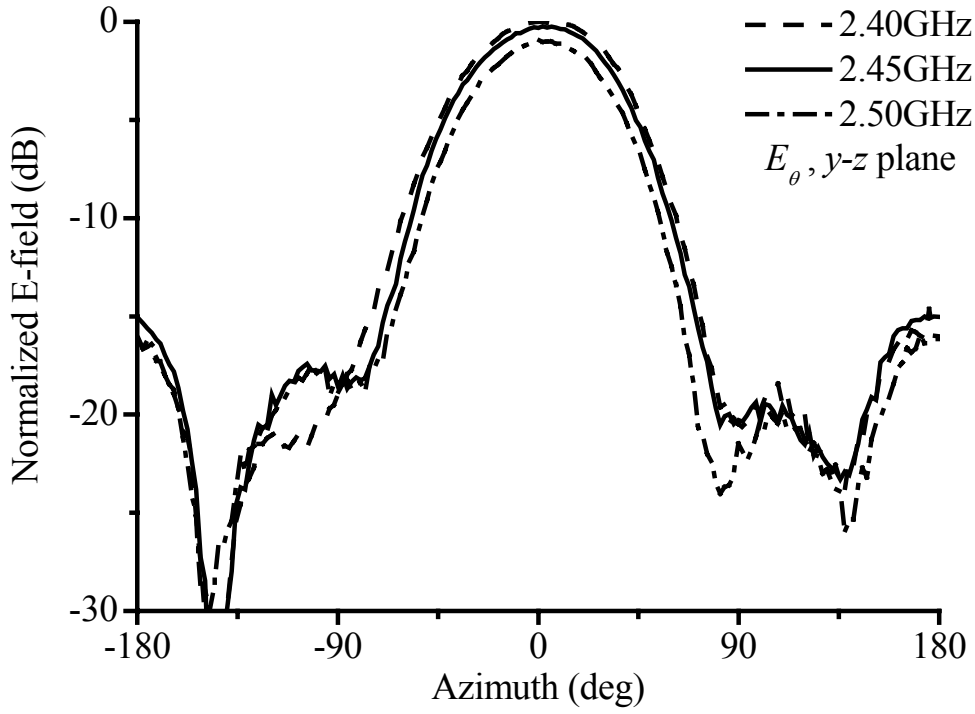

Fig. 2.3.5: Measured E_θ in the *y*-*z* plane

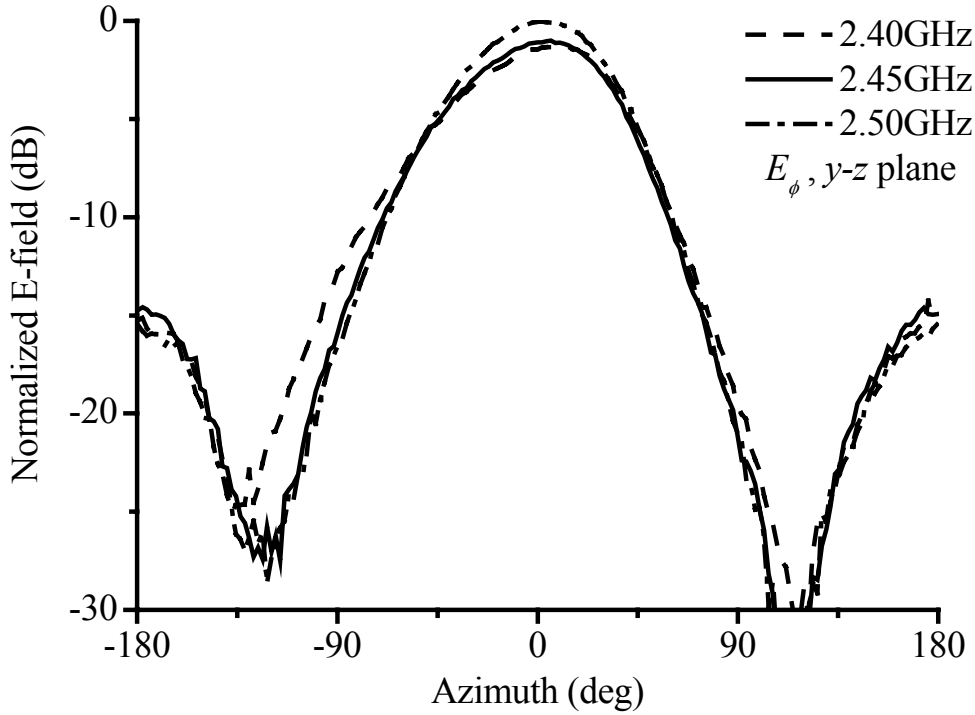

Fig. 2.3.6: Measured E_ϕ in the *y*-*z* plane

In the *x-z* plane, the difference between the E_θ and E_ϕ components at the boresight generally increases with frequency, and is generally less than 2.8dB. However, this difference is less than 1.4dB in the *y-z* plane. In the planes of interest, the radiation patterns for each of the E_θ and E_ϕ components are found to be stable with frequency across the azimuth, with a difference of less than 2dB at the boresight. At 2.45GHz, the half-power beamwidth (HPBW) for the E_θ component in the *x-z* plane is 57° and the HPBW for E_ϕ component is 73°. In the *y-z* plane, the HPBW for the E_θ component is 71° and 76° for the E_ϕ component. Due to the finite-size ground plane used in the measurements, the front-to-back ratio in the *x-z* plane is generally greater than 17dB and 15dB in the *y-z* plane. In addition, the measured average gains in both the planes are approximately 6.8dBi.

2.4 Two-element Linear Patch Array

The radiation characteristics of a single element patch antenna have been discussed in the previous section. It can be seen that the radiation pattern of a single element is relatively wide and that the antenna has a low directivity (gain). However, it is necessary to design antennas with high directivity in order to increase coverage, especially in environments with many obstacles. In order to do so, the electrical size of the antenna is increased. Therefore, an array, made up of an assembly of radiating elements in an electrical and geometrical configuration, can be constructed.

In this section, the analysis of a two-element linear array is presented based on the understanding of the stacked element. The geometry as well as the measured

impedance and radiation patterns of the array are provided in Sections 2.4.1 and 2.4.2, respectively.

2.4.1 Geometry

With an understanding of the workings for the stacked dual-polarization single patch element, a two-element stacked linear array antenna was designed as shown in Fig. 2.4.1. The dielectric substrate (200mm × 100mm) used for the bottom layer is Rogers 4003, with a relative dielectric constant of $\varepsilon_r = 3.38$ and a thickness of 60mil. The two layers of the dielectric supported by four plastic stands are separated by h. The two patches ($l_b \times l_b$) on the bottom layer are fed via a feeding network designed for optimal performance. The distance between the center of the patches for the top and bottom layers is d. The network consists of a 50Ω transmission line of a 3.45mm-width connected in parallel to two 100Ω transmission lines of width 0.9mm on either side. A quarter wavelength transformer measuring 17.5mm × 1.9mm is used to transform the impedance to 50Ω and fed diagonally to each patch. Two square patches ($l_t \times l_t$) are etched on the upper patch layer made of FR4, with a dielectric constant of $\varepsilon_r = 4.4$ and a thickness of 60mil.

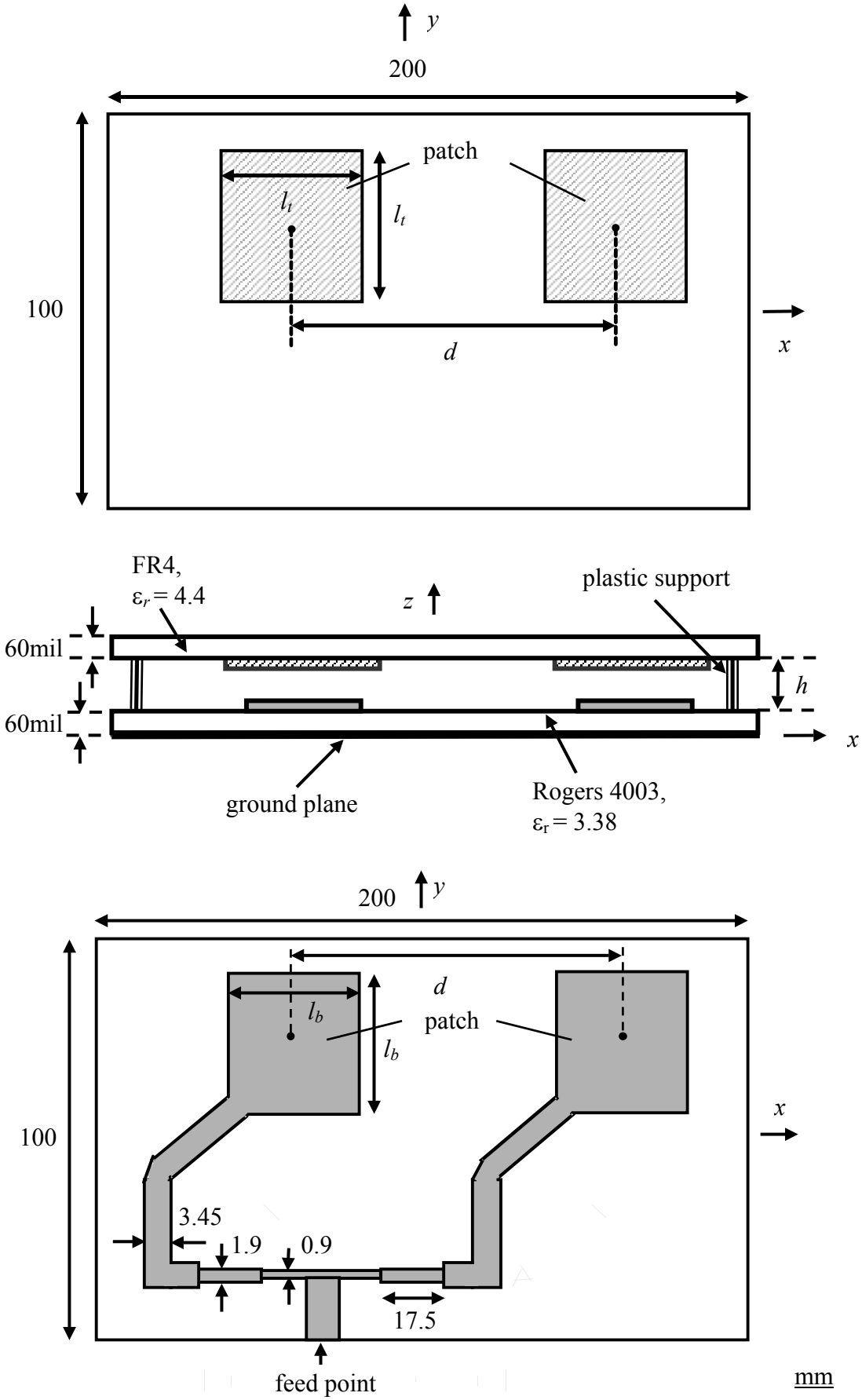

Fig. 2.4.1: Geometry of a two-element linear array

2.4.2 Measured Results

Using an HP8510C Network Analyzer, the input impedance of the array was measured and the VSWR for the proposed array is shown in Fig. 2.4.2. The optimised antenna configuration can be achieved when l_t = 42mm, l_b = 33mm, h = 8.5mm, and d = 60mm. From the measured results, the antenna is able to achieve a 1.5:1 VSWR bandwidth of 13.3% at a center frequency of 2.45GHz.

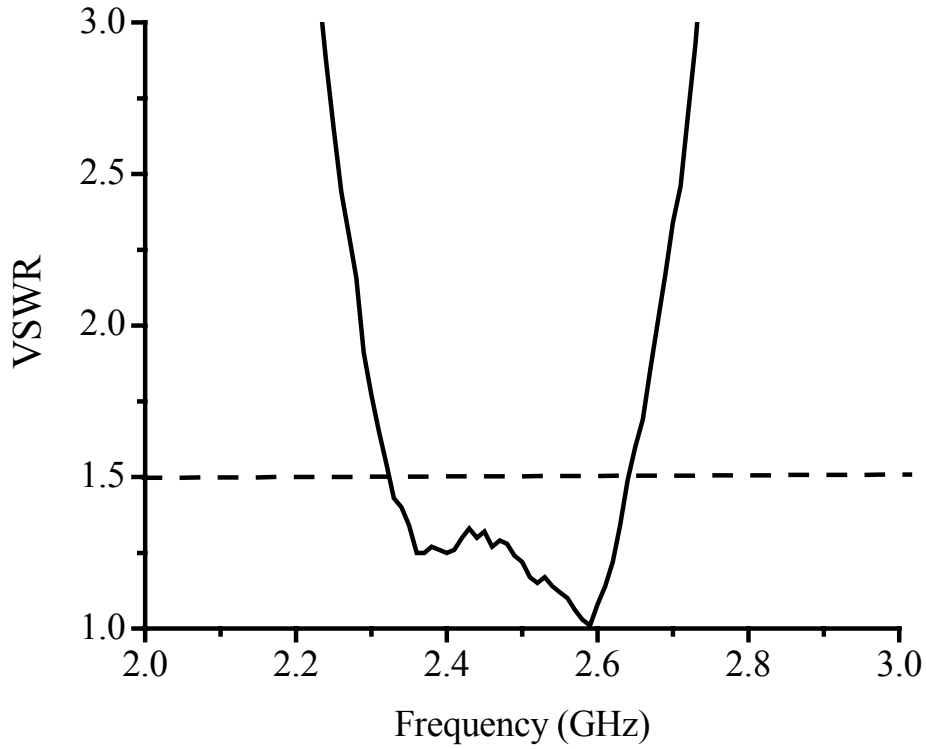

Fig. 2.4.2: Measured VSWR

The radiation patterns were then measured in an anechoic chamber at 2.4GHz, 2.45GHz, and 2.5GHz and their polar plots are shown in Figs. 2.4.3 – 2.4.6 for the *x*-*z* and *y*-*z* planes. In each plane, the normalization of the radiation at each frequency with respect to the maximum radiated component has been performed.

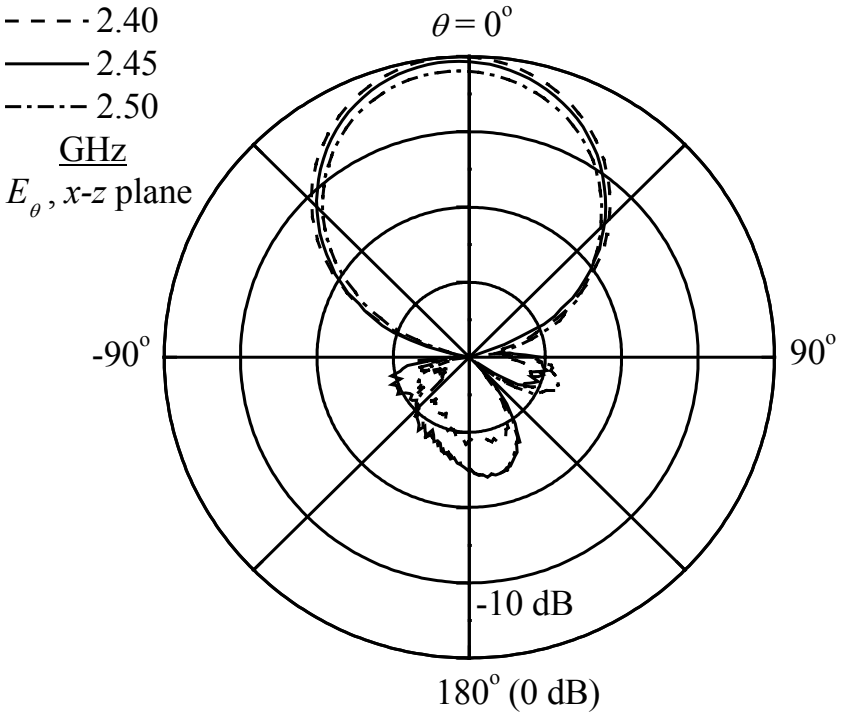

Fig. 2.4.3: Measured E_θ in the *x-z* plane

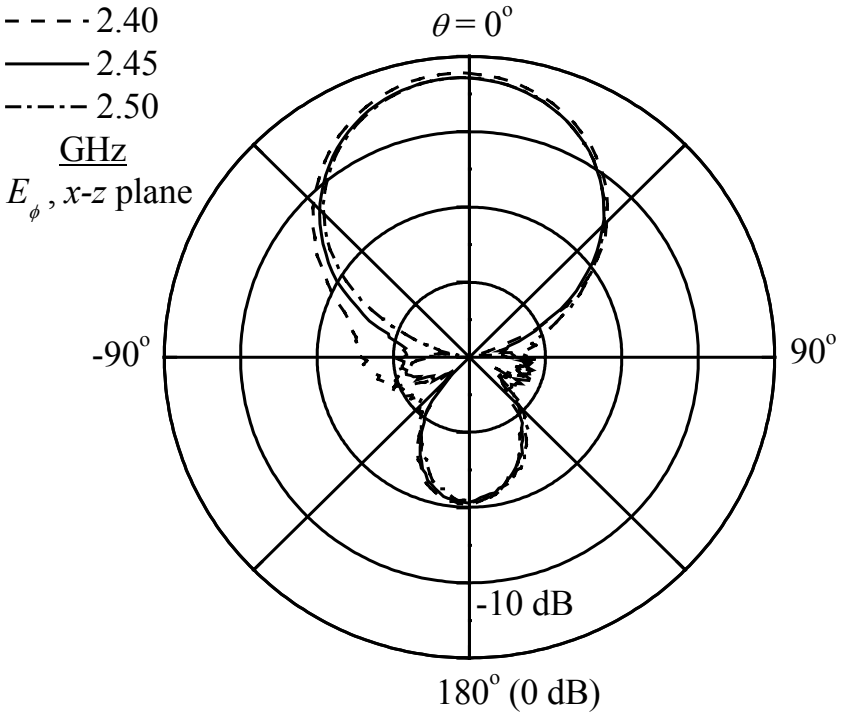

Fig. 2.4.4: Measured E_ϕ in the *x-z* plane

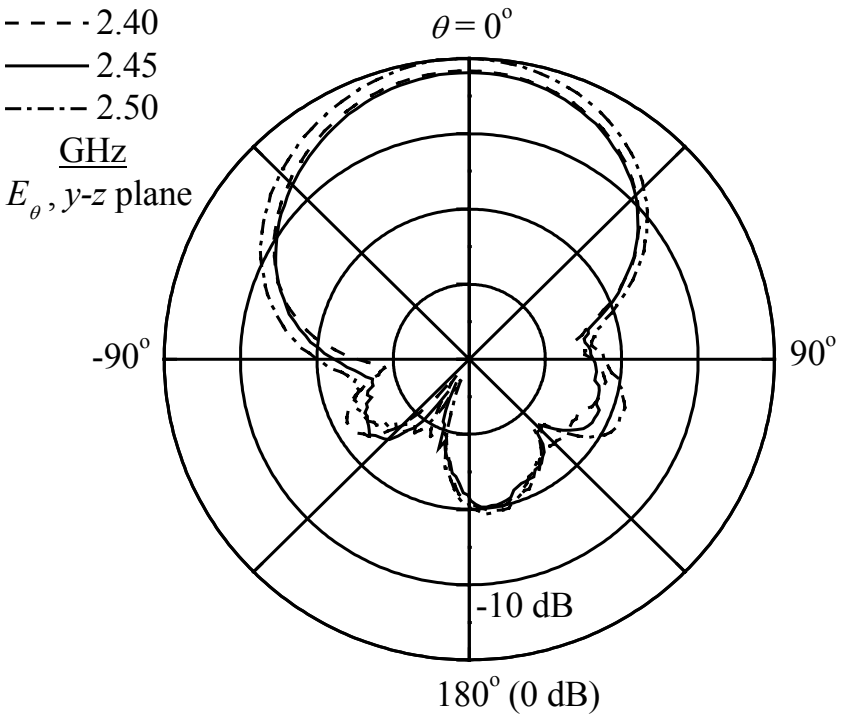

Fig. 2.4.5: Measured E_θ in the *y-z* plane

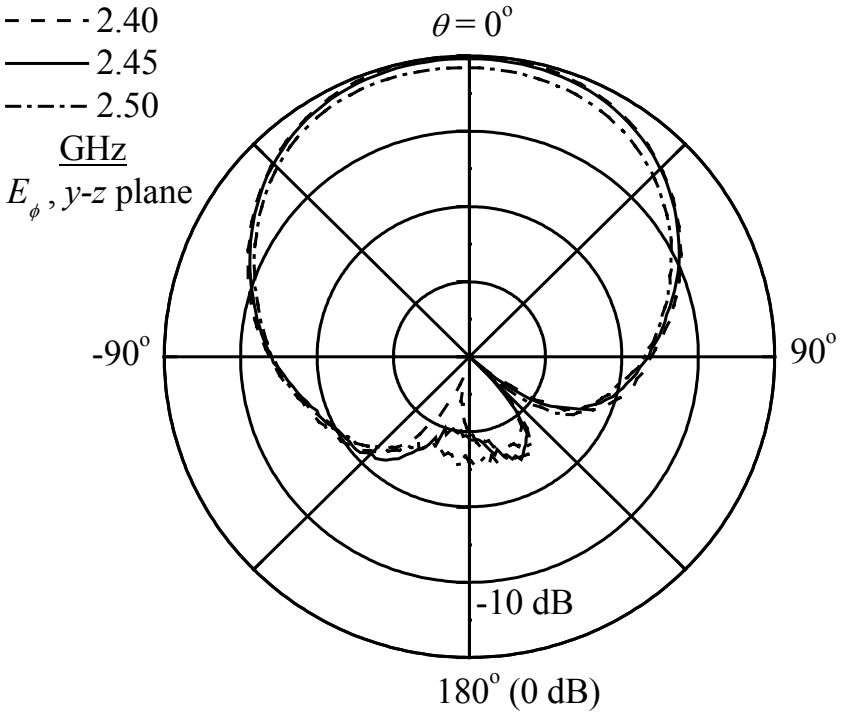

Fig. 2.4.6: Measured E_ϕ in the *y-z* plane

In the *x-z* and *y-z* planes, the variation in the E_θ and E_ϕ components with frequency are found to be less than 2dB. The patterns are symmetrical with the side-lobe levels kept low at –30dB in the *x-z* plane and –22dB in the *y-z* plane. The difference between the E_θ and E_ϕ components at the boresight is generally less than 2.2dB in the *x-z* plane and 1.6dB in the *y-z* plane. For the *x-z* plane, the average HPBW is 46° and 72° in the *y-z* plane at 2.45GHz. The front-to-back ratios in the *x-z* plane are generally greater than 18dB in both the planes which can be further reduced if a larger ground plane was used in the test. In addition, the measured average gains in both the planes are approximately 9dBi.

2.5 2 × 2 Planar Patch Array

Following the design of the two-element linear array, the analysis of the 2 × 2 planar array is presented in this section. The geometry as well as the measured impedance and radiation patterns of the array are provided in Sections 2.5.1 and 2.5.2, respectively.

2.5.1 Geometry

The proposed geometry of the 2 × 2 planar array is shown in Fig. 2.5.1. The bottom layer consists of four patches ($l_b \times l_b$) arranged symmetrically about the *x* and *y*-axes on a 200mm × 200mm ground plane. The upper layer consists of four patches ($l_t \times l_t$) arranged correspondingly in an inverted configuration. The dielectric substrate used for the bottom layer is Rogers 4003 ($\varepsilon_r = 3.38$) and FR4 ($\varepsilon_r = 4.4$) for the upper layer, each with a thickness of 60mil. The two layers of the dielectric are supported by four plastic stands with a separation of *h* between them. The top and bottom two patches

on the bottom layer are each fed via a feeding network designed for optimal performance. The network consists of a 50Ω transmission line of width 3.45mm connected in parallel to two 100Ω transmission lines of width 0.9mm on either side. A quarter wavelength transformer measuring 17.5mm × 1.9mm is used to transform the impedance to 50Ω and then fed diagonally to each patch. A second quarter wavelength transformer measuring 18.3mm × 5.8mm is used to transform the 25Ω line of width 9.2mm to 50Ω before the feed point.

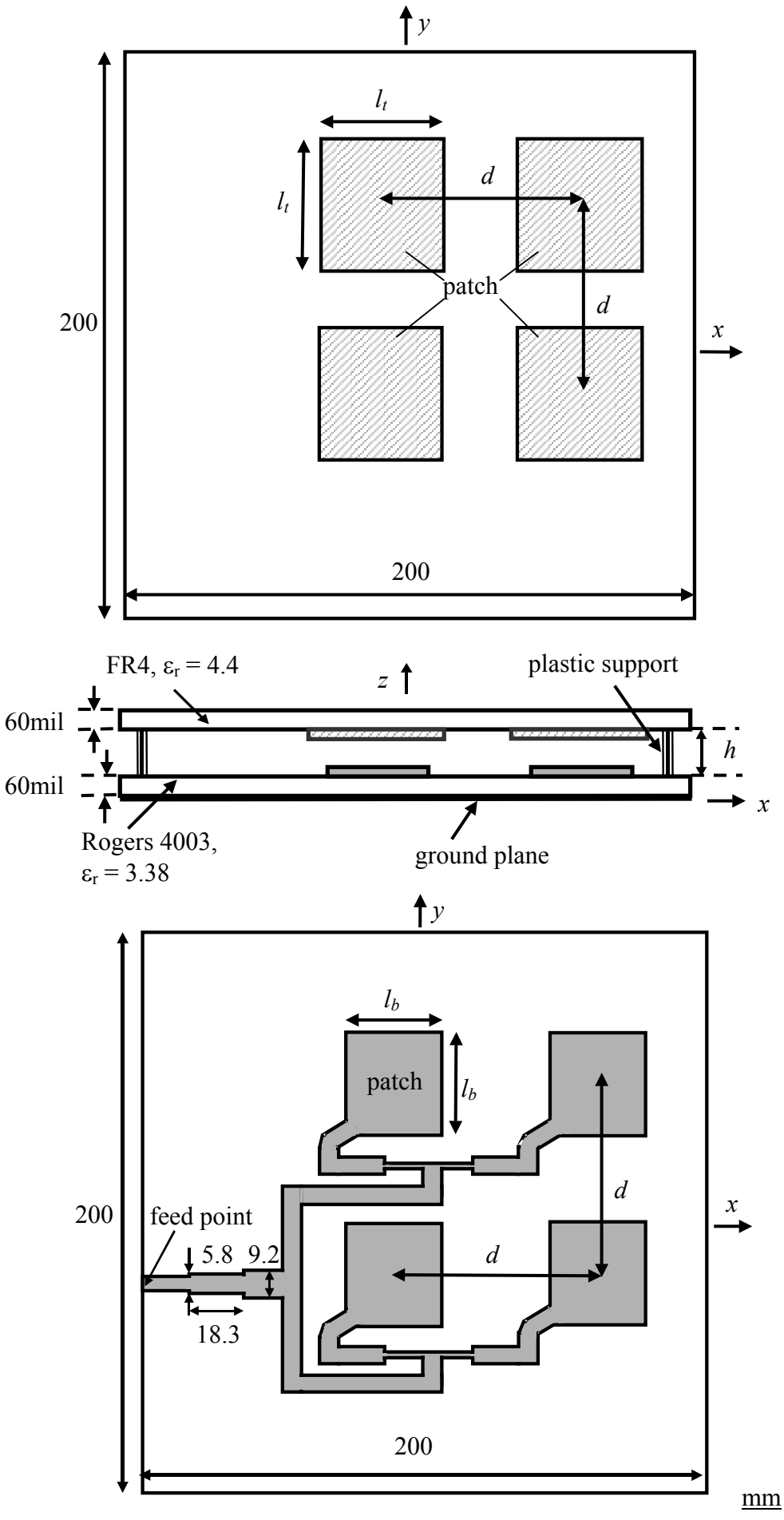

Fig. 2.5.1: Geometry of a 2 × 2 planar array

2.5.2 Measured Results

The impedance performance was measured using an HP8510C Network Analyzer. The measured VSWR for the array is shown in Fig. 2.5.2. When l_t = 42mm, l_b = 33mm, and h = 7mm, the optimum 1.5:1 VSWR bandwidth of 16% can be achieved.

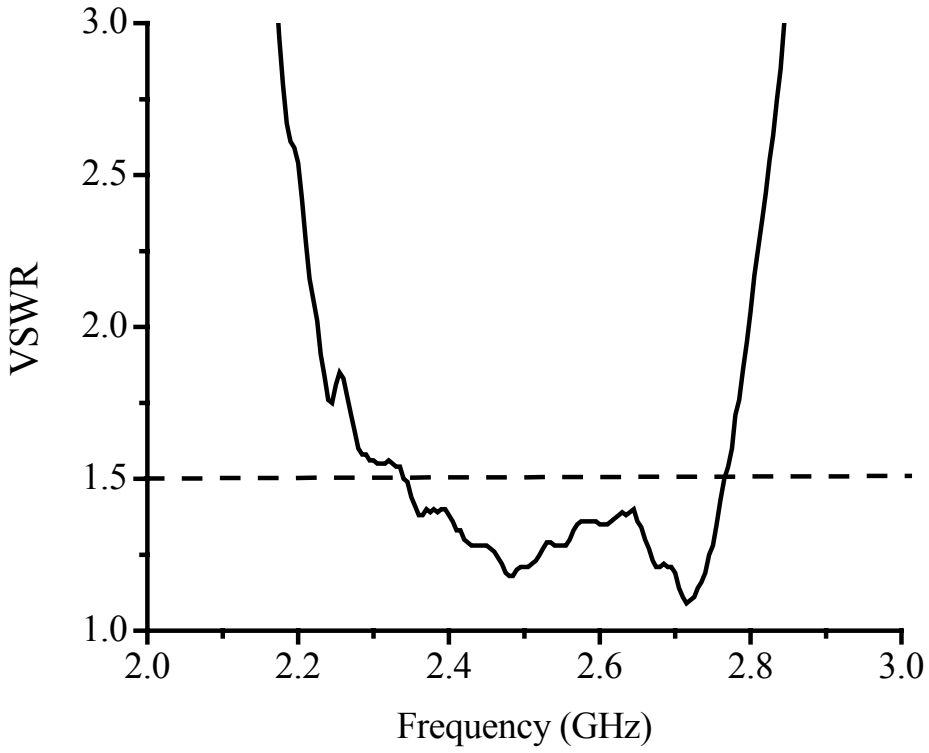

Fig. 2.5.2: Measured VSWR

Next, the radiation patterns were measured at 2.4GHz, 2.45GHz, and 2.5GHz in an anechoic chamber. The received power for the E_θ and E_ϕ components are plotted in Figs. 2.5.3 – 2.5.6 for the *x*-*z* and *y*-*z* planes.

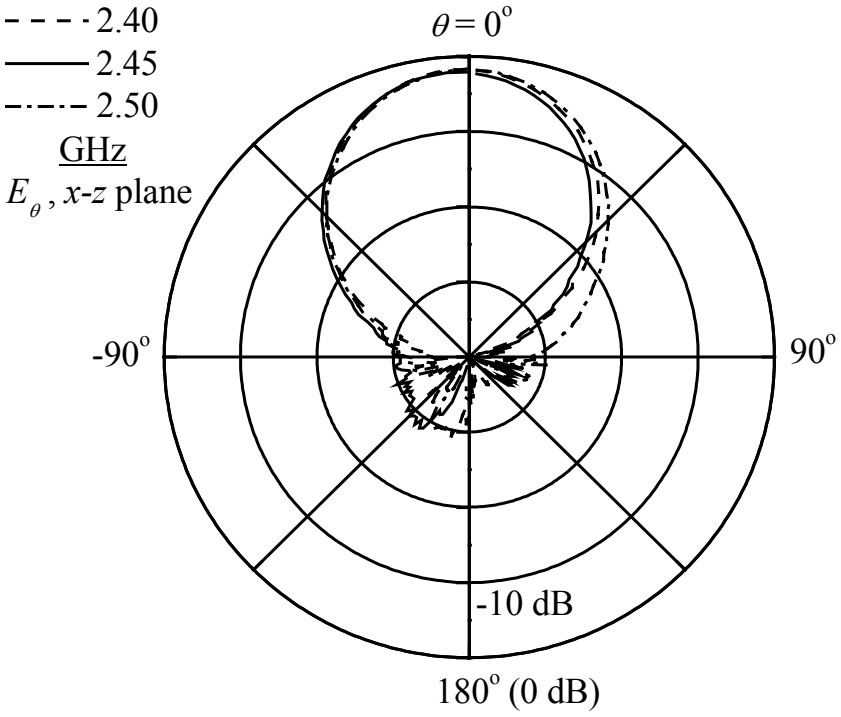

Fig. 2.5.3: Measured E_θ in the *x-z* plane

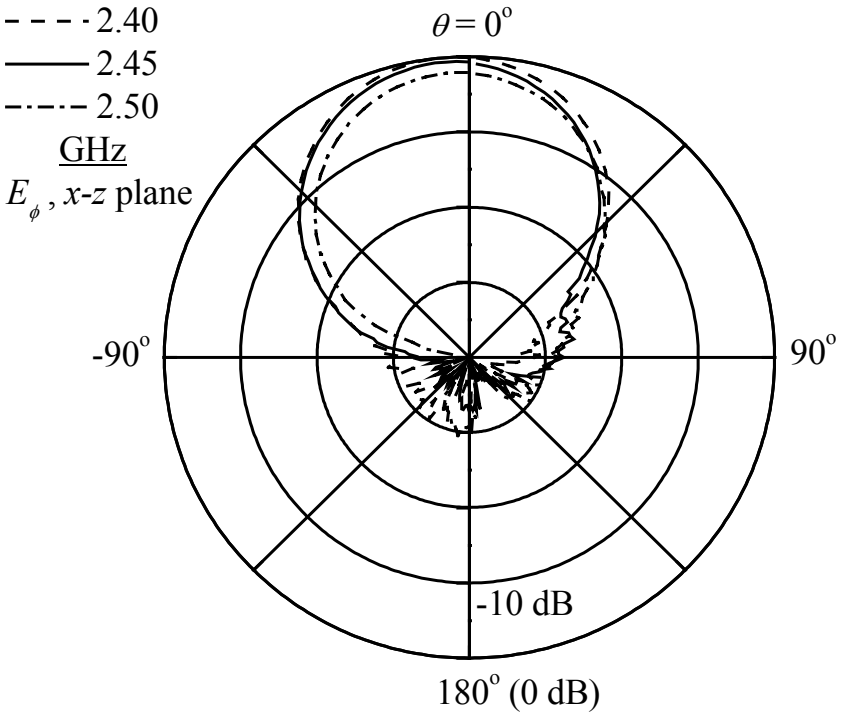

Fig. 2.5.4: Measured E_ϕ in the *x-z* plane

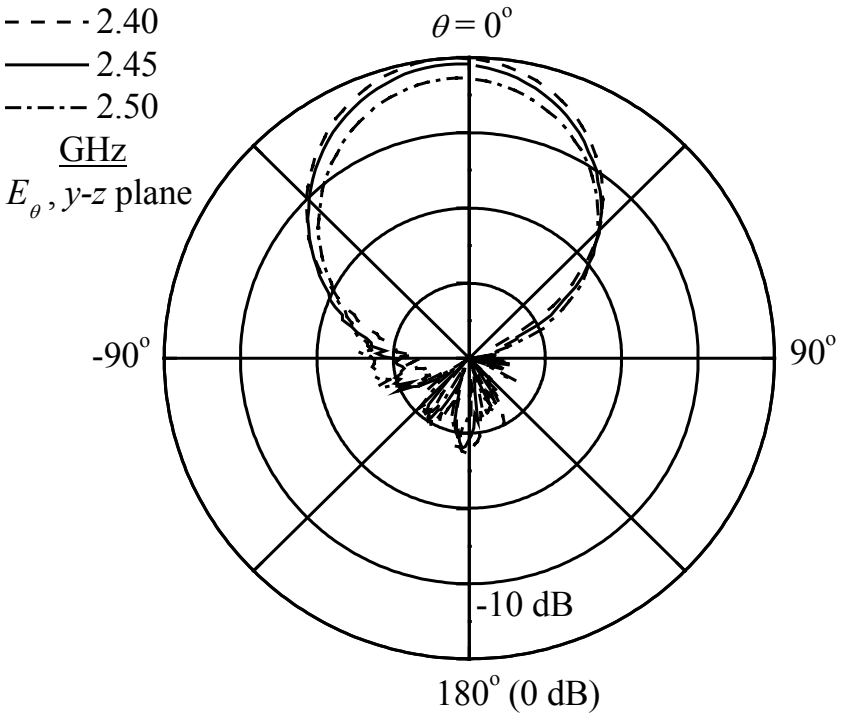

Fig. 2.5.5: Measured E_θ in the y-z plane

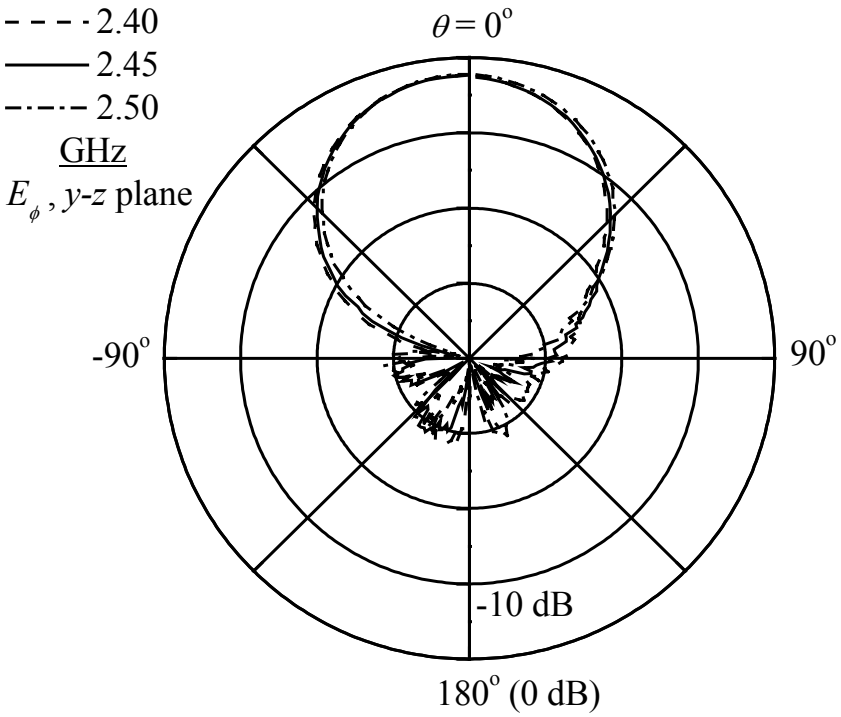

Fig. 2.5.6: Measured E_ϕ in the y-z plane

The patterns in each plane were normalized by the greatest E_θ or E_ϕ component for the three frequencies. The deviation of the E_θ and E_ϕ components with frequency is generally less than 2.2 dB in the *x-z* plane and 2.7dB in the *y-z* plane at the boresight. An antenna with ideal dual-linear polarization characteristics has equal E_θ and E_ϕ components across the impedance bandwidth. However, a difference of less than 6dB is usually required for satisfactory performance. From the figures, it can be observed that the difference between the E_θ and E_ϕ components at the boresight is less than 1.6dB and 2.2dB in the *x-z* and *y-z* planes, respectively.

The side-lobe levels are lower than –25dB in both the planes. In the *x-z* plane, the average HPBW is 48° and 46° in the *y-z* plane at 2.45GHz. The front-to-back ratios in both planes are generally greater than 25dB in both the planes. In addition, the measured average gains in both the planes are approximately 11dBi.

2.6 Stacked Offset Array

The 2 × 2 planar array has the drawback of a complicated feed network, which has to be carefully designed. Thus, a stacked offset array with a simple feed network is proposed. In the following sections, the design and analysis of the stacked offset array is presented. In Section 2.6.2, the array is simulated to investigate the effects of varying the size of the upper patches, the spacing between the two dielectric layers as well as the separation between the patches on the upper dielectric layer. The geometry as well as the measured impedance and radiation patterns of the array are also provided in Sections 2.6.1 and 2.6.3, respectively.

2.6.1 Geometry

The proposed geometry as shown in Fig. 2.6.1 consists of four radiating elements on the upper layer which are electromagnetically coupled to a driven patch (33mm × 33mm) etched on the bottom substrate layer. The feed point, diagonally fed by a microstrip line of 3.45mm width, is located at one of its corners on the bottom layer. The dielectric substrate (150mm × 150mm) used for both layers is Rogers 4003, with a relative permittivity of ε_r = 3.38, and a thickness of 60mil. The four patches each measuring 33mm × 33mm are separated at a same distance *d* in both *x* and *y* directions.

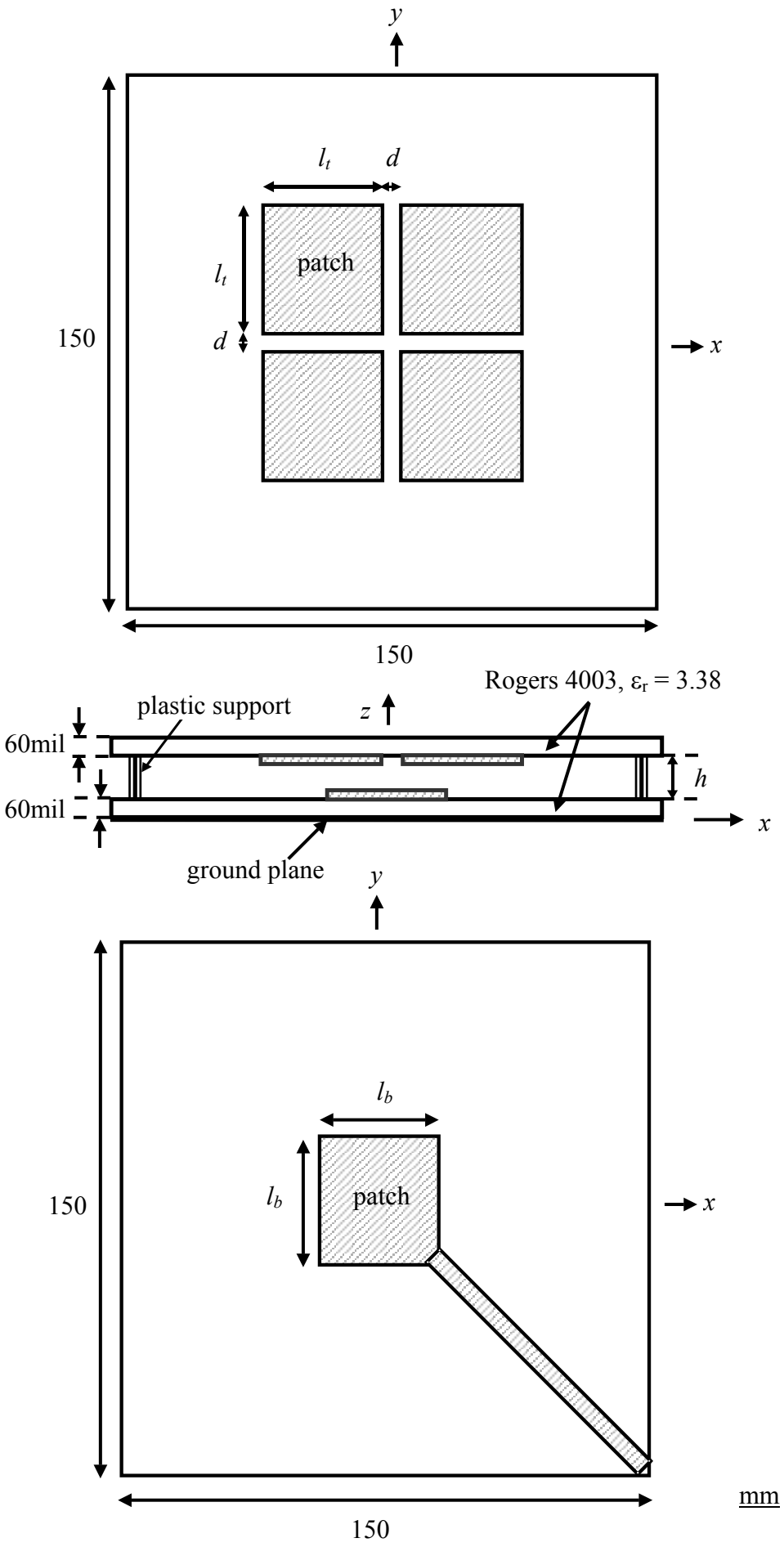

Fig. 2.6.1: Geometry of a stacked offset array

2.6.2 Parametric Study

In this section, the various physical parameters will be varied using the software Ansoft Ensemble v8.0 based on the Method of Moments (MoM) in order to study their effects on the impedance characteristics of the proposed array. The parameters of interests include the size as well as the separation between the patches on the superstrate layer and the spacing between the two dielectric layers.

(a) Effects of varying the size of upper patches

Firstly, the size of the upper patches l_t was varied from 32mm to 35mm with l_b = 33mm and h = 7mm. From Fig. 2.6.2, the size of the major loop is also observed to increase as l_t increases. According to Fig. 2.6.3, variations in l_t lead to the excitation of the upper resonance. Further increases in l_t will lead to the disappearance of the lower resonance. Two resonances at VSWR ≤ 1.5 can be observed clearly when l_t = 33mm. It can be seen that by adjusting the size of the upper patches, it is possible to achieve a broad bandwidth when both resonances are well matched. This can be seen from the minor loops appearing around the center of the Smith chart. Optimum matching can be obtained when l_t = 33mm and the impedance bandwidth obtained is 16%.

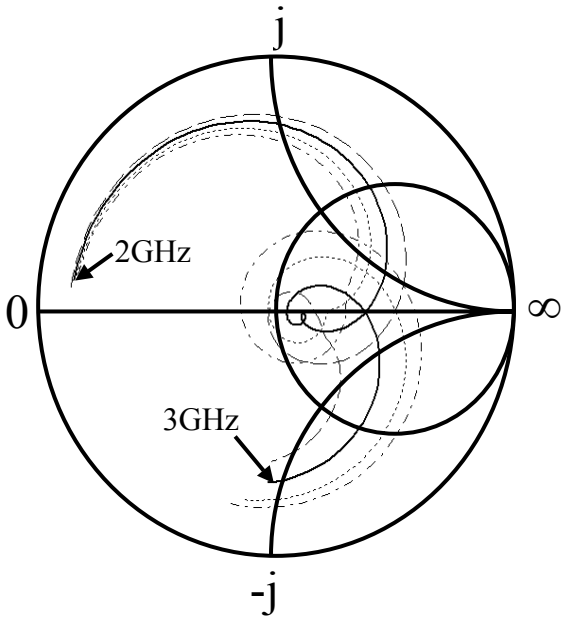

Fig. 2.6.2: Impedance loci for varying the size l_t of upper patches
(i) – – – 32mm (ii) ——— 33mm (iii) - - - - - 34mm (iv) — · — · 35mm

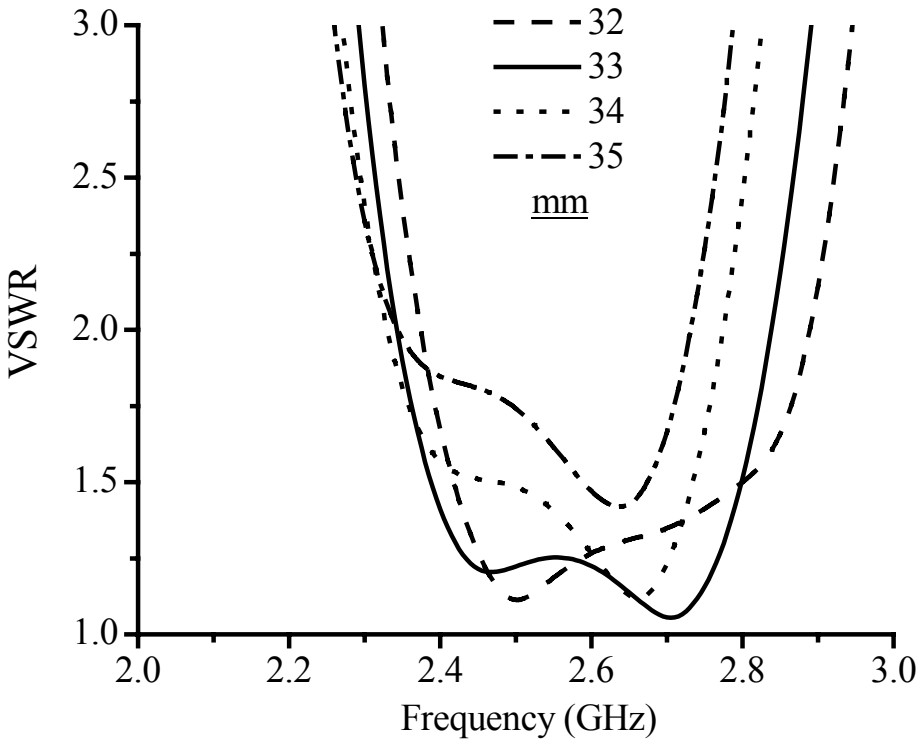

Fig. 2.6.3: Simulated VSWR for varying the size l_t of upper patches

(b) Effects of varying the spacing between dielectric substrates

Next, the spacing h between the upper and bottom patches was varied with $l_b = l_t =$ 33mm. As h increases from 6mm to 7.5mm, minor loops can be observed from the impedance loci which get smaller as the spacing h increases as shown in Fig. 2.6.4. When h is around 6mm to 7mm, both resonances are well matched as shown in Fig. 2.6.5. Good matching across a broader bandwidth can be achieved when the two resonances are brought closer together. Further increases in the spacing h will lead to a decline in bandwidth as the lower resonance disappears.

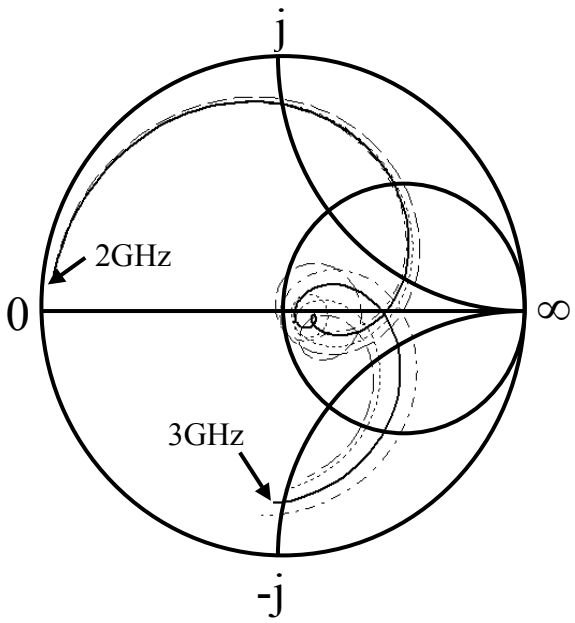

Fig. 2.6.4: Impedance loci for varying the spacing h between dielectric substrates
(i) — — — 6.0mm (ii) - - - - - 6.5mm (iii) ——— 7.0mm (iv) — · — · 7.5mm

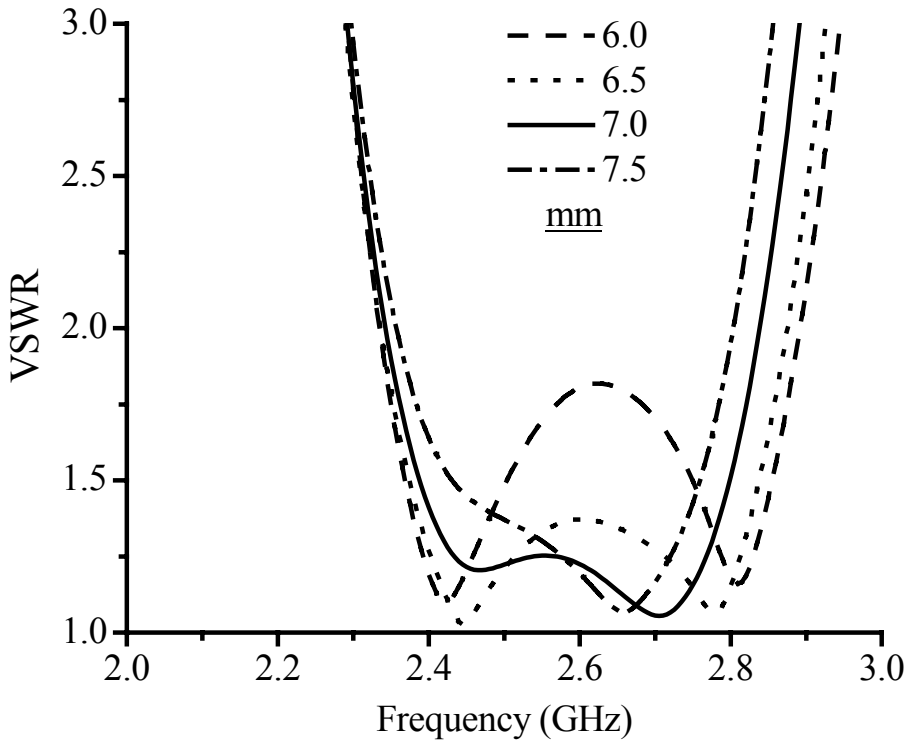

Fig. 2.6.5: Simulated VSWR for varying the spacing *h* between dielectric substrates

(c) Effects of varying the separation between elements

Lastly, the effects of varying the separation *d* between elements on the upper substrate layer are investigated. The separation *d* was varied from 2mm to 6mm with $l_t = l_b =$ 33mm, and h = 7mm. It can be seen from Fig. 2.6.6 that as *d* increases, the size of the major loop decreases and the minor loop gradually disappears. Optimum matching can be achieved when the patch elements are separated at around 3mm to 4mm apart. From Fig. 2.6.7, it can be seen that the frequency corresponding to the lower edge of the pass-band increases with *d*. Also, as *d* increases, the upper resonance disappears, leading to a considerable decline in the bandwidth.

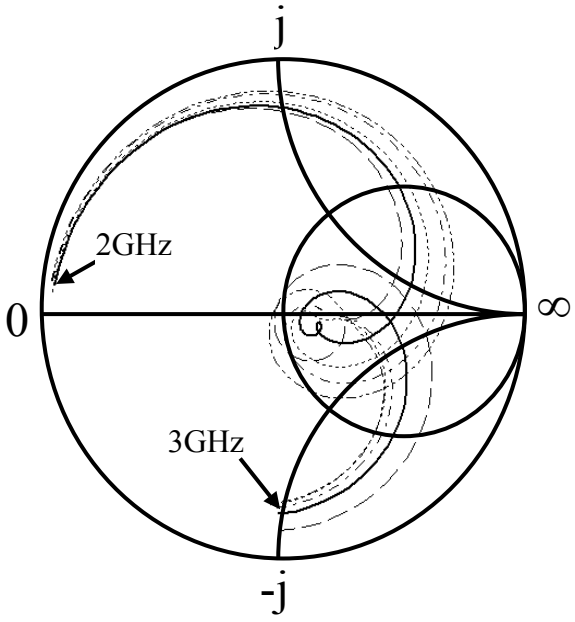

Fig. 2.6.6: Impedance loci for varying the separation *d* between patches
(i) — — — 2mm (ii) ——— 3mm (iii) - - - - - 4mm (iv) — · — · 5mm (v) — · · — 6mm

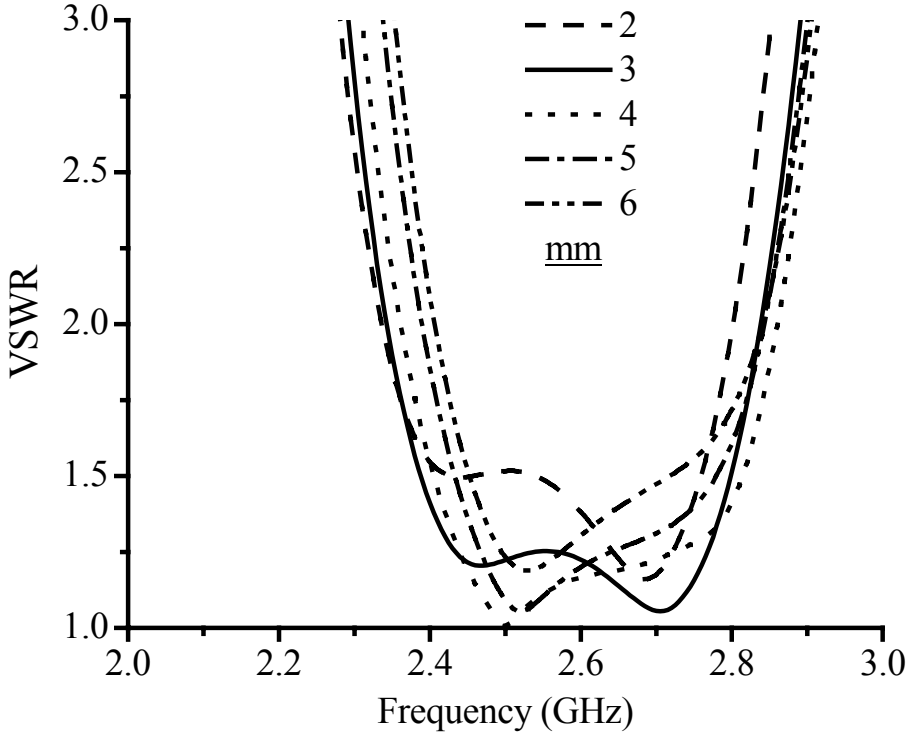

Fig. 2.6.7: Simulated VSWR for varying the separation *d* between patches

Therefore, it can be seen that the matching of the two resonances are determined collectively by the size of the upper patches, the spacing between the dielectric layers as well as the separation between the patches. The upper resonance is controlled predominantly by the size of the upper patches and the size of the lower patch primarily controls the lower resonance.

2.6.3 Measured Results

With the optimum parameters obtained from the parametric study, a prototype was fabricated and the impedance performance measured using an HP8510C Network Analyzer. Fig. 2.6.8 shows the measured VSWR for the array. The optimised array configuration occurs when $l_t = l_b = 33$mm, $d = 5$mm, and $h = 7$mm. The array is capable of achieving a 1.5:1 VSWR bandwidth of 16%.

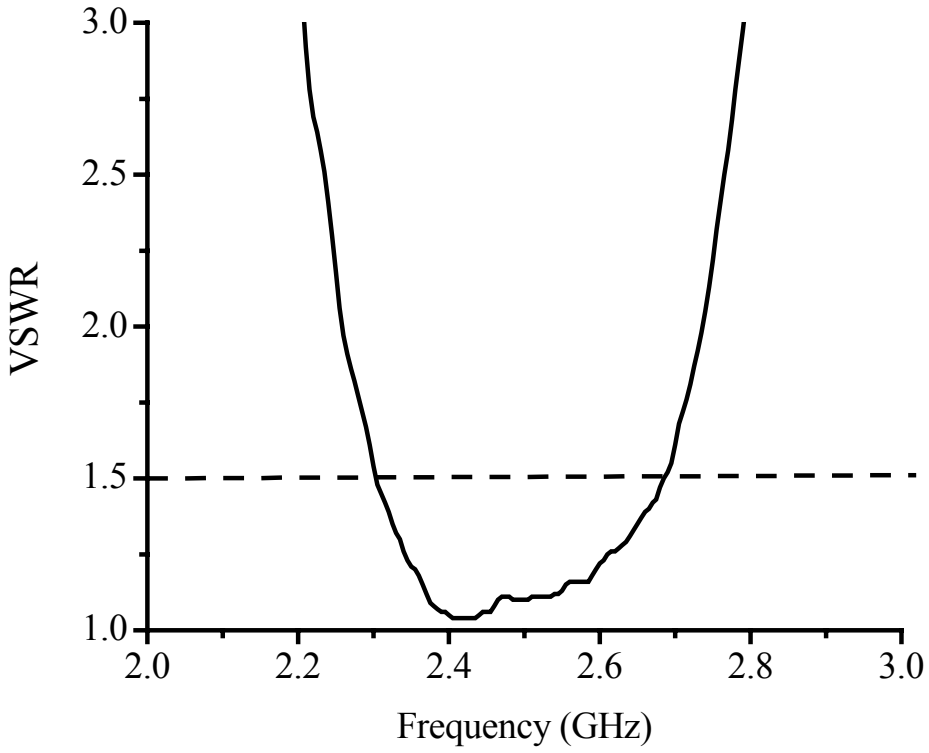

Fig. 2.6.8: Measured VSWR

The radiation patterns were then measured at three frequencies, namely, 2.4GHz, 2.45GHz and 2.50GHz. Figs. 2.6.9 – 2.6.12 display the received power in the *x-z* and *y-z* planes.

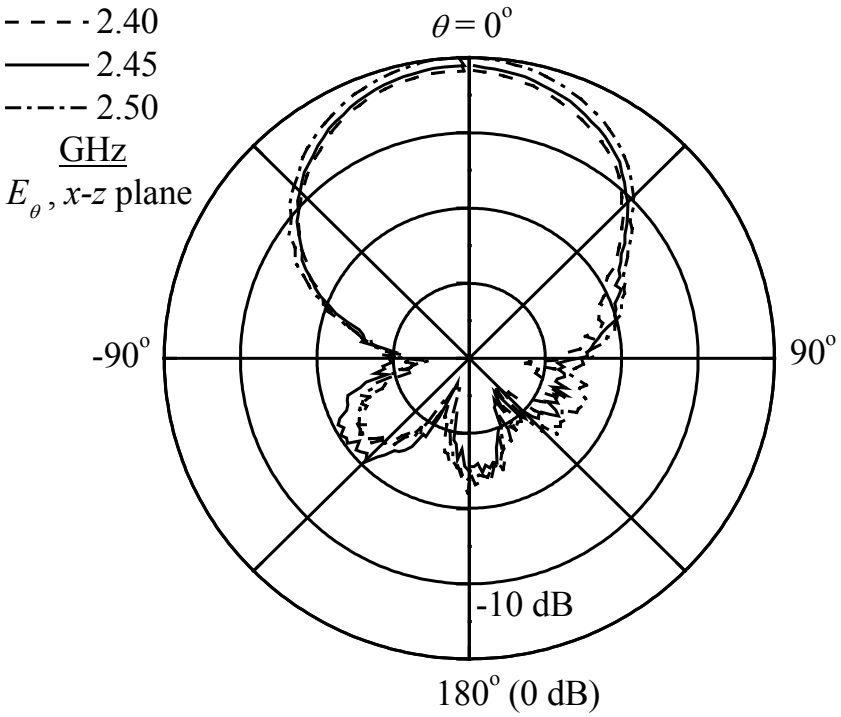

Fig. 2.6.9: Measured E_θ in the *x-z* plane

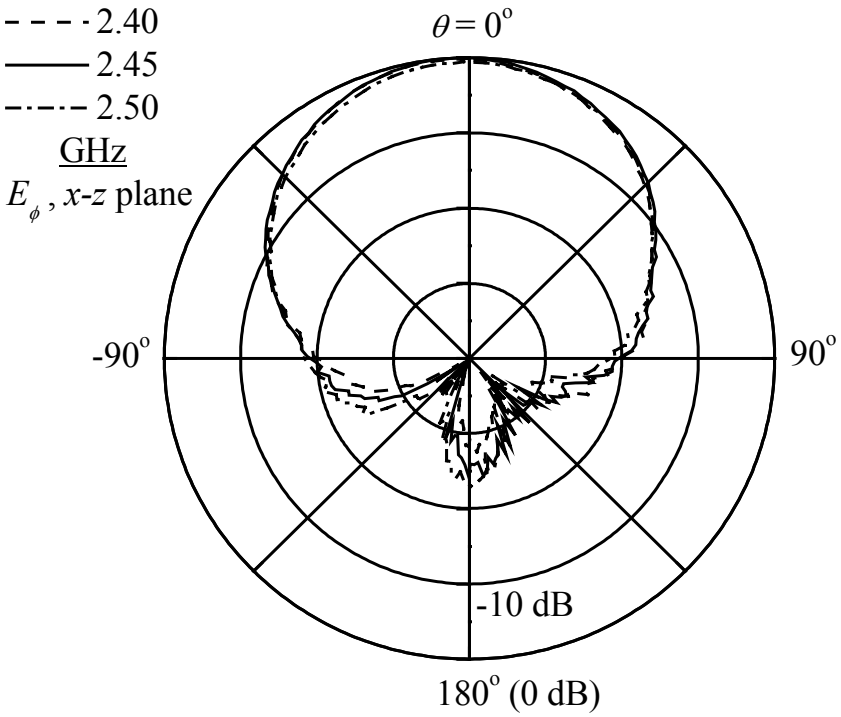

Fig. 2.6.10: Measured E_ϕ in the *x-z* plane

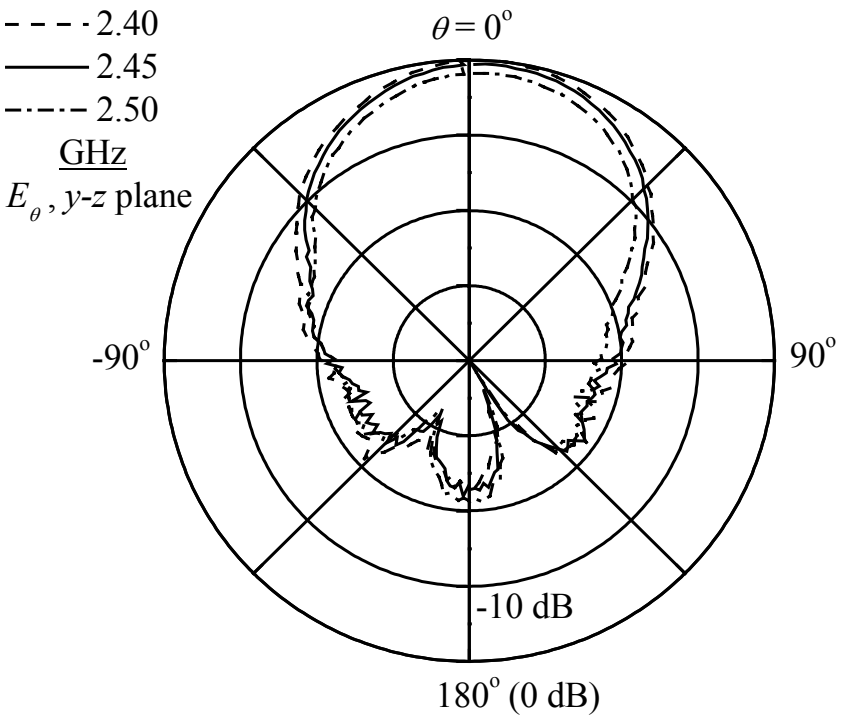

Fig. 2.6.11: Measured E_θ in the *y-z* plane

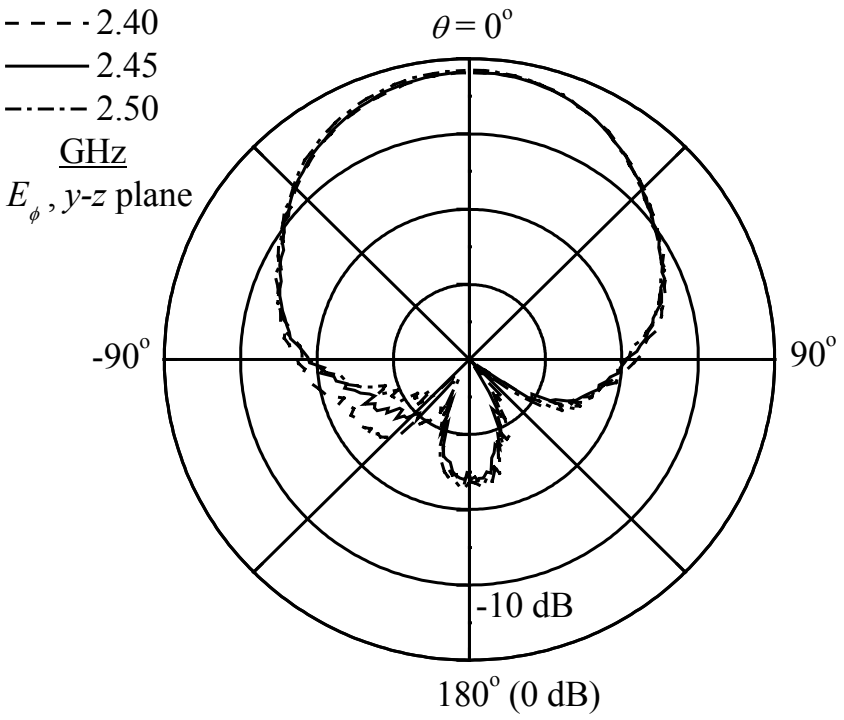

Fig. 2.6.12: Measured E_ϕ in the *y-z* plane

Having normalized the radiation levels by the maximum value at the three frequencies in each plane, it can be observed that the radiation patterns for the E_θ and E_ϕ components are found to be symmetrical with the absence of side-lobes in the upper-half space. The variation in each E_θ and E_ϕ component with frequency at the boresight is less than 1.7dB in both planes. As compared to the single element, two-element linear array and the 2 × 2 planar array, the radiation patterns for the stacked offset array change the least with frequency.

The maximum difference between the E_θ and E_ϕ components at the boresight in the *x-z* plane is 1.4dB and 1.8dB in the *y-z* plane. Compared to the 2 × 2 planar array, the stacked offset array offers the advantage of a lower difference in both the planes. This implies that across the 2.4GHz ISM band within the impedance bandwidth, good dual-linear polarization performance can be more easily achieved. In contrast with the two-element linear array and the single element, the difference in the *x-z* plane for the stacked offset array is much lower while the difference increases slightly in the *y-z* plane.

For the stacked offset array in the *x-z* plane, the average E_θ/ E_ϕ HPBW is 54°/61° and 62°/53° in the *y-z* plane. The front-to-back ratios are generally greater than 20dB in both the planes. In addition, the measured average gains in both the planes are approximately 9.5dBi.

2.7 Conclusions

In this Chapter, the designs of single feed dual-linear polarization antennas have been presented which include the single patch element, two-element linear array, 2 × 2 planar array as well as the stacked offset planar array.

The impedance performance of the antennas is evaluated in terms of the bandwidth for VSWR < 1.5. It can be seen that the antennas are able to achieve a broad impedance bandwidth of greater than 13%, which covers the 2.4GHz ISM band well. As for the radiation performance, it is evaluated in terms of the front-to-back ratio, gain, variation in the vertically and horizontal polarized components as well as the difference between them across the impedance bandwidth. From the measurement results, the 2 × 2 planar and stacked offset arrays are able to achieve front-to-back ratios greater than 20dB in both the *x*-*z* and *y*-*z* planes.

The stacked offset array, designed to reduce the complexity of the feed network, has a relatively stable radiation performance, as the vertical and horizontal patterns are less responsive to frequency as compared to the two-element linear array and 2 × 2 planar array. In addition, it has good dual-linear polarization characteristics, as the difference between the horizontal and vertical polarized components at the boresight is low across the impedance bandwidth. Also, the sidelobes for the offset array are well suppressed with an array gain of 9.5dBi.

Chapter 3

DIVERSITY FUNDAMENTALS

3.1 Introduction

In a flat fading channel, when all the arriving multipath components combine destructively at a receiving antenna, it will lead to a substantial decrease in signal-to-noise ratio (SNR). The receiver is said to enter into a deep fade or null. In order to decipher the desired signal reliably, an alternate signal path is required with a sufficiently large SNR. In other words, a secondary branch (or channel) is introduced to increase the probability that an adequate signal level can be received. Diversity is achieved by using the information on the different branches available to the receiver so as to increase the SNR at the decoding stage. This concept makes use of the fact that the uncorrelated or slightly correlated diversity branches have a low probability of simultaneously experiencing a deep fade. In order to increase the desired reliability, more than two branches might be required. By having additional branches, there is a higher probability that at least one branch, or the combined branch outputs, produces a sufficiently high SNR to allow reliable decoding of the message at the receiver.

3.2 Diversity Techniques

There are several methods to achieve independently fading signals. Depending on the propagation mechanism, these include space, polarization, angle, frequency, and time diversity.

In space diversity, the use of transmitting or receiving antennas separated in space is the most common diversity technique encountered. Two antennas that are physically spaced experience different propagation environments and the multipath components can sum destructively or constructively at each antenna. Often, the antennas are positioned far enough so that the branch signals have a higher probability of fading independently. In a macro-cellular environment where the scatterers are predominantly around the mobile terminals and the base stations are located on tall buildings or hilltops, the spacing between the antennas need to be large enough to achieve a low correlation as compared to a micro-cellular environment where the base station and the mobile are inside the clutter of buildings and other obstacles. This is because in a micro-cellular environment, the channel has a fast fading envelope that changes significantly with slight displacements of the antenna. In contrast, a macro-cellular environment is characterized by a slow fading envelope with respect to antenna displacement, thus the antennas need to be separated further apart (about 10λ to 20λ) to achieve independent fading of the branches [Tur95].

Polarization diversity implies that a single polarization at the transmitter can be depolarized in the propagation medium and the signal arrives at the terminal with a polarization that can differ greatly from the transmitted one. Also, due to the random movement of the transmitter or receiver, the polarization of the transmitted or received signal will not be fixed. Therefore, the antennas with orthogonal polarizations are used in polarization diversity systems such that at times, there will be a larger signal received on one polarization than on the other or at most, equal signals on both polarizations. Independent reception is possible with two orthogonal polarizations and the two resulting signals do not fade in a correlated manner. Polarization diversity has

the advantage over space diversity in that the antennas can be co-located and housed in a single unit smaller than that required for single polarization. In addition, the installation time is reduced and the structural design is lighter, thus leading to lower costs.

It has been reported that a slant ±45° configuration is slightly better (≈ 1dB) than the vertical/horizontal (V/H) configuration due to a lower difference in the mean signal powers between branches. It is also known that polarization diversity is more effective, especially when the orientation of the mobile antenna is inclined [Kar01][Lem98][Tur95][Wah97][Wei98].

Angle (or pattern) diversity uses antennas with different beam patterns on each branch. The multipath components are weighted differently at each channel, creating unalike interference patterns of the signal at each branch. Therefore, each channel receives the transmitted signal with different strengths depending on the branch pattern and the propagation characteristics at that moment in time. Similar to polarization diversity, angle diversity allows for the antennas to be co-located.

Frequency diversity can be implemented by transmitting information on more than one carrier frequency. The rationale behind this technique is that since frequencies separated by more than the coherence bandwidth of the channel are uncorrelated, and thus will not experience the same fading behaviour. However, the main disadvantage of using this diversity technique is that it requires valuable bandwidth that will reduce the communication capability. In addition, frequency diversity requires the same

number of receivers and channels. However, these can be justified for critical traffic conditions.

Time diversity transmits information repeatedly at time spacings that exceed the coherence time of the channel, so that the multiple repetitions of the signal received are essentially uncorrelated. However, time diversity requires information storage both at the transmitter and receiver which is much simpler for digital transmissions.

3.3 Factors Influencing Diversity Performance

The main factors affecting the diversity performance, regardless of the diversity technique used to improve signal reliability, are the relative power levels between branches and the envelope cross-correlation.

3.3.1 Difference in Mean Power Levels

For a two-branch diversity system, the average envelope power received in each branch (P_1 and P_2) can be written as follows [Jak74],

$$P_1 = E\left[e_1^{\,2}\right] = \int_0^\infty e_1^{\,2} f(e_1) de_1$$
$$P_2 = E\left[e_2^{\,2}\right] = \int_0^\infty e_2^{\,2} f(e_2) de_2 \qquad (3.1)$$

where $E[\bullet]$ is the expectation (mean) value operator, the subscripts 1 and 2 denote the channel number, and $f(e_n)$, n = 1, 2 is the distribution of the envelope for the branch.

Assuming equal noise power in each branch, the difference in power levels in a two-branch diversity system can be defined as,

$$P_{\text{diff}}\,(\text{dB}) = 10\log_{10}(\max[P_1\,,\,P_2]) - 10\log_{10}(\min[P_1\,,\,P_2]) \tag{3.2}$$

If one branch has a larger mean SNR than the other, its contribution to the final SNR will be more significant and hence the diversity gain of having a second branch will be reduced.

3.3.2 Cross-correlation

The cross-correlation, ρ, is a measure of the tendency of the signal in one branch to fade with the other. When $\rho = 1$, the two signals are said to be completely correlated, which means that they will fade, peak, increase, and decrease at the same time. On the other hand, when $\rho = 0$, the two signals are completely uncorrelated and the received signal envelope in one branch is independent of the other. Cross-correlation can be expressed mathematically as [Jak74],

$$\rho = \frac{E\left[\left(e_1 - \bar{e}_1\right)\left(e_2 - \bar{e}_2\right)\right]}{\sqrt{E\left[\left(e_1 - \bar{e}_1\right)^2\left(e_2 - \bar{e}_2\right)^2\right]}} \tag{3.3}$$

where

$$\bar{e}_{1,2} = E\left[e_{1,2}\right] = \int_0^\infty e_{1,2} f_{1,2}\left(e_{1,2}\right) de_{1,2} \tag{3.4}$$

Ideally, the received envelope in the branches should be independent of each other such that when one branch receives a signal that is very weak and indistinguishable

from noise, the system can still rely on the other to provide the receiver with a reliable link to the transmitted signals.

For successful diversity operation, a value of ρ = 0.7 or less is often used as a guideline [Lee72]. In spatial diversity systems, this can be achieved by spacing the antenna far enough while in polarization diversity antenna, it has been found that the cross-polar discrimination, which is found to be dependent on the propagation environment [Egg83][Koz84][Lem98][Lot96][Tur95][Vau90][Wah97] as well as the antenna design [See03], should be as close to unity (or 0dB) so as to achieve low correlation between the branches.

3.3.3 Diversity Gain

Diversity gain is used as a qualitative indication of diversity performance. It is a function of envelope correlation, number of branches, reliability or cumulative density function (CDF) percentage, and combining technique. Usually, the diversity gain is defined based on the significance of using diversity to reduce the fraction of time in which the signal drops below a certain specified level, or outage rate, usually specified with respect to the mean output noise level of the combiner. Alternatively, one may define the fraction of time that the signal level is exceeded, or reliability, which can be obtained from the CDF of the envelope. As an illustration, Fig. 3.3.1 [Die00] shows the CDF of the individual branches and that of the combined signal of the polarization diversity system using maximal ratio combining (MRC).

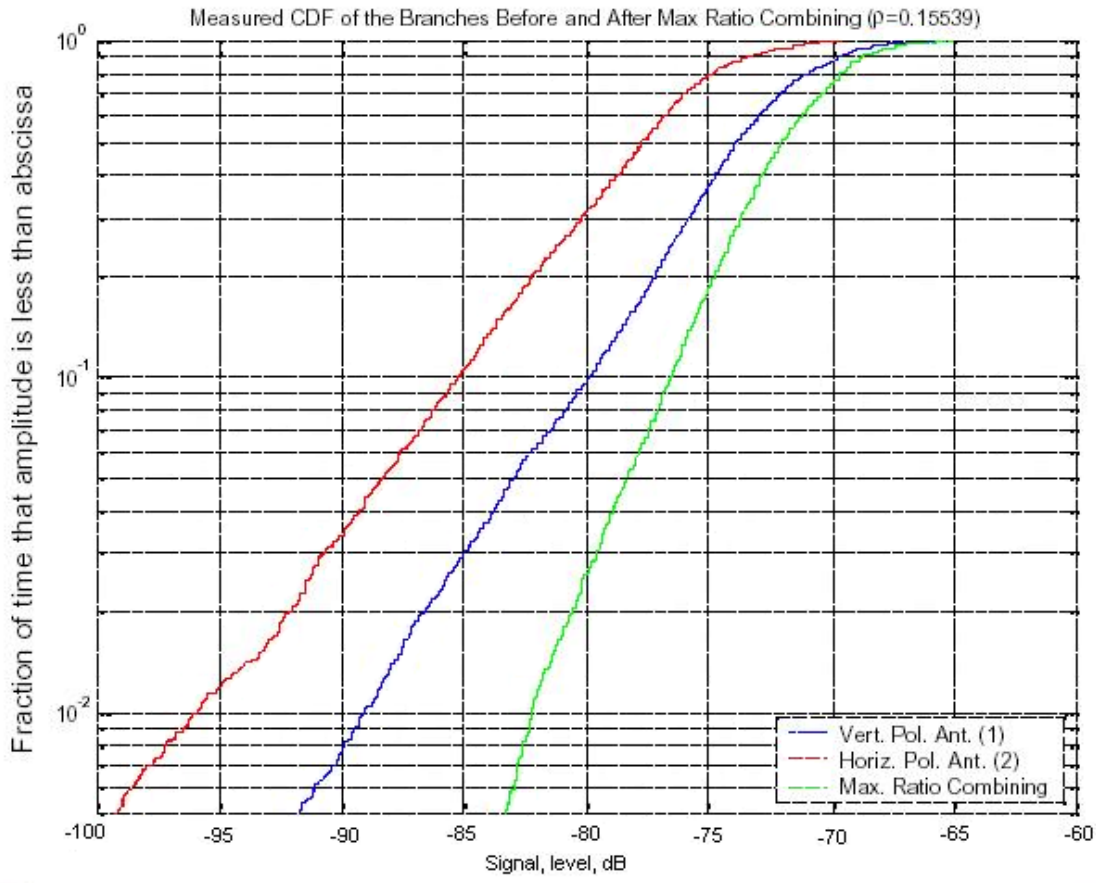

Fig. 3.3.1: Cumulative distribution function of a two-branch polarization diversity system

It can be seen that, at a 90% reliability level (10% outage rate), the signal levels on Antenna 1 and Antenna 2 are equal to or exceed –80dB and –85dB, respectively. The combined signal exceeds –76.5dB for 90% of the time. The diversity gain is then taken to be the improvement in signal levels over the strongest branch at a given reliability after combining. In this example, by measuring the horizontal distance between the combined signal and the branch with the larger signal power (Antenna 1) at a 10% CDF level, the diversity gain is 3.5dB. It can also be seen that at a 1% CDF level, the diversity gain increases to 7dB, which demonstrates that diversity gain is a function of the reliability level.

Besides reliability, correlation and the difference in signal levels between the two branches are also factors affecting the diversity gain as shown in Fig. 3.3.2. It can be observed that the largest diversity gain at 90% reliability is achieved when the mean levels of the signals from the two branches are equal and the correlation is low. There will be no appreciable diversity gain if the correlation is high and the difference in signal levels is large.

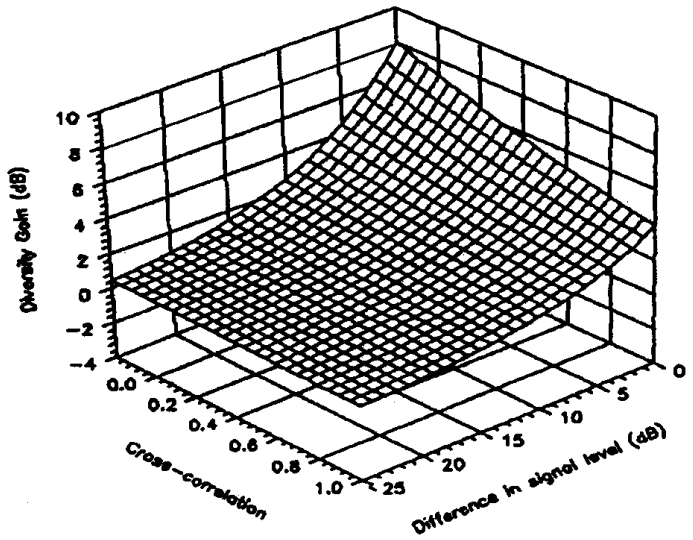

Fig. 3.3.2: Diversity gain at 90% signal reliability as a function of cross-correlation and mean branch signal level difference for two-branch diversity using MRC

3.4 Diversity Combining Techniques

Diversity branches can be established through space, angle, polarization, frequency, time, or any combination of these mechanisms. Regardless of the methods used to achieve diversity, the output from the branches can be processed using schemes such as selection, equal gain, or maximal ratio combining. Depending on the combining technique used, the diversity performance as well as the output SNR will be affected.

The following subsections will discuss and compare three common combining schemes (selection, maximal ratio, and equal gain) in terms of their diversity gain.

3.4.1 Selection Combining

Selection diversity chooses the receiver branch that has the largest instantaneous SNR to be connected to the demodulator as shown in Fig. 3.4.1. The greater the number the branches, the higher the probability of having a larger output SNR. In practice, the branch with the highest S+N/N is used since it is difficult to measure SNR alone.

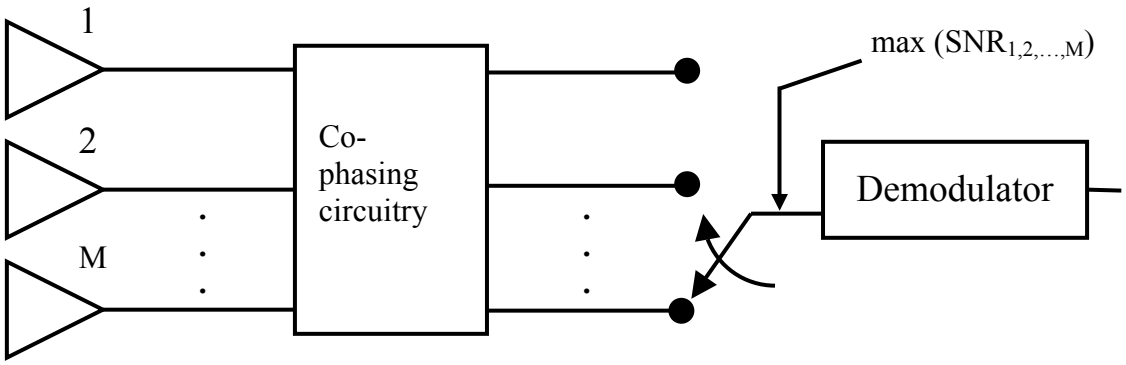

Fig. 3.4.1: Block diagram for selection diversity system

3.4.2 Maximal Ratio Combining

In this combining method first proposed by Kahn [Kah54], the signals from all the M branches are weighted according to their individual instantaneous SNRs. In order to ensure that all the branches are added in phase for maximum diversity gain, the branches are co-phased prior to summing as shown in Fig. 3.4.2. Unlike selection diversity which selects the branch with the greatest SNR, this technique takes advantage of all the channels in order to get a more reliable received signal. A distinct

advantage of using this combining technique is the capability of producing an output with acceptable SNR even when none of the SNRs from the individual branches are acceptable. However, a drawback of using maximal ratio combining is that it is more complicated and requires accurate estimates of the instantaneous signal level and average noise power in order to achieve optimum diversity performance. As this method will perform better than the selection or equal gain combining since it is an optimum combiner [Pro95], it will be used in the analysis of the various polarization diversity antennas in Chapters 4 and 5.

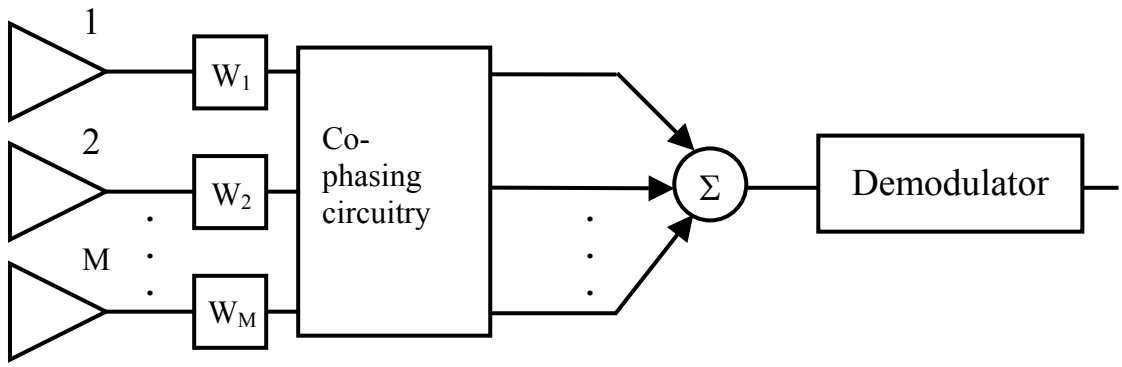

Fig. 3.4.2: Block diagram for maximal ratio diversity system

3.4.3 Equal Gain Combining

This technique is similar to maximal ratio combining except that the weights in each branch are the same ($W_1 = W_2 = \ldots = W_M$). In this technique, a phase lock summing circuit is used. The branch signals are coherently combined but the noise components are incoherently combined. The advantage of producing an acceptable output from a number of unacceptable inputs is still retained. Its performance is marginally inferior to maximal ratio combining but superior to selection combining as shown in Fig. 3.4.3 for the case of $M = 2$.

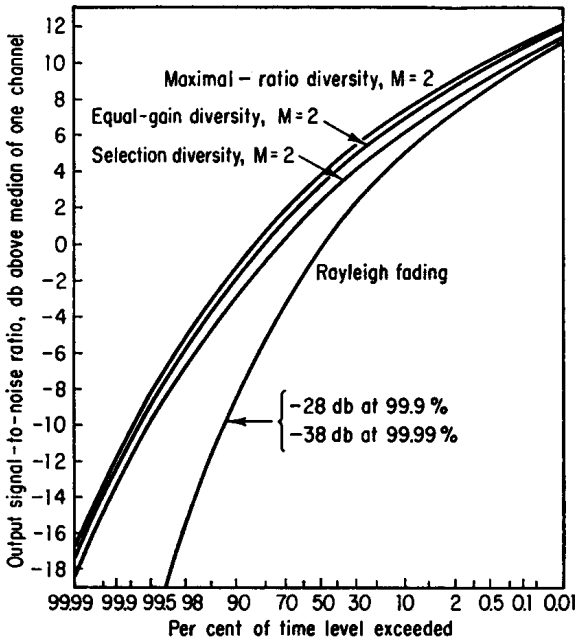

Fig. 3.4.3: Combiner probability distributions for M = 2 [Sch65]

It can be observed that at 90% reliability, the maximal ratio diversity has a gain of 7dB as compared to 6.5dB and 5.5dB for equal gain and selection diversity, respectively. This difference in diversity gain will become more significant as the number of channels increases as shown by the bottom two curves of Fig. 3.4.4. Although selection diversity is inferior as compared to maximal ratio and equal gain diversity, the upper three curves demonstrate that it is still able to provide a significant improvement in diversity gain and that the rate of further gain diminishes with increasing order of diversity.

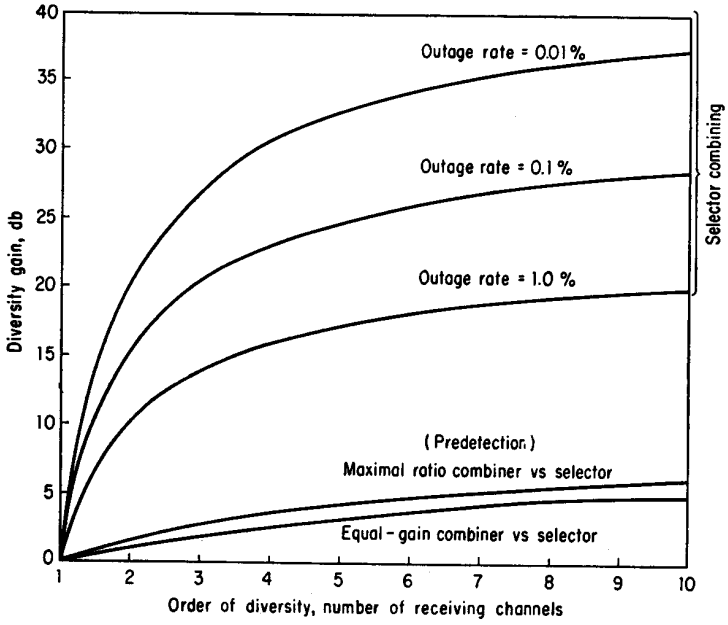

Fig. 3.4.4: Diversity gain as a function of order of diversity [Sch65]

After combining, the average SNR is given as [Jak74],

$$\langle\gamma\rangle = \Gamma\sum_{m=1}^{M}\frac{1}{m} \qquad \text{for selection combining} \qquad (3.5)$$

$$\langle\gamma\rangle = \Gamma\left(1+(M-1)\frac{\pi}{4}\right) \qquad \text{for equal gain combining} \qquad (3.6)$$

$$\langle\gamma\rangle = \Gamma M \qquad \text{for maximal ratio combining} \qquad (3.7)$$

where Γ is the mean SNR per branch, and M is the number of branches.

From the above equations, it can be seen that for maximal ratio combining, the improvement in average SNR increases proportionately with the number of branches. The improvement in average SNR for selection combining increases slowly with the number of branches. As shown in Fig. 3.4.4, the improvement in average SNR for equal gain combining is only 1.05dB poorer than maximal ratio combining, in the limit of an infinite number of branches.

Chapter 4

DIVERSITY PERFORMANCE OF STACKED PATCH ANTENNAS

4.1 Introduction

An electromagnetic wave can be elliptically, circularly or linearly polarized. If the state of polarization does not change with time, it is said to be completely polarized. The polarization of a randomly polarized wave varies continuously in a time varying manner with a zero time average value of polarization at any one state. A partially polarized radiation consists of a randomly polarized component and a completely polarized component. The characteristics of a completely polarized wave emanating from a point source will be examined in detail in the following section. The reception of radiation from distributed sources, which is more general, will be discussed subsequently.

The performance of a dual-linear polarized antenna can be characterized in terms of its return loss at both ports as well as port-to-port isolation, co-polar, and cross-polar radiation patterns. However, in order for the antenna to be suitable for base station applications, the far-field coupling and diversity gain must also be considered.

In this Chapter, the design and performances of a stacked dual-linear patch element and array designed for 3G applications will be evaluated according to the parameters stated above.

4.2 Theoretical Analysis

The power received by an antenna can be shown to be dependent on its polarization properties as well as the polarization of incident radiation. From Fig. 4.2.1, Antenna *a* is fed from a shielded source and Antenna *b* is a short linear current element [Col69].

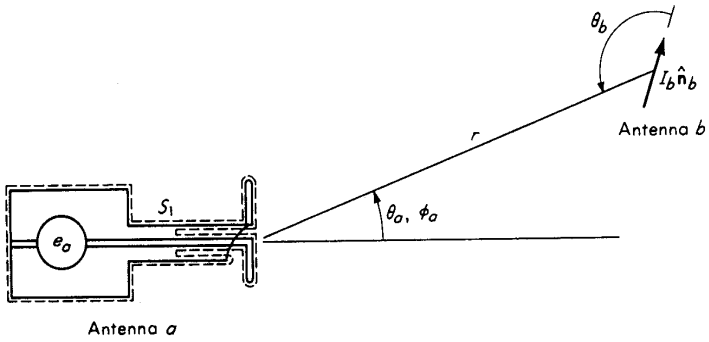

Fig. 4.2.1: Antenna excited by a current element

By Reciprocity Theorem, we have,

$$V_{1a}I_{1b} + V_{1b}I_{1a} = -\boldsymbol{E}_a.\hat{n}_b\, I_b\Delta l$$

Suppose Antenna *b* is not terminated by a load, i.e., is open circuited at the terminals, then $I_{1b} = 0$ and the open circuit voltage can be expressed as,

$$V_{1b} = V_{oc} = -\frac{\boldsymbol{E}_a.\hat{n}_b}{I_{1a}} I_b\Delta l \qquad (4.2)$$

When the antenna is transmitting, the elliptical polarized wave which is radiated can be written as,

$$\boldsymbol{E}_a = E_\theta\,\hat{\theta} + E_\phi\,\hat{\phi} = r_\theta(t)e^{-j\psi_\theta(t)}\,\hat{\theta} + r_\phi(t)e^{-j\psi_\phi(t)}\,\hat{\phi} \qquad (4.3)$$

where θ and ϕ denote the vertical and horizontal polarizations. The phase of the signals ψ_θ and ψ_ϕ are uncorrelated and uniformly distributed over $[0,2\pi]$. The $r_\theta(t)$ and $r_\phi(t)$ are

real-valued functions which represent the envelope of the signal. It is assumed that $r_\theta(t)$ and $r_\phi(t)$ are Rayleigh distributed [Egg98][Vau90] and uncorrelated [Egg98][Koz84][Lem98][Tur95][Vau90] for a typical mobile communication system.

To characterize the receiving antenna, a complex effective vector length $\boldsymbol{h}$ has been introduced by Sinclair [Sin50]. Under transmitting conditions, the radiated field can be expressed as,

$$\boldsymbol{E}_a = \frac{j\zeta_0 I_{1a}\boldsymbol{h}}{2\lambda_0 r} e^{-jk_0 r} \tag{4.4}$$

If we compare Eq. (4.4) to that of the radiation field by a unit electric current source, it can be seen that $\boldsymbol{h}$ gives the radiated field relative to that from a current element of unit length.

The incident field $\boldsymbol{E}_0$ can be taken as originating from two electric current elements perpendicular to each other. These current elements will produce an incident field given by,

$$\boldsymbol{E}_0 = -\frac{j\zeta_0 \Delta l}{2\lambda_0 r} e^{-jk_0 r}\left(I_\theta \hat{\theta} + I_\phi \hat{\phi}\right) \tag{4.5}$$

Rewriting I_θ and I_ϕ in terms of $E_{0\theta}$ and $E_{0\phi}$

$$\begin{aligned} I_\theta &= -\frac{2\lambda_0 r e^{+jk_0 r}}{j\zeta_0 \Delta l} E_{0\theta} \\ I_\phi &= -\frac{2\lambda_0 r e^{+jk_0 r}}{j\zeta_0 \Delta l} E_{0\phi} \end{aligned} \tag{4.6}$$

Substituting Eqs. (4.4) and (4.6) into Eq. (4.2), the open circuit received voltage can be simplified to give,

$$V_{oc} = h_\theta E_{0\theta} + h_\phi E_{0\phi} = \boldsymbol{h}.\boldsymbol{E}_0 \tag{4.7}$$

The total received open circuit voltage will be the sum of the contributions from all directions seen by the receiving antenna,

$$V_{oc} = \int \boldsymbol{h}(\Omega) \bullet \boldsymbol{E}(\Omega, t) d\Omega \tag{4.8}$$

where the direction given by θ and ϕ is given by the solid angle Ω.

The far-field coupling can be derived from the complex antenna channel vectors. If we define the polarization matrix for the incident field as,

$$\boldsymbol{J}'(\theta_1, \phi_1; \theta_2, \phi_2) = \begin{bmatrix} J'_{\theta\theta} & J'_{\theta\phi} \\ J'_{\phi\theta} & J'_{\phi\phi} \end{bmatrix} \tag{4.9}$$

where the elements in the matrix are of the form,

$$J'_{\theta\phi}(\theta_1, \phi_1; \theta_2, \phi_2) = \left\langle E_\theta(\theta_1, \phi_1, t) E_\phi^*(\theta_2, \phi_2, t) \right\rangle \tag{4.10}$$

The polarization matrix for the antenna can also be defined as,

$$\boldsymbol{J}(\theta_1, \phi_1; \theta_2, \phi_2) = \begin{bmatrix} J_{\theta\theta} & J_{\theta\phi} \\ J_{\phi\theta} & J_{\phi\phi} \end{bmatrix} \tag{4.11}$$

where the elements in the matrix are of the form,

$$J_{\theta\phi}(\theta_1, \phi_1; \theta_2, \phi_2) = \left\langle h_\theta(\theta_1, \phi_1, t) h_\phi^*(\theta_2, \phi_2, t) \right\rangle \tag{4.12}$$

If the polarizations are considered uncorrelated and each polarization considered spatially uncorrelated, then,

$$J'(\theta_1, \phi_1; \theta_2, \phi_2) = P(\theta, \phi) \delta(\theta_1 - \theta_2) \delta(\phi_1 - \phi_2) \begin{bmatrix} \chi & 0 \\ 0 & 1 \end{bmatrix} \tag{4.13}$$

where χ refers to the cross-polar discrimination and,

$$P(\theta, \phi) = P \qquad \theta_L \le \theta \le \theta_u, \phi_L \le \phi \le \phi_u \tag{4.14}$$

$$= 0, \qquad \text{elsewhere}$$

The correlation coefficient for the open circuit signals are expressed as,

$$\rho_{12} = E\left\{V_{oc(1)} V_{oc(2)}{}^{*}\right\} \tag{4.15}$$

where $E\{\bullet\}$ refers to the expectation operator.

Substituting Eqs. (4.8), (4.10), and (4.12) into Eq. (4.15),

$$\rho_{12} = \iint \left(J_{\theta\theta} J'_{\theta\theta} + J_{\phi\phi} J'_{\phi\phi} + J_{\theta\phi} J'_{\theta\phi} + J_{\phi\theta} J'_{\phi\theta}\right) d\Omega_1 d\Omega_2 \tag{4.16}$$

Assuming that orthogonal polarizations are uncorrelated, using Eq. (4.13) and substituting into Eq. (4.16),

$$\rho_{12} = \int_{\Omega_l}^{\Omega_u} \chi\left(h_{\theta 1}(\Omega) h_{\theta 2}{}^{*}(\Omega)\right) + h_{\phi 1}(\Omega) h_{\phi 2}{}^{*}(\Omega) d\Omega \tag{4.17}$$

The various constants drop out under normalization. It should be noted that for the unpolarized case where $\chi = 1$ (0dB), the correlation coefficient corresponds to the far-field coupling of the antenna.

The signals in the respective diversity branches can be given by Eq. (4.18), where $u(t)$ is the complex valued low pass signal common to all the branches, f_0 is the carrier frequency and $g_k(t)$ is the equivalent low-pass transfer function, assuming non-selective fading on each diversity branch.

$$v_k(t) = \mathrm{Re}\left[g_k(t) u(t) \exp\left(j 2\pi f_0 t\right)\right] \tag{4.18}$$

$u(t)$ can be normalized to unit mean square envelope with period $2T$ given by,

$$\frac{1}{2T} \int_{-T}^{T} \left|u(t)\right|^2 dt = 1 \tag{4.19}$$

Using Eq. (4.19), the instantaneous signal-to-noise ratio in the k^{th} receiver can be written as the ratio of the instantaneous complex signal to noise envelopes,

$$\gamma_k = \frac{\frac{1}{2}|v_k(t)|^2}{\frac{1}{2}|n_k(t)|^2} = \frac{1}{2}\frac{|g_k|^2}{N_k} \tag{4.20}$$

From Eqs. (4.18) and (4.19), the complex envelopes in the diversity branches are of the form,

$$v_k(t) = g_k(t)u(t) + n_k(t) \tag{4.21}$$

The output complex envelope from general linear combining can be expressed as,

$$v(t) = \sum_{k=1}^{M} \alpha_k v_k(t) \tag{4.22}$$

where α_k are the complex weights which are changed from time to time as the branch signals vary over short-term fading in maximal ratio combining. In the case of selection combining, all the α_k are zero except for the branch with the largest SNR. For equal gain combining, the α_k have phase opposite to the signals in the respective branches but equal in magnitude. In the subsequent analysis, the maximal ratio combiner will be used so as to achieve the maximum output SNR at any instant.

With Eqs. (4.21) and (4.22), the signal and noise complex envelopes at the output of the combiner are,

$$s(t) = u(t)\sum_{k=1}^{M} \alpha_k g_k(t) \tag{4.23a}$$

$$n(t) = \sum_{k=1}^{M} \alpha_k n_k(t) \tag{4.23b}$$

The instantaneous output SNR is shown in Eq. (4.24), using the normalization in (4.19) and assuming that the $n_k(t)$ are mutually independent.

$$\gamma = \frac{1}{2}\frac{\left|\sum_{k=1}^{M}\alpha_k g_k\right|^2}{\sum_{k=1}^{M}|\alpha_k|^2 N_k} = \frac{1}{2}\frac{|g_k|^2}{N_k} \tag{4.24}$$

The output SNR given in Eq. (4.24) can be maximized by applying the Schwarz Inequality for complex-valued numbers, i.e.,

$$\left|\sum_{k=1}^{M} p_k^{*} q_k\right|^2 \le \left(\sum_{k=1}^{M}|p_k|^2\right)\left(\sum_{k=1}^{M}|q_k|^2\right) \tag{4.25}$$

where $q_k = Cp_k$ for all k

is a necessary condition for the equality to hold which means that both the vectors must be parallel and in phase, and C is an arbitrary complex constant.

Applying Eq. (4.25) into Eq. (4.24), by setting $p_k = \frac{g_k^{*}}{\sqrt{N_k}}$ and $q_k = \alpha_k\sqrt{N_k}$,

$$\left|\sum_{k=1}^{M}\alpha_k g_k\right|^2 \le \left(\sum_{k=1}^{M}\frac{|g_k|^2}{N_k}\right)\left(\sum_{k=1}^{M}|\alpha_k|^2 N_k\right) \tag{4.26}$$

Re-writing using Eq. (4.24),

$$\gamma \le \frac{1}{2}\sum_{k=1}^{M}\frac{|g_k|^2}{N_k} \tag{4.27}$$

where $\alpha_k = C\frac{g_k^{*}}{N_k}$ for all k

The terms on the right of Eq. (4.27) correspond to the individual instantaneous SNR on each branch defined in Eq. (4.20). Thus, this combiner results in an instantaneous output SNR which is the sum of the instantaneous SNR on the individual branches,

$$\gamma = \sum_{k=1}^{M}\gamma_k \tag{4.28}$$

With the instantaneous SNR defined in Eq. (4.28), the probability distribution function (p.d.f.), $p(\gamma)$, can be determined by first considering the Laplace transformation,

$$F(s)=\int_0^{\infty}\exp(-s\gamma)p(\gamma)d\gamma=\langle\exp(-s\gamma)\rangle=\prod_{k=1}^{M}\langle\exp(-s\gamma_k)\rangle \tag{4.29}$$

The γ_k are independently exponentially distributed, and the p.d.f. is given as,

$$p(\gamma_k)=\frac{1}{\Gamma_k}\exp\left(-\frac{\gamma_k}{\Gamma_k}\right) \tag{4.30}$$

where Γ_k is the average of γ_k over the short-term fading.

Thus,

$$\langle\exp(-s\gamma_k)\rangle=\int_0^{\infty}\exp(-s\gamma_k)\frac{1}{\Gamma_k}\exp\left(-\frac{\gamma_k}{\Gamma_k}\right)d\gamma_k=\frac{1}{1+s\Gamma_k} \tag{4.31}$$

where Re $s \geq 0$

Therefore,

$$F(s)=\prod_{k=1}^{M}\frac{1}{1+s\Gamma_k} \tag{4.32}$$

By performing the inversion of Eq. (4.29), for M-branch maximal ratio combining, the p.d.f. can be written as [Sch65],

$$p(\gamma)=\frac{1}{2\pi j}\int_{c-j\infty}^{c+j\infty}\frac{\exp(s\gamma)}{\prod_{k=1}^{M}(1+s\Gamma_k)}ds \qquad \text{where } c\geq 0 \tag{4.33}$$

The contour of integration can be closed at ∞ in the left-half plane with only poles enclosed. Hence, the integral can be evaluated by routine residual calculations. Two cases are considered. One is when all the Γ_k are equal. Considering two-branch maximal ratio combining, Eq. (4.33) becomes,

$$p(\gamma)=\frac{\gamma}{\Gamma^2}e^{-\frac{\gamma}{\Gamma}} \tag{4.34}$$

The cumulative distribution function is obtained by integrating Eq. (4.34), giving,

$$p(\gamma < \varphi) = 1 - e^{-\frac{\varphi}{\Gamma}}\left(\frac{\varphi}{\Gamma} + 1\right) \tag{4.35}$$

Another case is when $\Gamma_1 \neq \Gamma_2$, which gives,

$$p(\gamma) = e^{\frac{-\gamma}{\Gamma_1}}\left(\frac{1}{\Gamma_1 - \Gamma_2}\right) + e^{\frac{-\gamma}{\Gamma_2}}\left(\frac{1}{\Gamma_1 - \Gamma_2}\right) \tag{4.36}$$

By integrating Eq. (4.36), the cumulative distribution function is,

$$p(\gamma < \varphi) = 1 - \frac{\Gamma_1 e^{-\frac{\varphi}{\Gamma_1}} - \Gamma_2 e^{-\frac{\varphi}{\Gamma_2}}}{\Gamma_1 - \Gamma_2} \tag{4.37}$$

The covariance matrix can be defined as,

$$C = \begin{pmatrix} \frac{\chi}{\chi+1} & \rho\sqrt{\frac{\chi}{(\chi+1)^2}} \\ \rho^*\sqrt{\frac{\chi}{(\chi+1)^2}} & \frac{1}{\chi+1} \end{pmatrix} \tag{4.38}$$

where ρ in Eq. (4.38) represents the complex cross-covariance which can be taken as the far-field coupling of the two channels and its eigenvalues are the solutions to,

$$\begin{vmatrix} \frac{\chi}{\chi+1} - \lambda & \rho\sqrt{\frac{\chi}{(\chi+1)^2}} \\ \rho^*\sqrt{\frac{\chi}{(\chi+1)^2}} & \frac{1}{\chi+1} - \lambda \end{vmatrix} = 0 \tag{4.39}$$

The eigenvalues are,

$$\lambda_1 = \frac{1}{2}\left[1 - \sqrt{1 - 4\left(\frac{\chi}{(\chi+1)^2}\right)\left(1 - |\rho|\right)^2}\right] \qquad \lambda_2 = \frac{1}{2}\left[1 + \sqrt{1 - 4\left(\frac{\chi}{(\chi+1)^2}\right)\left(1 - |\rho|\right)^2}\right] \tag{4.40}$$

From Appendix B of [Sch65], it can be shown that,

$$p(\gamma) = \frac{1}{2\pi j}\int_{c-j\infty}^{c+j\infty} \frac{\exp(s\gamma)}{\prod_{k=1}^{M}(1 + s\lambda_k)} ds \tag{4.41}$$

A comparison of Eq. (4.33) with Eq. (4.41) shows that the power level for an independently fading diversity branch can be replaced by the eigenvalues in Eq. (4.40).

4.3 Dual-linear Polarization Stacked Element

A dual-polarization stacked antenna is designed, simulated and measured. Its performance in terms of isolation, vertical and horizontal radiation patterns, far-field coupling, output power correlation as well as diversity gain are evaluated in the following sections using the equations from Section 4.2.

4.3.1 Geometry

The design consists of two layers of dielectric, namely the top and bottom layers which are made up of 0.8mm thick substrates (Rogers 4003, $\varepsilon_r = 3.38$) having dimensions of 150mm × 150mm. The underside of the bottom layer is entirely covered with foil and grounded. Two square patches are, respectively, etched onto the underside of the top layer and the topside of the bottom layer. The spacing between the two layers supported by four plastic stands is s, and the two concentric patches are parallel to and facing each other as shown in Fig. 4.3.1. The dimensions for the top ($l_t \times l_t$) and the bottom ($l_b \times l_b$) patches are selected such that the resonances occur within the frequency band of interest. The lower patch is orthogonally fed on two adjacent sides by microstrip lines of a 3.5mm width.

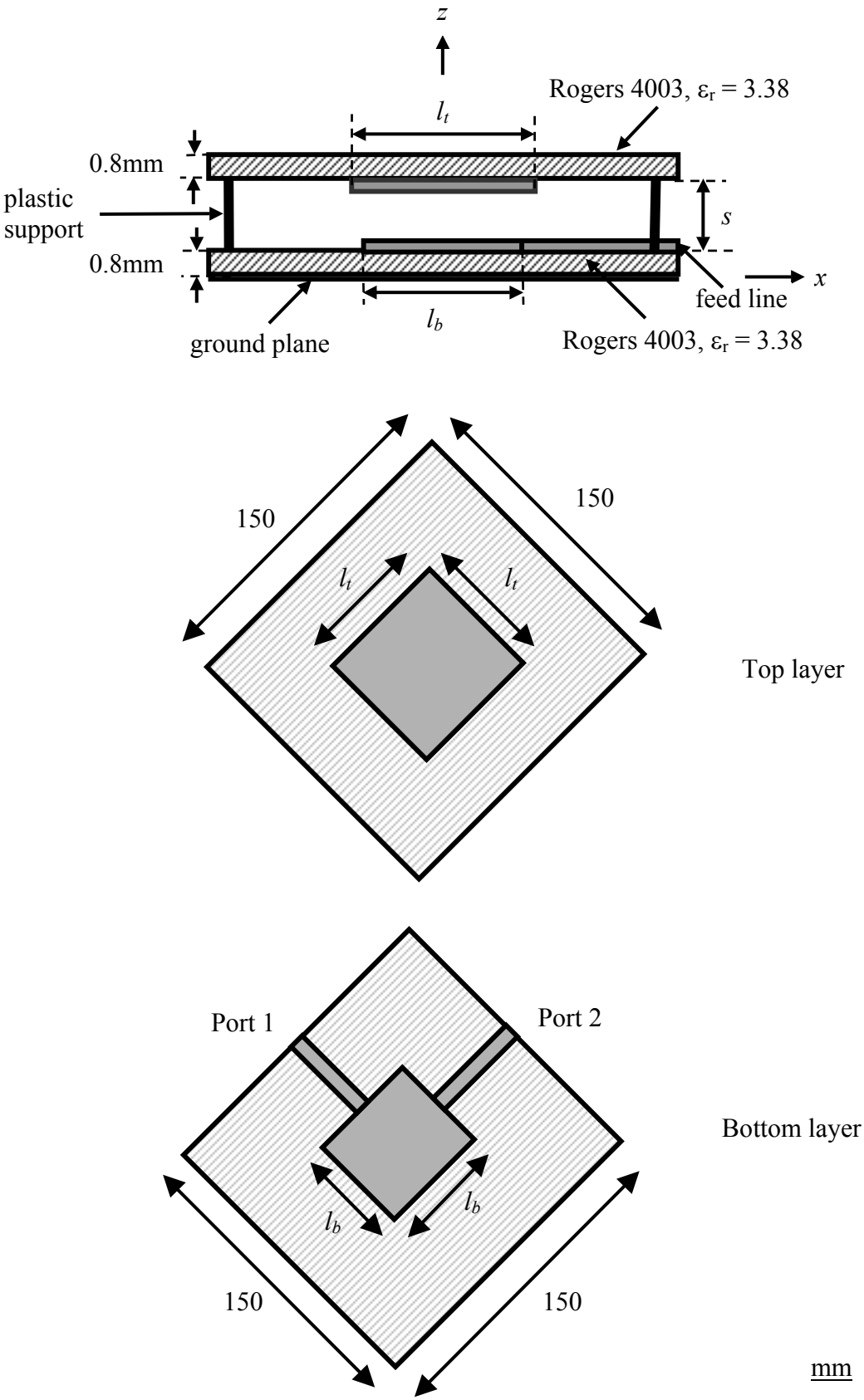

Fig. 4.3.1: Geometry of a stacked dual-linear polarized element

4.3.2 Impedance Performance

The proposed geometry above was simulated using Ansoft Ensemble v8.0. It can be seen from Fig. 4.3.2 for $|S_{11}| \leq -14$dB, the optimum bandwidth achieved is 8% when s = 10mm, l_t = 54mm, and l_b = 40mm. The isolation is more than 24dB across the entire well matched bandwidth.

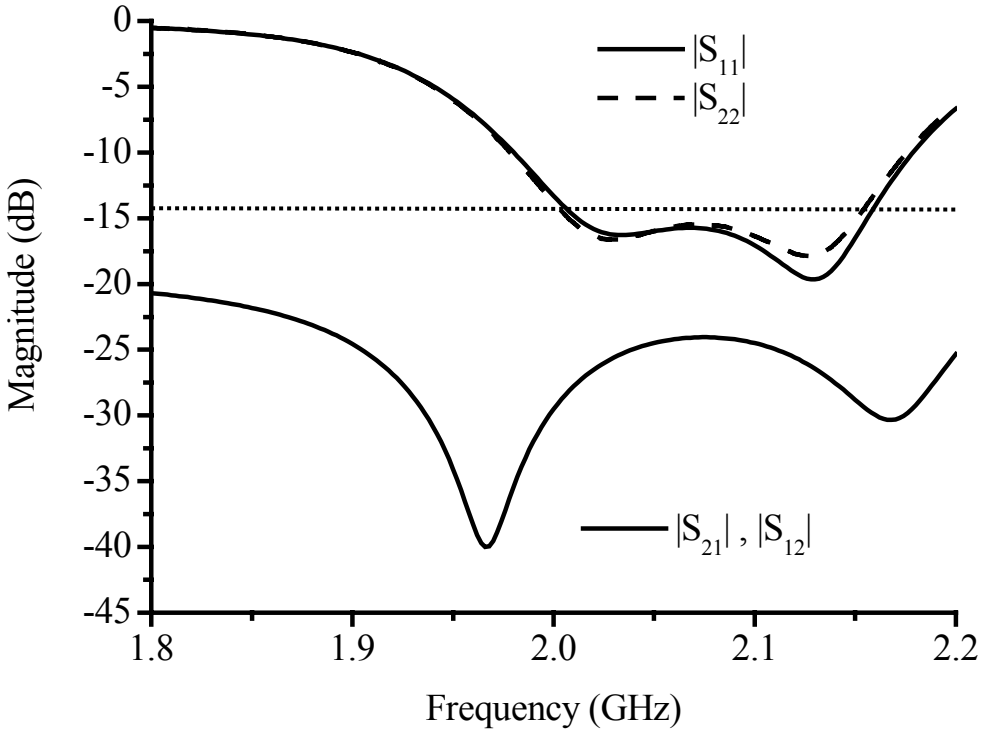

Fig. 4.3.2: Simulated S parameters

The input impedance was measured by an HP8753D Network Analyzer. Fig. 4.3.3 shows the measured S parameters for the proposed antenna. The optimized antenna configuration occurs when l_t = 55mm, l_b = 40mm, and s = 11mm. The measured results show that the antenna achieves a bandwidth of 8% for $|S_{11}| \leq -14$dB, with a center frequency of 1.98GHz that is lower than the simulated result. Also, the measured isolation is greater than 24dB across the entire well matched bandwidth.

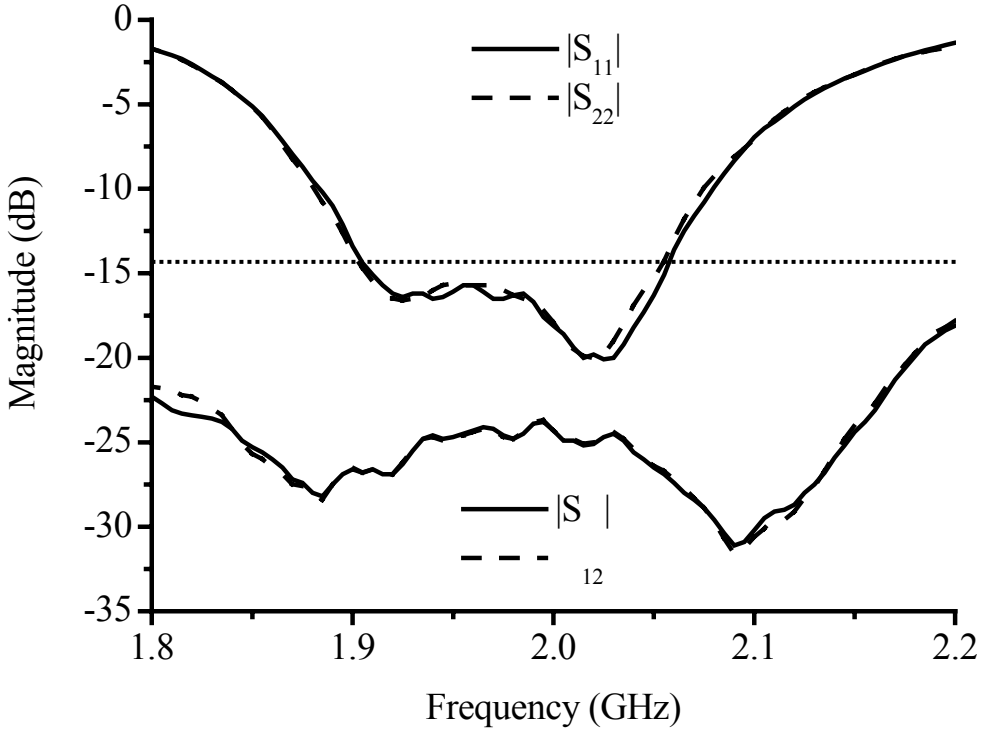

Fig. 4.3.3: Measured S parameters

4.3.3 Radiation Performance

With the antenna positioned in a ±45° configuration, the radiation patterns were measured at 1.91GHz, 1.98GHz, and 2.06GHz, which correspond to the lower, center, and upper frequency of the bandwidth, respectively. Figs. 4.3.4 – 4.3.6 display the simulated and measured responses for the vertical and horizontal polarizations. Each of the radiation levels was normalized by the total received power $\left(\sqrt{|E_\theta|^2+|E_\phi|^2}\right)$. It can be observed that at the three frequencies, the measured responses for the vertical polarizations are close to the simulated responses. The measured and simulated responses for the horizontal polarizations start to deviate after ±70° and the extent of the deviation increases with increasing frequency.

As the difference between the vertical and horizontal radiation levels gets larger than 6dB at a particular angle, the antenna functions more like a vertically polarized antenna and less like a polarization diversity antenna at that angle. The difference in the radiation levels between the simulated responses for the horizontal and vertical polarizations is less than 6dB across the entire azimuth at all the three frequencies. Comparing the measured responses for the vertical and horizontal polarizations, at the lower frequency, the difference is less than 6dB within a coverage of 135°. However, at the center frequency, the coverage is reduced to 110° and reduced further to 100° at the upper frequency. Here, it is noted that the finite-size ground plane and the cable placement in the measurements has led to an increase in the vertical polarization radiation as compared to the simulated results at the higher angles outside the main beam. As a result, the difference between the measured vertical and horizontal polarizations becomes more pronounced outside the main beam.

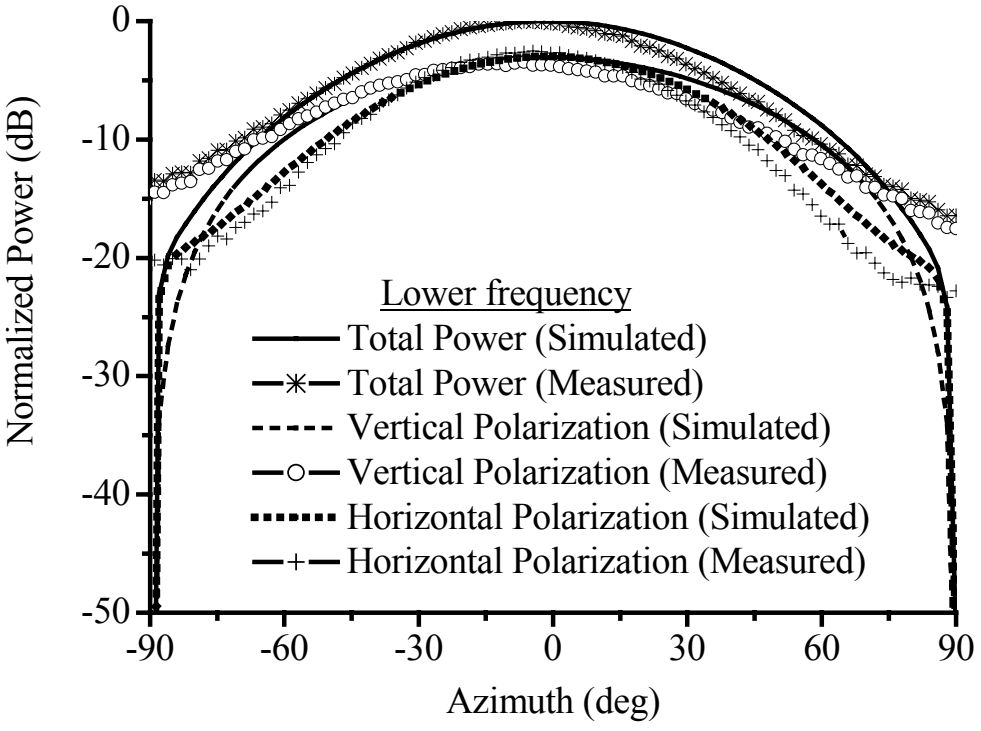

Fig. 4.3.4: Measured and simulated radiation patterns at lower frequency

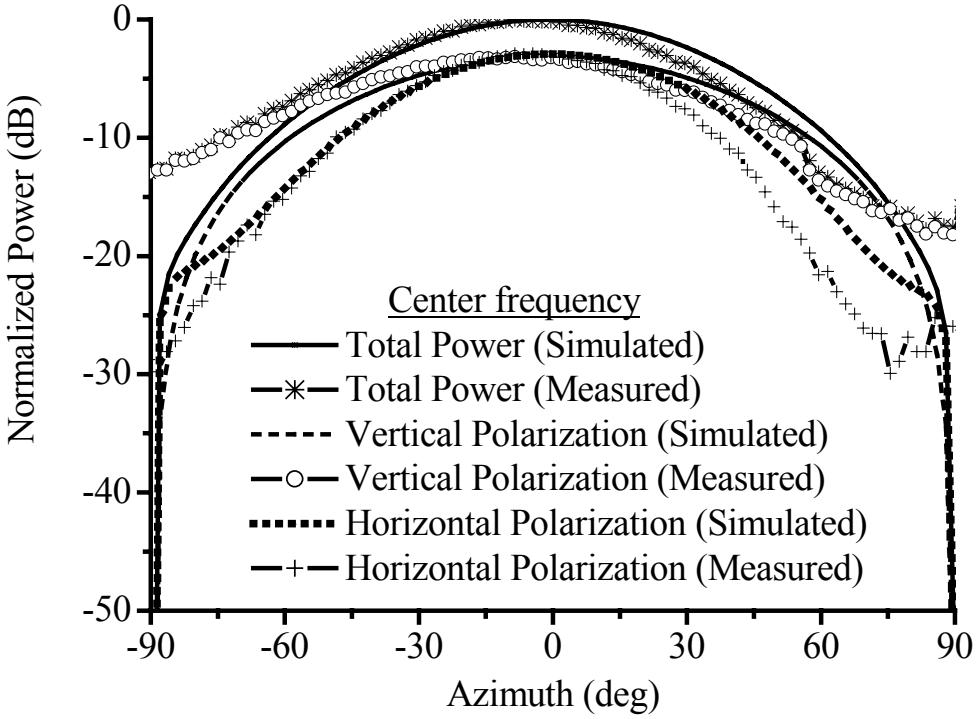

Fig. 4.3.5: Measured and simulated radiation patterns at center frequency

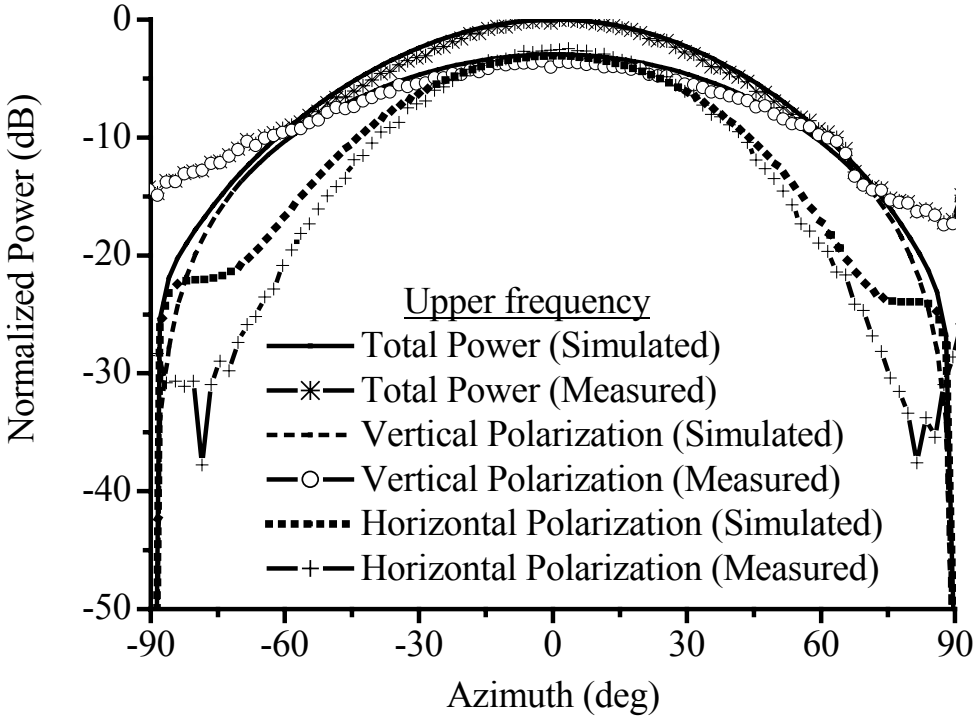

Fig. 4.3.6: Measured and simulated radiation patterns at upper frequency

4.3.4 Far-field Coupling

Using Eq. (4.17) when $\chi = 1$, the far-field coupling σ between the two branches can be computed by taking the inner product of the complex port vectors [Lin01].

$$\sigma = \frac{E_{\theta 1}E_{\theta 2}^{*} + E_{\phi 1}E_{\phi 2}^{*}}{\left(\sqrt{(E_{\theta 1})^2 + (E_{\phi 1})^2}\right)\left(\sqrt{(E_{\theta 2}^{*})^2 + (E_{\phi 2}^{*})^2}\right)}$$

$$= \frac{E_{\theta 1}E_{\theta 2}^{*} + E_{\phi 1}E_{\phi 2}^{*}}{E_1 E_2^{*}} \tag{4.42}$$

where $E_{\theta 1,\ \phi 1}$ and $E_{\theta 2,\ \phi 2}$ correspond to the antenna pattern vectors in Port 1 and 2, respectively, and $E_1 = \sqrt{(E_{\theta 1})^2 + (E_{\phi 1})^2}$, $E_2^{*} = \sqrt{(E_{\theta 2}^{*})^2 + (E_{\phi 2}^{*})^2}$.

The expression in Eq. (4.42) can be simplified since the antenna elements exhibit symmetry with respect to the vertical axis. Thus, in the $\theta = 90°$ plane, the radiation patterns will be symmetrical with respect to the $\phi = 45°$ plane as well. With $E_{\theta 2} = e^{-j(\varphi_\theta + \varphi)} E_{\theta 1}$ and $E_{\phi 2} = e^{-j(\varphi_\phi + \varphi)} E_{\phi 1}$, where φ is to account for arbitrary phase difference between the two ports during measurement, φ_θ and φ_ϕ are the phase difference for the E_θ and E_ϕ components, respectively. In this Chapter, the orientation of the feed-points with respect to the co-ordinate axes gives $\varphi_\theta = 0$ and $\varphi_\phi = \pi$. For simplicity, it is assumed that there is no phase difference from measurement, i.e. $\varphi = 0$.

$$\sigma = \frac{|E_{\theta 1}|^2 - |E_{\phi 1}|^2}{|E_1|^2} \tag{4.43}$$

An antenna with zero far-field coupling ensures that all the power incident on the antenna aperture is received at the antenna outputs. The measured far-field coupling at

the lower, center, and upper frequencies were examined and compared against the simulated results.

Figs. 4.3.7 – 4.3.9 show the calculated far-field coupling at the three frequencies using the simulated and measured antenna patterns. From the graphs, the simulated responses indicate a greater coupling at about ±65°. The measured coupling at the lower frequency of 1.91GHz is below 0.7 across the entire ±90° azimuth. The measured coupling at the centre frequency of 1.98GHz is less than 0.7 within a 127° coverage and deteriorates to 107° at the upper frequency of 2.06GHz. At the lower and upper frequencies, it can be observed that the measured coupling at ±20°-30° is the minimum with a local maximum at the boresight. At the center frequency, the measured and simulated coupling is minimum at the boresight. Comparing Figs. 4.3.7 – 4.3.9 with Figs. 4.3.4 – 4.3.6, it can also be seen from Eq. (4.43) that the coupling is zero when the power for the vertical and horizontal polarizations are equal.

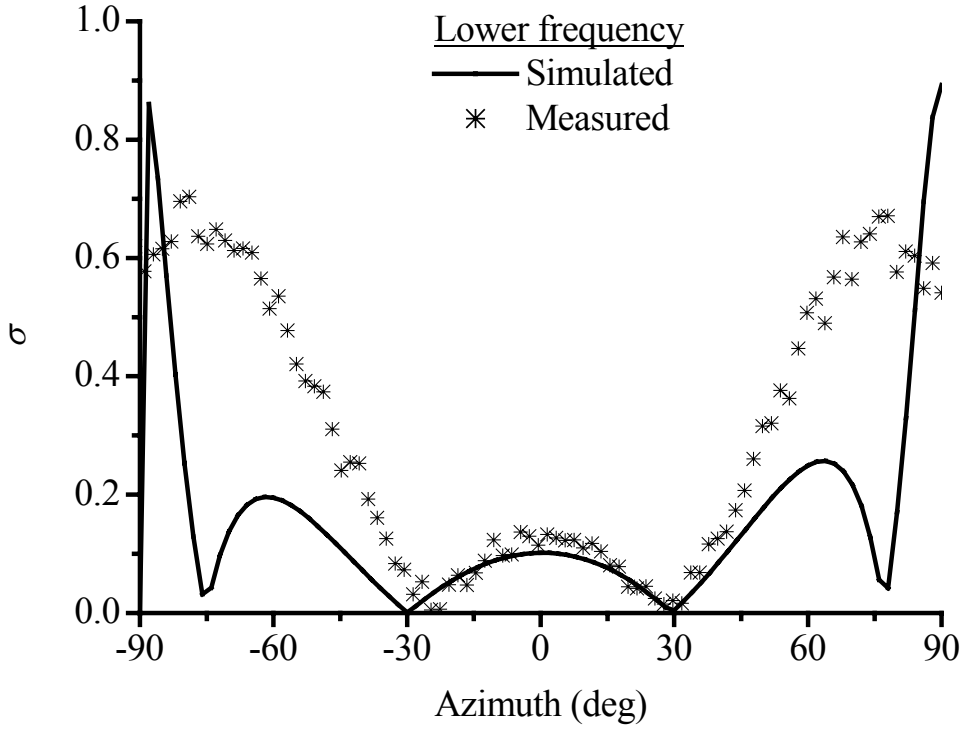

Fig. 4.3.7: Measured and simulated far-field coupling σ at lower frequency

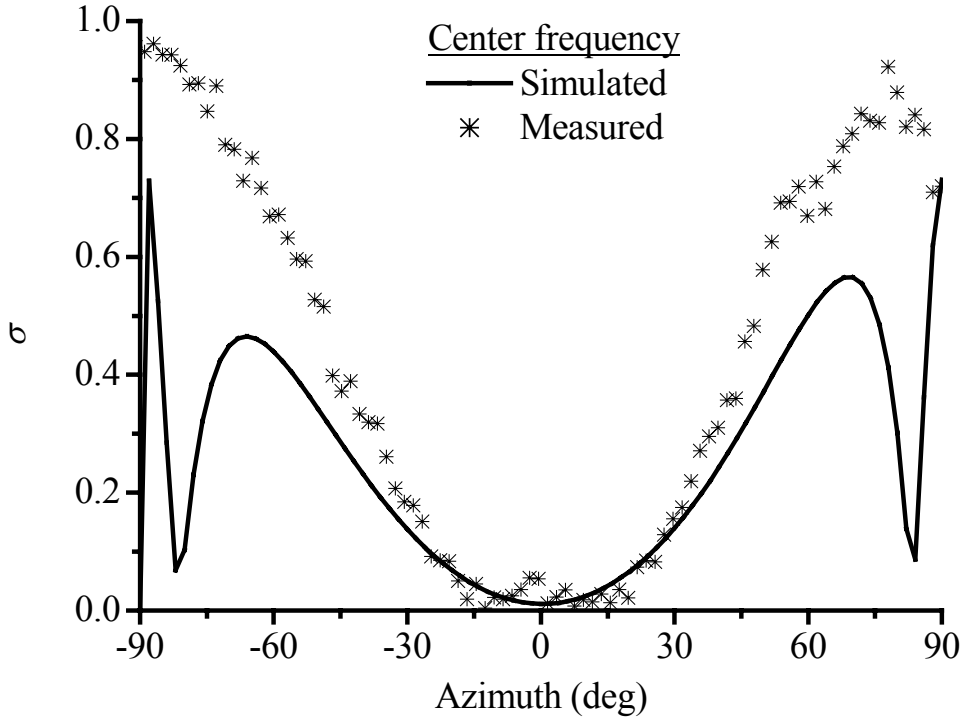

Fig. 4.3.8: Measured and simulated far-field coupling σ at center frequency

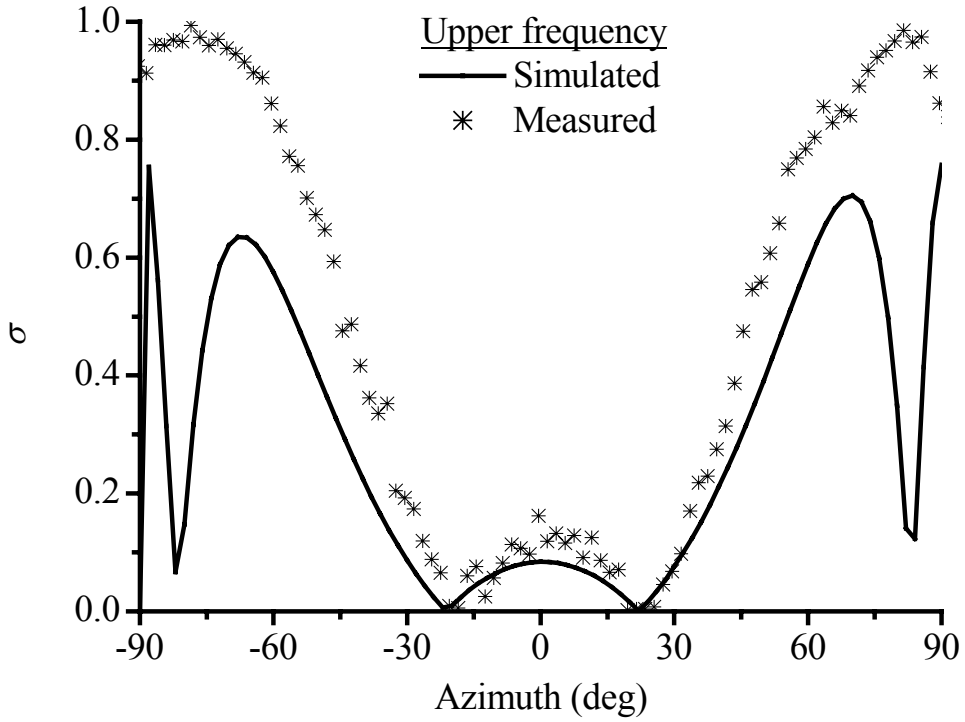

Fig. 4.3.9: Measured and simulated far-field coupling σ at upper frequency

4.3.5 Output Power Correlation

The output power correlation ρ has been shown to be dependent on the cross-polar discrimination χ [Vau87].

$$\rho = \left(\frac{\chi\left(E_{\theta 1}E_{\theta 2}^{\ *}\right) + E_{\phi 1}E_{\phi 2}^{\ *}}{E_1 E_2^{\ *}} \right)^2$$

where the cross-polar discrimination is defined as the ratio of the vertically polarized to the horizontally polarized E-field in the far zone.

$$\chi(\theta,\phi) = \frac{\left|E_\theta(\theta,\phi)\right|}{\left|E_\phi(\theta,\phi)\right|} \tag{4.45a}$$

$$= 20\log_{10}\frac{\left|E_\theta(\theta,\phi)\right|}{\left|E_\phi(\theta,\phi)\right|}\text{dB} \tag{4.45b}$$

Since the antenna elements are symmetrical with respect to the vertical axis, Eq. (4.44) can be simplified to give,

$$\rho = \left(\frac{\chi\left|E_{\theta 1}\right|^2 - \left|E_{\phi 1}\right|^2}{\chi\left|E_{\theta 1}\right|^2 + \left|E_{\phi 1}\right|^2} \right)^2 \tag{4.46}$$

It is well-known in available literature that, for $\rho \leq 0.7$ at the base station, effective diversity combining can be achieved [Bre59][Lee72][Jak74].

The cross-polar discrimination can be influenced primarily by channel fading as well as the antenna polarization. The effects of channel cross-polar discrimination on output power correlation have been discussed [Lin01], based on the assumption that the dual-polarized antennas are ideal in that the vertical and horizontal polarized patterns are equal over the entire azimuth.

Instead of considering the environmental influence on χ for an ideal dual-polarized antenna, the effects of antenna polarization on χ can also be investigated in the presence of a non-fading channel. Figs. 4.3.10 – 4.3.12 compare the simulated and measured output power correlation at the lower, center, and upper frequencies. The measured and simulated cross-polar discrimination responses are also included for discussion. From the measured results, the output power correlation is generally less than 0.7 within a 126° sector at the lower frequency, 100° at the center frequency and 93° at the upper frequency. However, the simulated results show that for a correlation of less than 0.7, the coverage at the lower frequency is ±82° while at the center and upper frequencies, the coverage is ±54° and ±50°, respectively. From the figures, it can be observed that the increase in the simulated and measured output power correlation attributes to the significant increase in the antenna cross-polar discrimination.

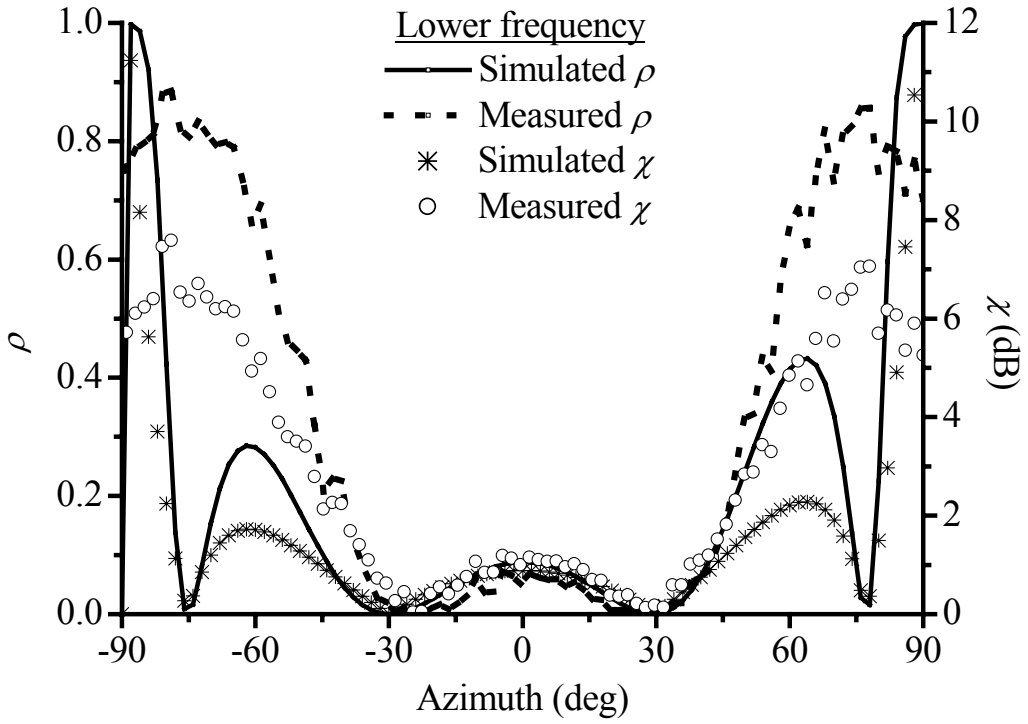

Fig. 4.3.10: Measured and simulated output power correlation ρ and cross-polar discrimination χ at lower frequency

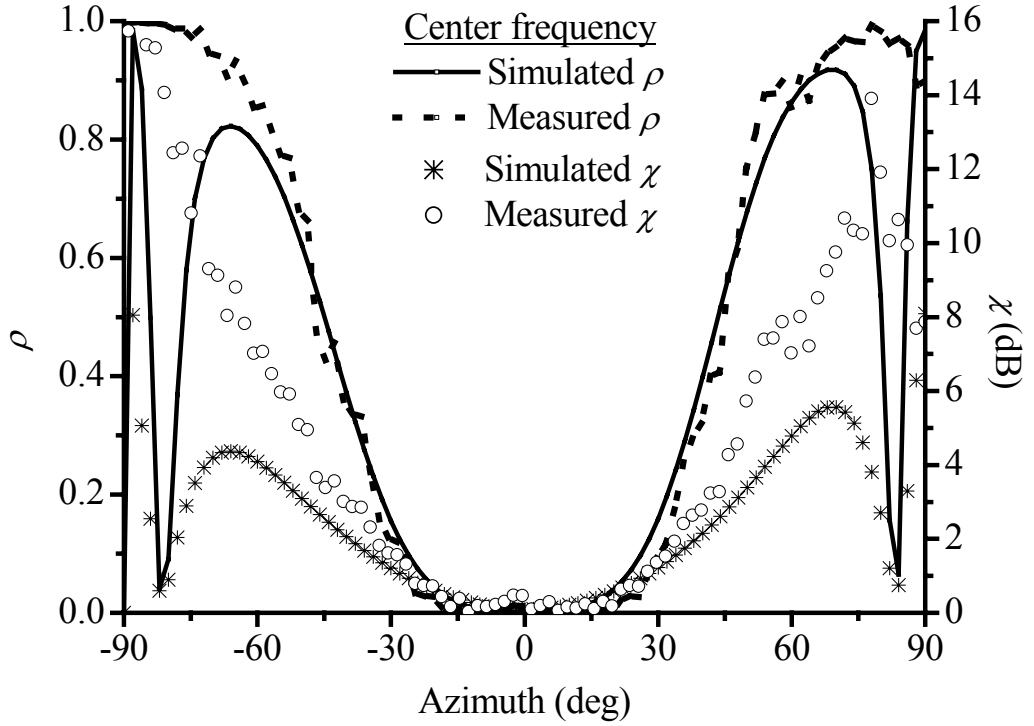

Fig. 4.3.11: Measured and simulated output power correlation ρ and cross-polar discrimination χ at center frequency

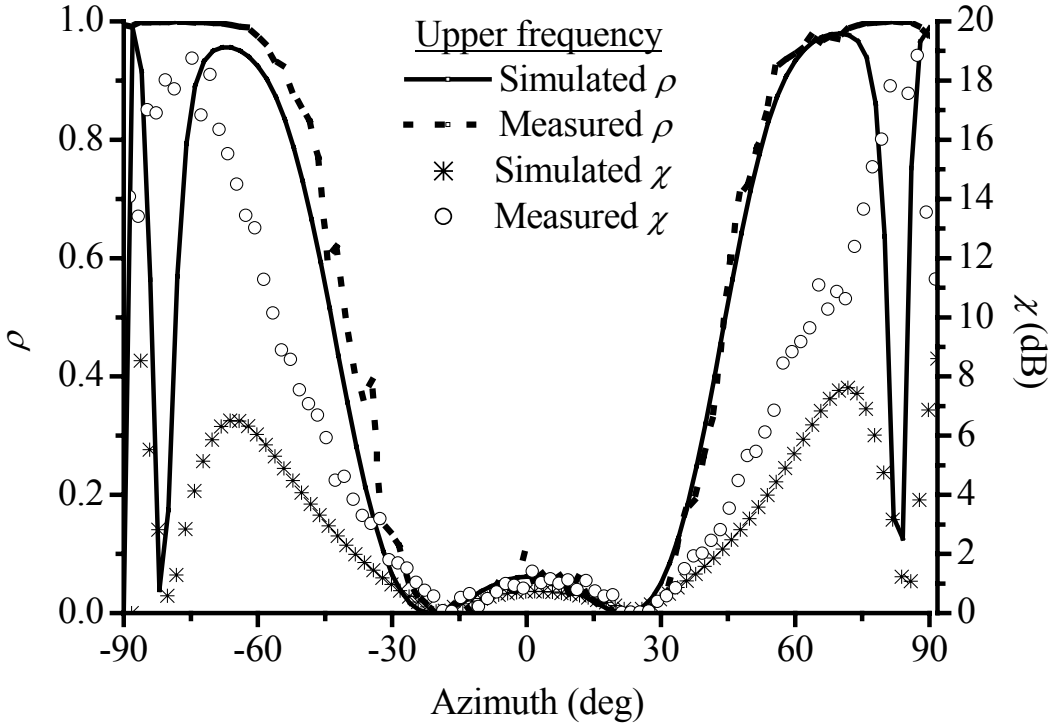

Fig. 4.3.12: Measured and simulated output power correlation ρ and cross-polar discrimination χ at upper frequency

From Table 4.3.1 [Lin01], it can be seen that the interval $0 < \chi < 6$dB due to the channel in an urban-suburban environment is a good representation. It must be noted that the cross-polar discrimination values provided in the Table are based on a Rayleigh fading channel and assuming that the dual-polarized antenna is ideal (i.e. identical patterns in both vertical and horizontal polarizations).

With this, the effects of χ caused by the channel on the output power correlation coefficient are examined at the center frequency. It can be observed from Fig. 4.3.13, that as χ increases, the entire simulated response for the output power correlation coefficient shifts upwards as can be predicted from Eq. (4.44).

Table 4.3.1: Vertical and horizontal field components in different environment [Lin01]

Environment and source	Mobile Orientation	χ (dB)	Frequency	Correlation ρ_{env}
Urban	Vertical car antenna	4-7	920 MHz	median 0.02
Urban	30° on large groundplane	7	463 MHz	-0.003
Sub-urban		12		0.019
Urban & sub-urban	0°	10	1790 MHz	<0.7 for 95%
	45°	4.6-6.3		<0.7 for 95%
Urban	70±15° in- and outdoor	1-4	1821 MHz	<0.2 for 90%
Sub-urban		2-7		<0.1 for 90%
Urban & sub-urban	0°	4-7	1848 MHz	<0.5 for 93%
	45°	0		<0.5 for 93%
Urban	Car mounted monopole	7.6 ± 2.1	970 MHz	0.09 ± 0.09
Urban & sub-urban	Random, in- and outdoor	< 5 dB	1739 MHz	-0.25 to 0.24
Sub-urban	0° and 45°	7	1800 MHz	<0.2

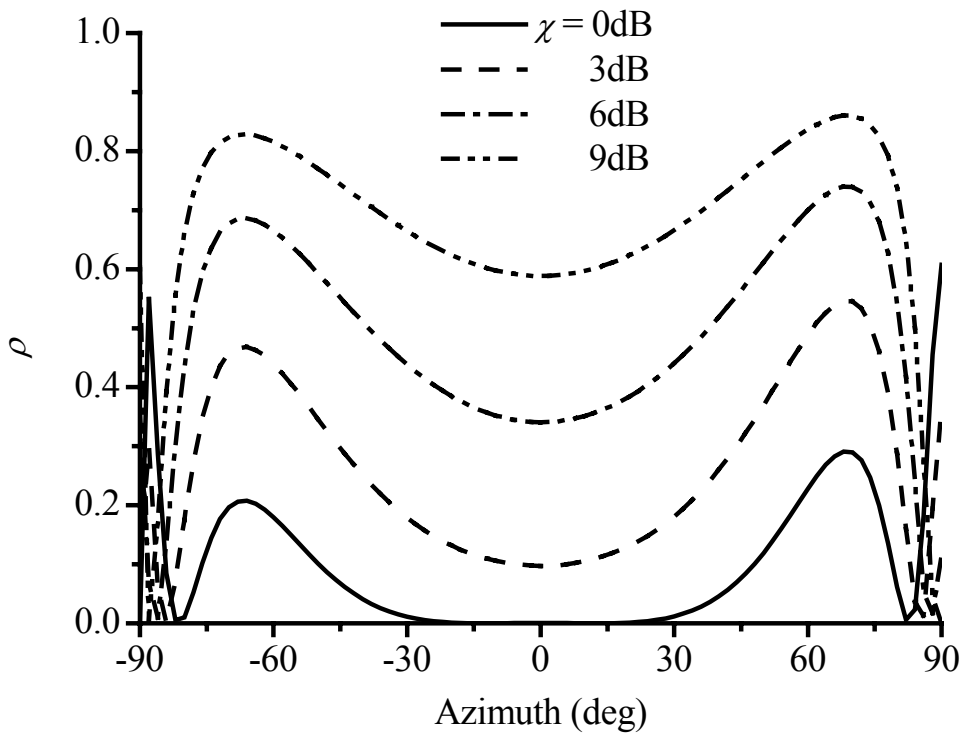

Fig. 4.3.13: Simulated output power correlation coefficient ρ for different cross-polar discrimination χ

4.3.6 Diversity Gain

The diversity performance of an antenna can be evaluated in terms of the diversity gain. In a single branch system, we can measure the level of a signal which is exceeded for some fraction of time, e.g. 90%. If we consider the diversity system, the signal level exceeded for the same proportion of the available time can be determined. The increase in signal levels available for the same proportion of time (reliability) is known as the diversity gain.

The diversity gain can be calculated by finding the eigenvalues from Eq. (4.40), which in turn can be substituted into the probability distribution functions given in Eqs. (4.34) and (4.36) by replacing the Γ by the eigenvalues. By using MATLAB, the value

of φ at each angle can be found for a given outage rate (e.g. 1%), which is the percentage of time when a signal is below a particular threshold φ. This φ is then subtracted from the corresponding φ for a vertically polarized antenna, which can be evaluated by setting λ_1 to be $\chi/(\chi+1)$ and λ_2 to be zero.

The simulated and measured diversity gain performances at 1% outage rate at the three frequencies are shown in Figs. 4.3.14 – 4.3.16. The maximum diversity gain of 11.7dB occurs when the far-field coupling is at its minimum and when χ = 0dB.

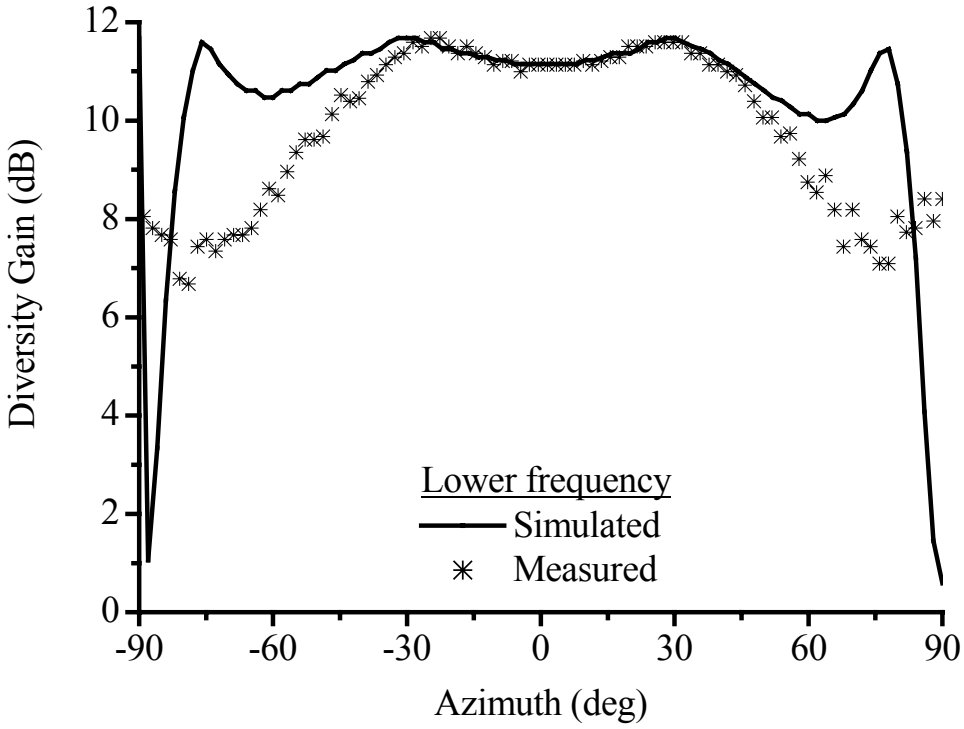

Fig. 4.3.14: Measured and simulated diversity gain at lower frequency

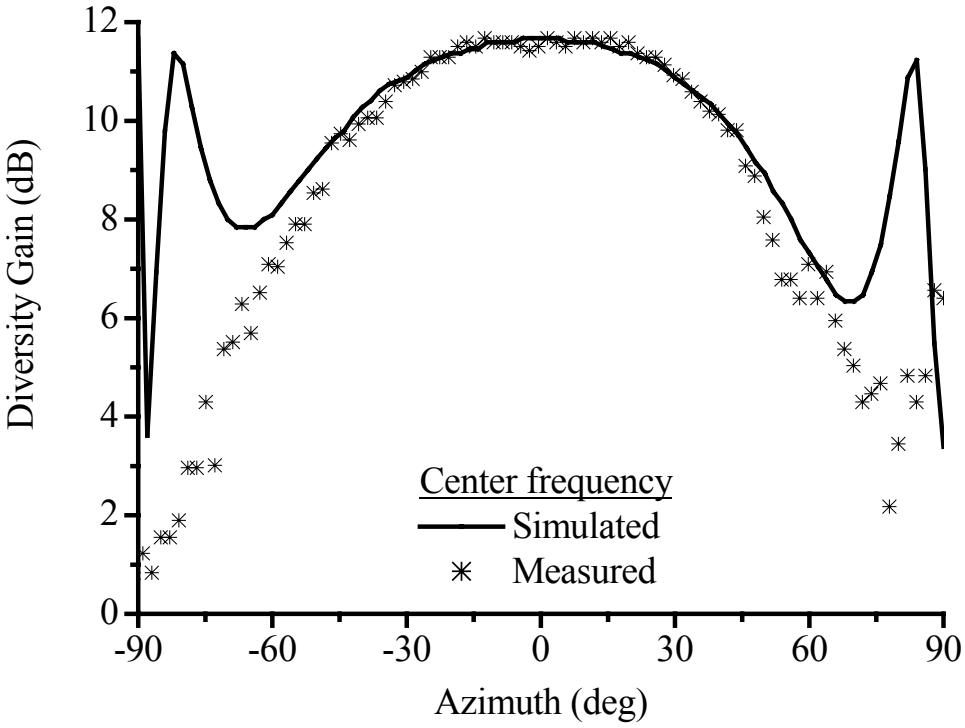

Fig. 4.3.15: Measured and simulated diversity gain at center frequency

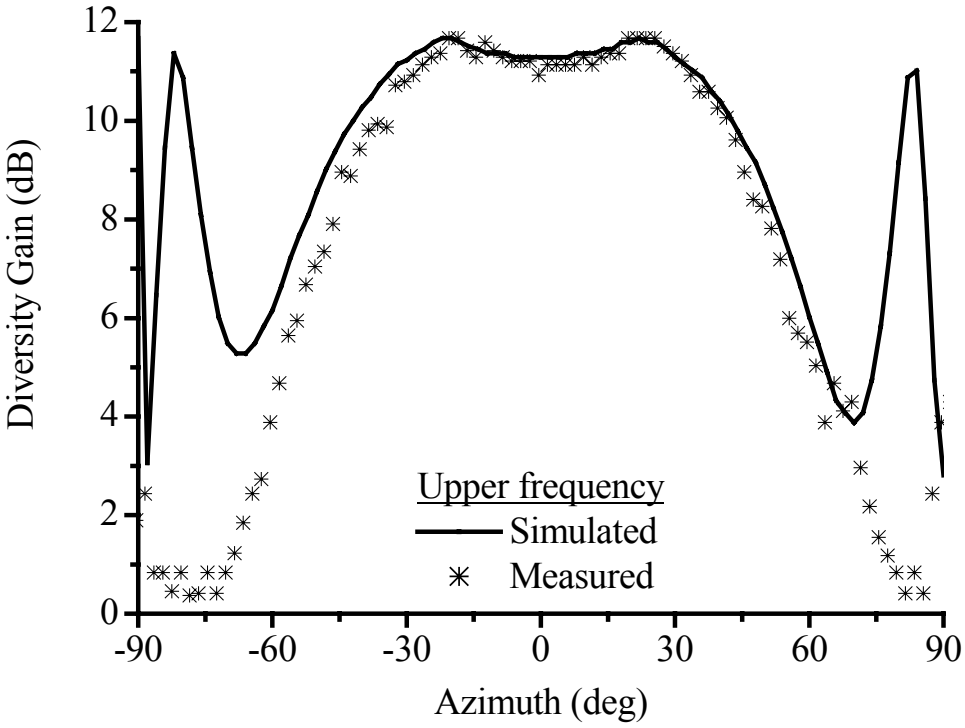

Fig. 4.3.16: Measured and simulated diversity gain at upper frequency

The simulated and measured diversity gain within a 120° sector at the three frequencies are shown in Table 4.3.2 for comparison. At the boresight, the slight dip in the simulated and measured diversity gain at the lower and upper frequencies is caused by the increase in the cross-polar discrimination and the far-field coupling. This can be shown from Eqs. (4.35), (4.37), and (4.40) that the SNR γ, is dependent on the eigenvalues, which are the functions of cross-polar discrimination χ and far-field coupling σ. The degradation in measured diversity gain at the boresight is 0.5dB at the lower frequency and 0.7dB at the upper frequency. The diversity gain approaches zero as $\rho \rightarrow 1$. At the three frequencies, the diversity gain is reduced to 75% of the maximum gain when $\rho = 0.7$.

Table 4.3.2: Measured and simulated diversity gain within a 120° sector at the lower, center, and upper frequencies

	Calculated gain (dB)	**Measured gain (dB)**
Lower frequency	>10.1	>8.6
Center frequency	>7.8	>7.1
Upper frequency	>6.1	>5.0

An analysis on the effects of different values of χ (assuming an ideal dual-polarized antenna) on the diversity gain is also made in Fig. 4.3.17. At χ = 6dB, the maximum diversity gain drops to 8.75dB. Generally, the curve shifts downwards as χ increases. In a space diversity system [Vau90], where the diversity gain is 9.26dB at 1% outage rate, the same effect can be achieved using polarization diversity provided χ < 5dB [Egg83][Wah97]. Thus, if the χ due to the fading channel effects is taken into account, a more stringent requirement on the χ will be required in antenna design.

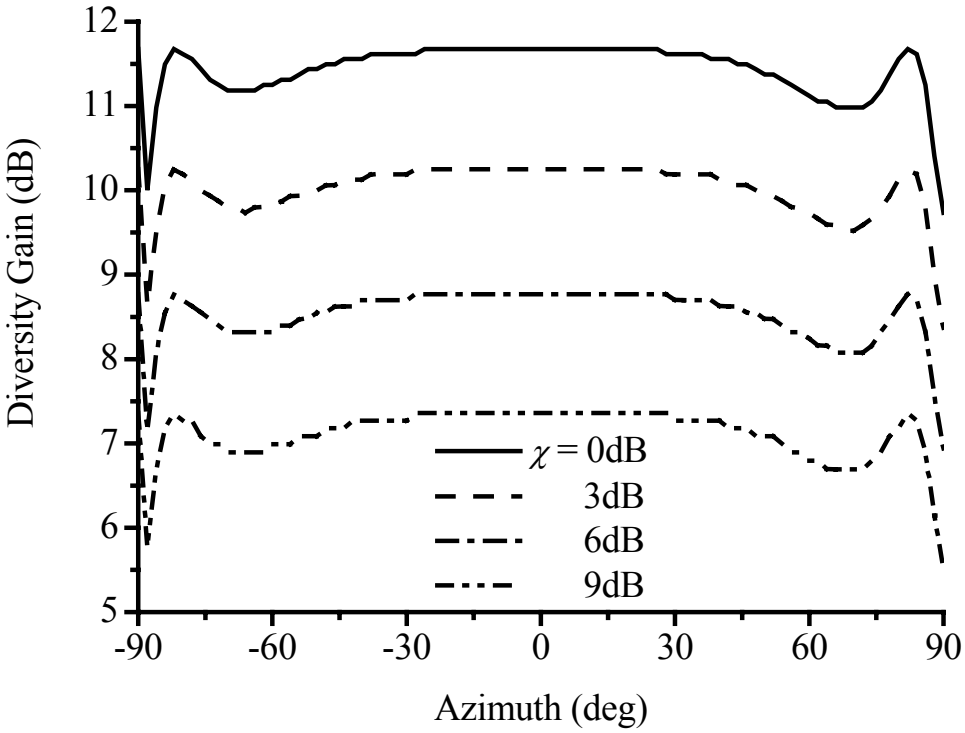

Fig. 4.3.17: Simulated diversity gain for different cross-polar discrimination χ

The effects of outage rate on the diversity gain performance are also investigated in Fig. 4.3.18. The maximum achievable diversity gain is observed to increase with the requirement of the system. For the outage rate of 20%, the maximum gain will be reduced to half of the gain when the outage rate is 1%.

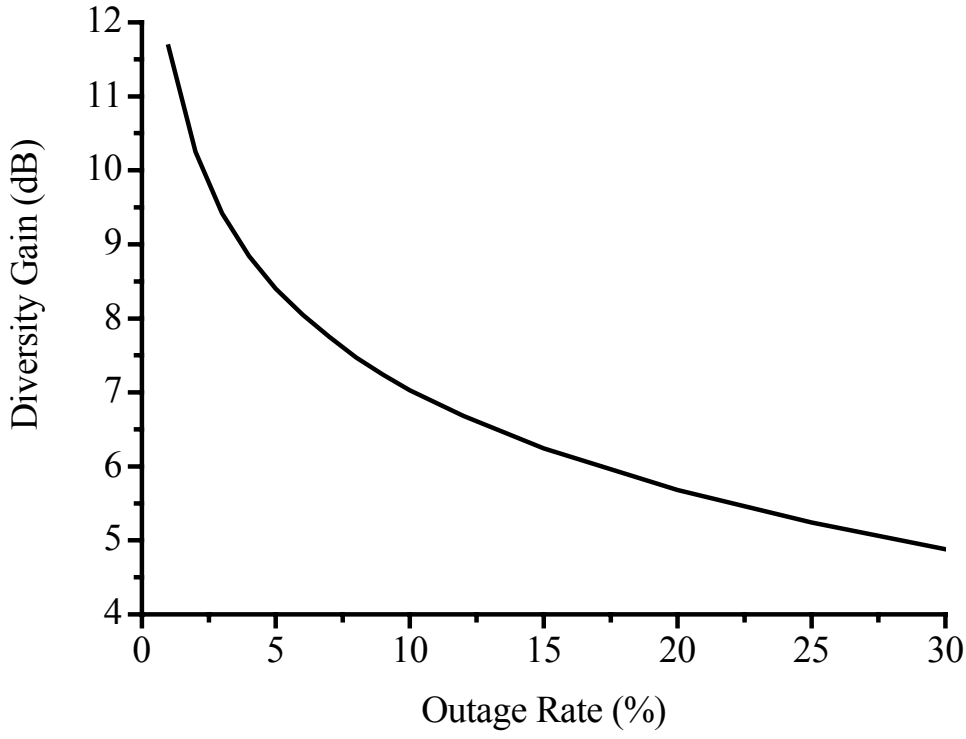

Fig. 4.3.18: Maximum achievable diversity gain as a function of outage rate

4.4 Dual-linear Polarization Stacked Array

Following the analysis of the stacked element above, a 2 × 1 linear array is designed and its impedance as well as diversity performance investigated in the same way as the stacked dual-linear polarized element.

4.4.1 Geometry

As shown in Fig. 4.4.1, the array design consists of the top and bottom dielectric layers made up of a 0.8mm-thick substrate (Rogers 4003, ε_r = 3.38) with dimensions of 200mm × 250mm. The underside of the bottom layer is entirely covered with copper foil and grounded. Two square patches ($l_b \times l_b$) are etched onto the topside of the bottom layer. Two square patches ($l_t \times l_t$) are concentrically positioned on the underside of the top layer and separated by a distance of d. The two patches on the bottom layer are fed via a feeding network designed for optimal performance. The network comprises of a microstrip line ($l_s \times w_s$) fed directly to each patch which can be adjusted in order to obtain good impedance matching. A 25Ω transmission line of a 4.9mm-width is connected in parallel to two 50Ω transmission lines of width 1.85mm. A $\lambda/4$ transformer measuring 21.9mm × 3.1 mm is used to transform the impedance to 50Ω. The spacing between the two dielectric layers supported by four plastic stands is h. The patches arranged in a ±45° configuration, are parallel to and face each other. The dimensions for the top and the bottom patches are selected such that the resonances occur within the frequency band of interest.

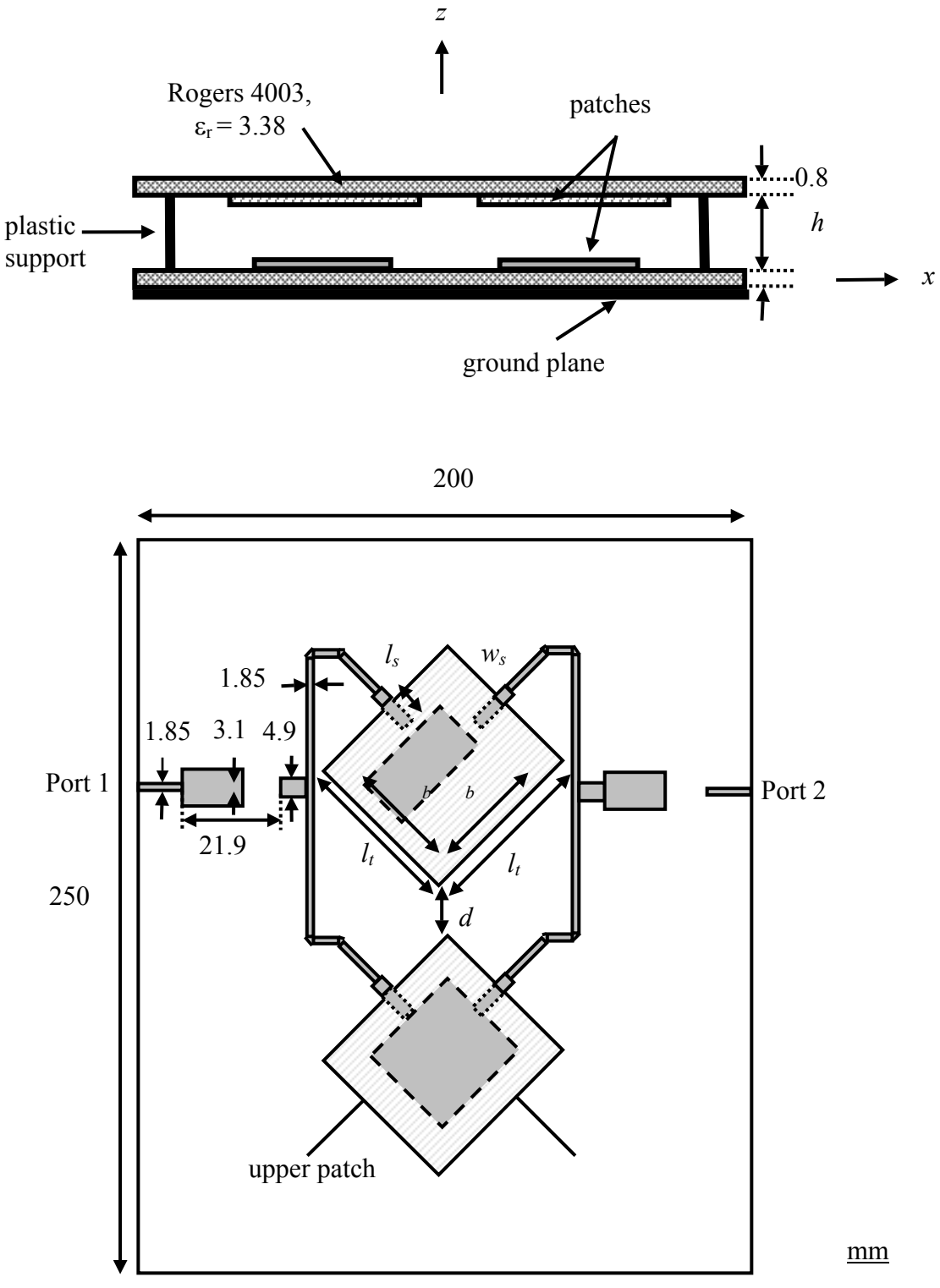

Fig. 4.4.1: Geometry of a stacked dual-linear polarized array

4.4.2 Parametric Study

In this section, a parametric study will be conducted to investigate the influence of physical parameters such as the size of lower and upper patches, separation between the dielectric layers, etc. on the impedance matching. This is done so as to obtain an optimized array configuration to be fabricated.

(a) Effects of varying the size of lower patches

The size of the lower patches l_b was varied from 38mm to 40mm with h = 7.5mm, l_t = 56mm, l_s = 16mm, w_s = 3.6mm, and d = 20mm. According to Figs. 4.4.2 and 4.4.3, varying l_b generally has a significant effect on the resonant frequency. An increase in l_b lowers the resonant frequency. In addition, from the impedance loci, the matching is sensitive to the size of the lower patches. When l_b = 39mm, the loop is observed to rotate to the center but turns outwards in a clockwise manner as l_b increases.

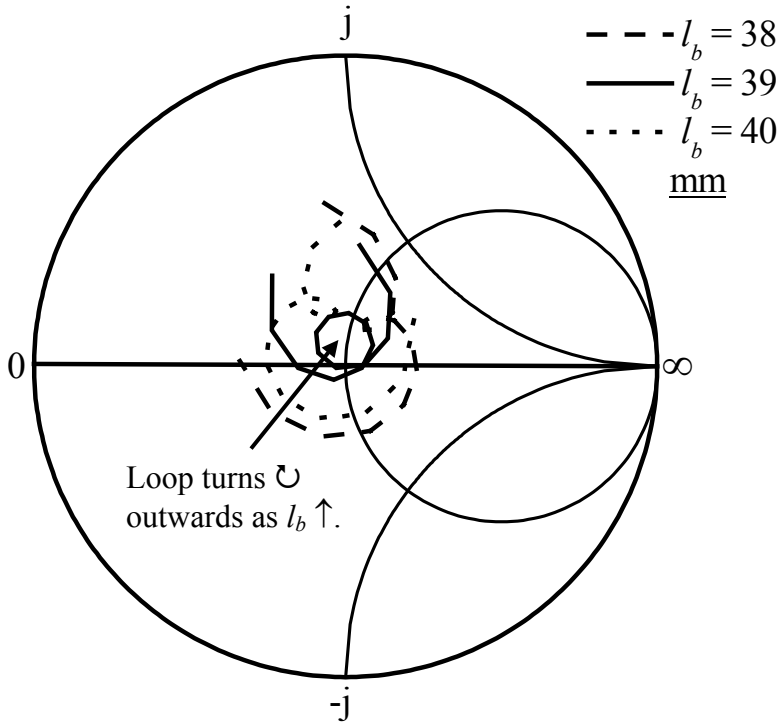

Fig. 4.4.2: Simulated impedance loci for varying size l_b of lower patches

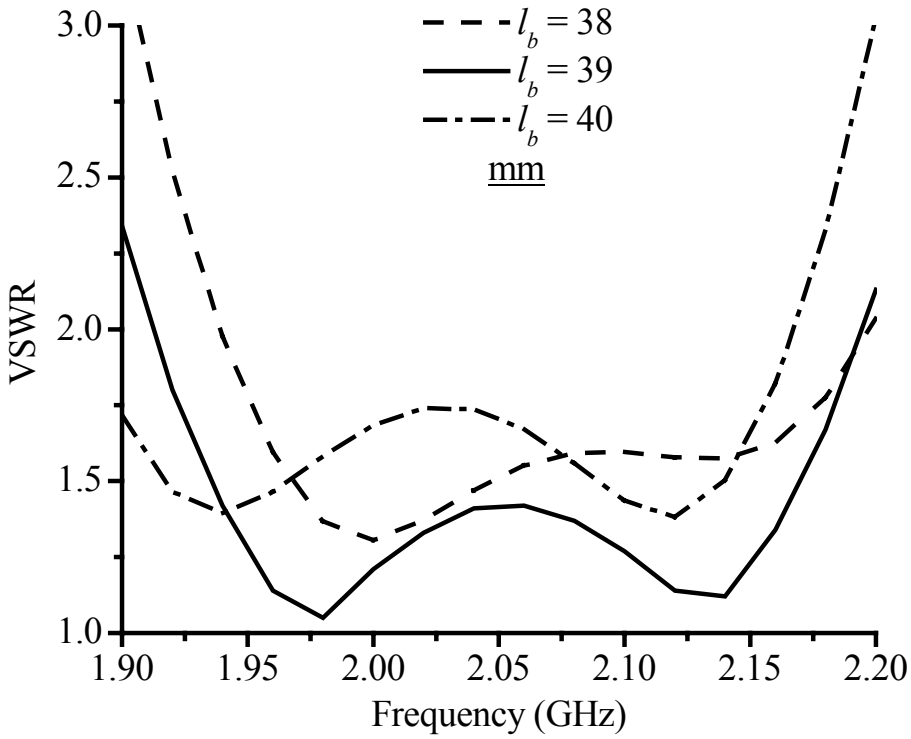

Fig. 4.4.3: Simulated VSWR for varying size l_b of lower patches

(b) Effects of varying the size of upper patches

The size of the upper patches l_t was varied from 55mm to 57mm with h = 7.5mm, l_b = 39mm, l_s = 16mm, w_s = 3.6mm, and d = 20mm. According to Figs. 4.4.4 and 4.4.5, an increase in l_t leads to a decrease in the lower and upper frequencies, while the matching at the center frequency is slightly affected. As l_t increases to 57mm, it can be observed that the matching gets poorer since the loop has rotated outwards in an anticlockwise manner.

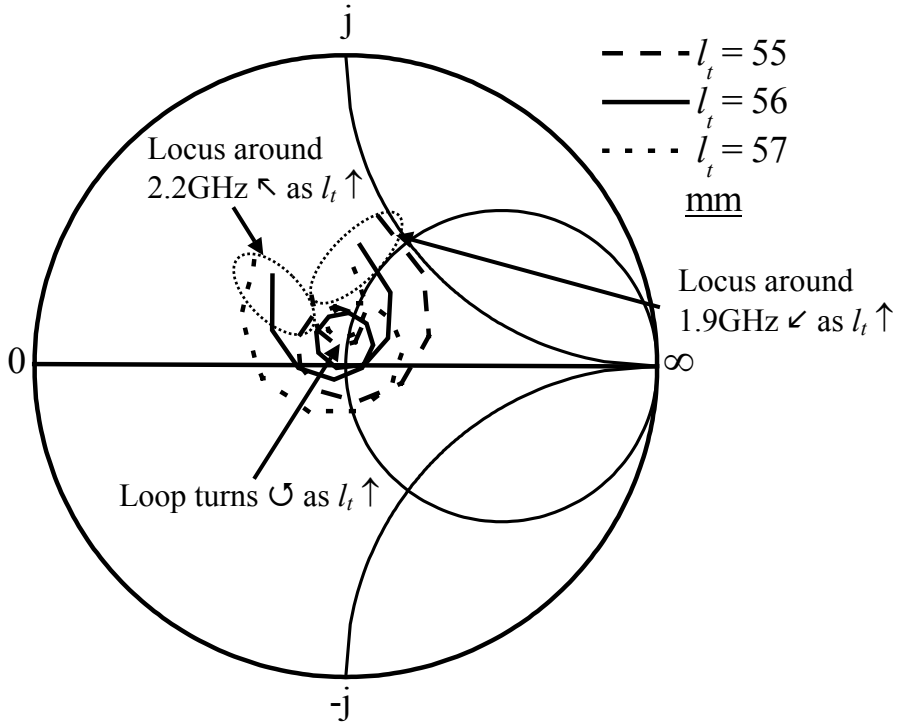

Fig. 4.4.4: Simulated impedance loci for varying size l_t of upper patches

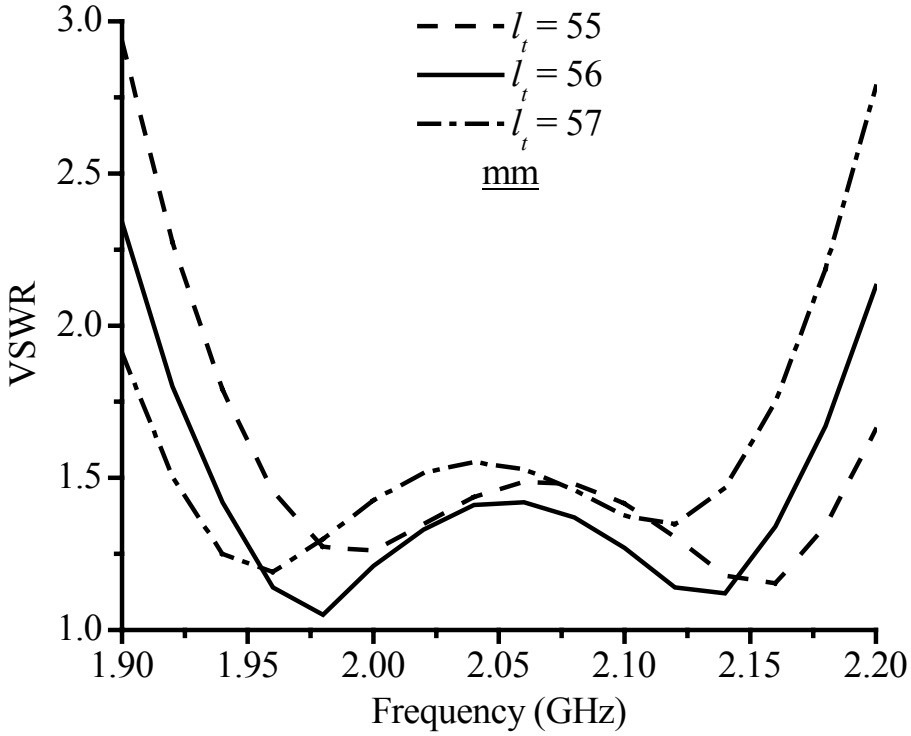

Fig. 4.4.5: Simulated VSWR for varying size l_t of upper patches

(c) Effects of varying the length of microstrip line

The length of the microstrip line l_s was varied from 14mm to 18mm with h = 7.5mm, l_b = 39mm, l_t = 56mm, w_s = 3.6mm, and d = 20mm. According to Figs. 4.4.6 and 4.4.7, an increase in l_s leads to an increase in the lower frequency, and a slight decrease in the upper frequency. The matching at the center frequency is responsive to the changes in the length of the microstrip line. As l_s increases to 18mm, it can be observed from the impedance locus that the size of the loop gets smaller and the frequency points in the vicinity of 1.9GHz are mostly located further from the center of the Smith Chart.

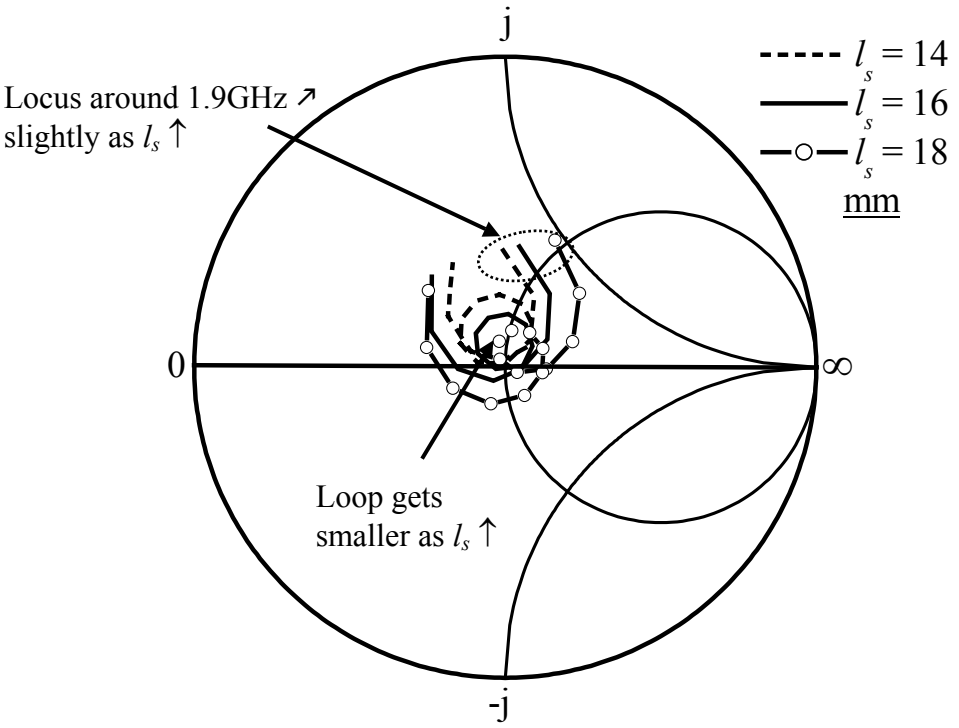

Fig. 4.4.6: Simulated impedance loci for varying length l_s of microstrip line

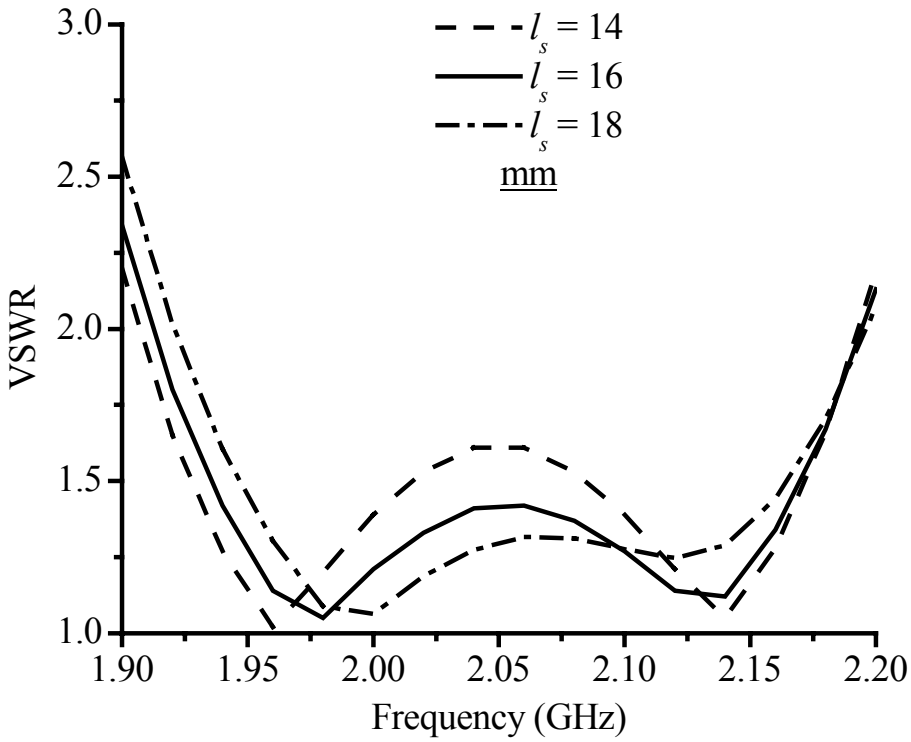

Fig. 4.4.7: Simulated VSWR for varying length l_s of microstrip line

(d) Effects of varying the width of microstrip line

The width of the microstrip line w_s was varied from 3.2mm to 4mm with h = 7.5mm, l_b = 39mm, l_t = 56mm, l_s = 16mm, and d = 20mm. According to Figs. 4.4.8 and 4.4.9, an increase in w_s leads to a decrease in the upper frequency as the frequency points in the vicinity of 2.2GHz are located further from the center of the Smith Chart. The lower frequency is generally unresponsive to changes in w_s. The matching at the center frequency is responsive to the changes in the width of the microstrip line. As w_s increases to 4mm, the impedance locus gradually turns in a clockwise manner and the size of the loop decreases.

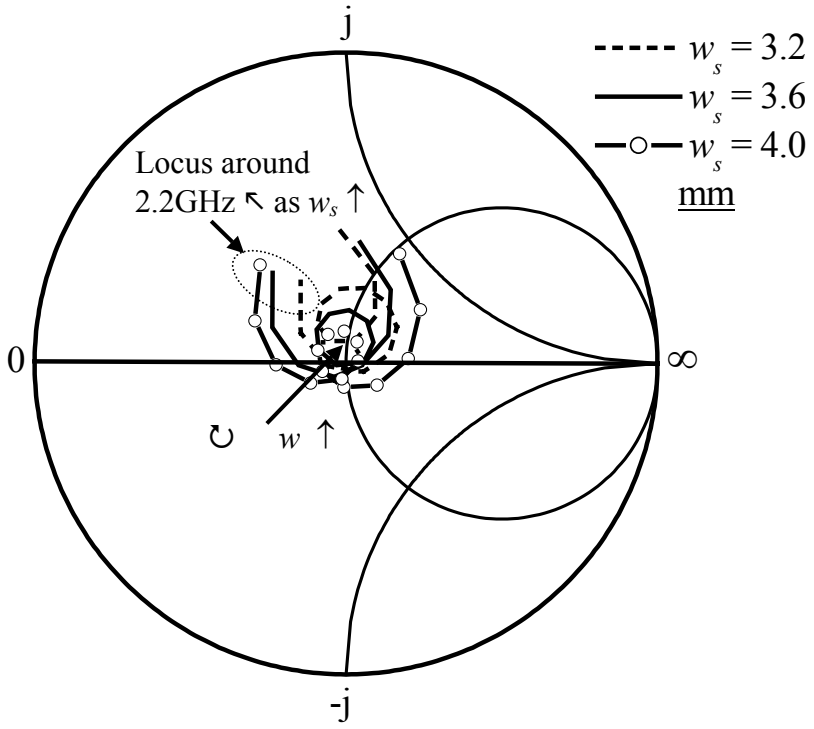

Fig. 4.4.8: Simulated impedance loci for varying width w_s of microstrip line

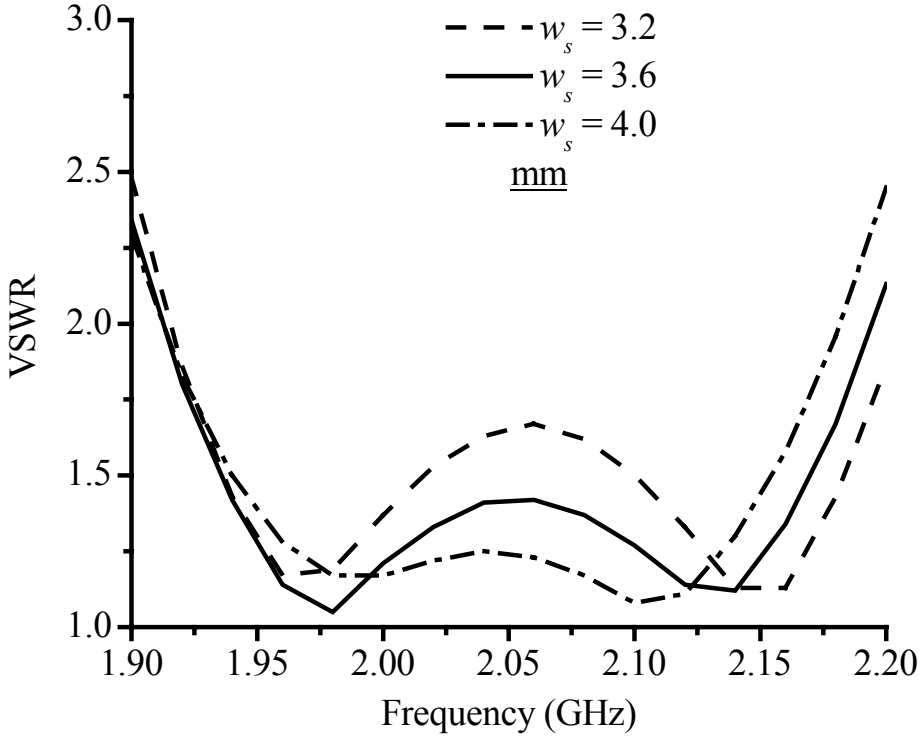

Fig. 4.4.9: Simulated VSWR for varying width w_s of microstrip line

(e) Effects of varying the separation between dielectric layers

The separation h between the dielectric layers was varied from 7mm to 8mm with l_b = 39mm, l_t = 56mm, l_s = 16mm, w_s = 3.6mm, and d = 20mm. According to Figs. 4.4.10 and 4.4.11, an increase in h leads to a decrease in the upper frequency as the frequency points in the vicinity of 2.2GHz move further away from the center of the Smith Chart. The lower frequency is generally unresponsive to the changes in h. The matching at the center frequency is responsive to the changes in the separation between the dielectric layers. The loop size in the impedance locus is very sensitive to the changes in h. As h increases to 8mm, the size of the loop decreases.

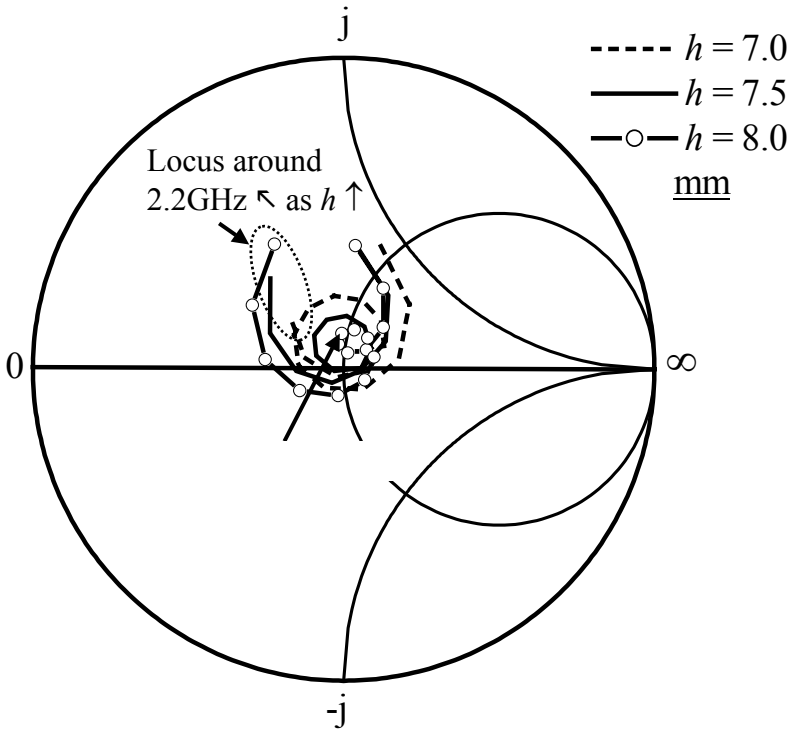

Fig. 4.4.10: Simulated impedance loci for varying separation h between dielectric layers

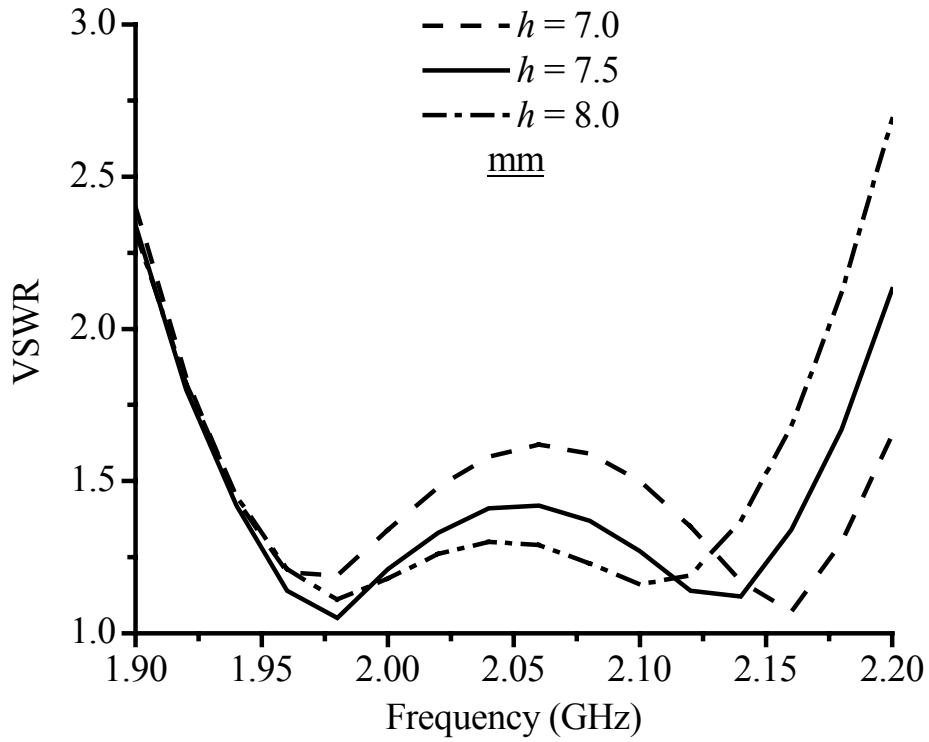

Fig. 4.4.11: Simulated VSWR for varying separation h between dielectric layers

(f) Effects of varying the separation between the patches on $|S_{21}|$

The electromagnetic coupling can be controlled by varying the distance between the patches on the top and bottom layers correspondingly. The separation d between the patches on the top layer was varied from 15mm to 25mm, with l_b = 39mm, l_t = 56mm, l_s = 16mm, w_s = 3.6mm, and h = 7.5mm. According to Fig. 4.4.12, when d > 20mm, the $|S_{21}|$ is generally less than –21dB across the impedance bandwidth. The $|S_{21}|$ at the upper frequency is generally lower than that at the lower frequency by about 3dB, with a minima at around the center frequency of 2.05GHz.

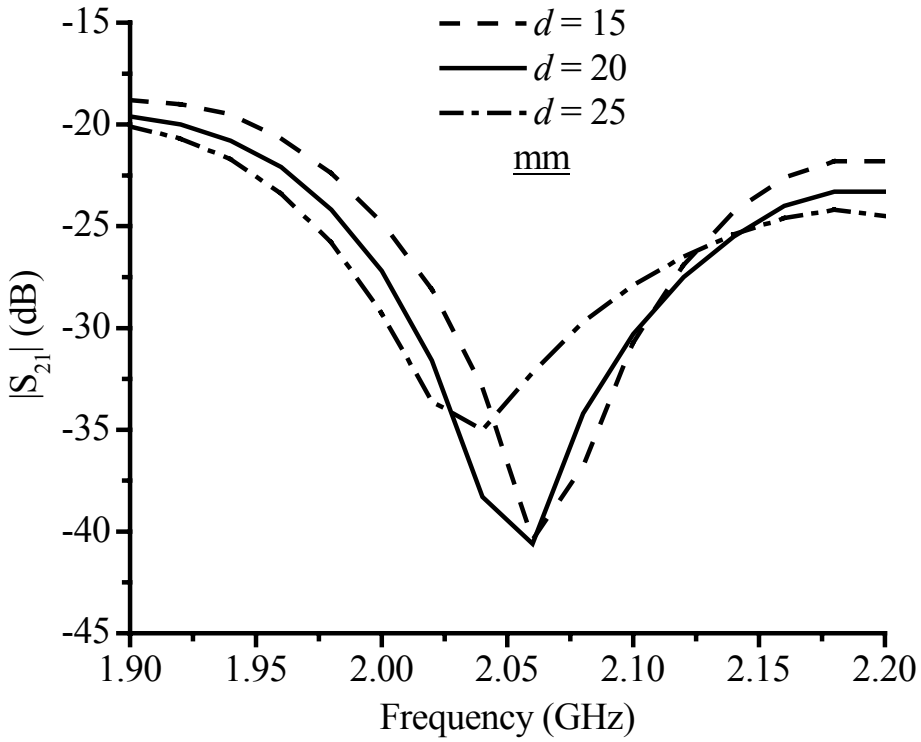

Fig. 4.4.12: Simulated $|S_{21}|$ for varying separation d between patches

4.4.3 Impedance Performance

The proposed geometry shown in Fig. 4.4.1 was simulated using Zeland IE3D. It can be seen from Fig. 4.4.13 for $|S_{11}| \leq -14$dB, the optimum bandwidth achieved is 11.2% (1.94GHz – 2.17GHz) when h = 7.5mm, l_b = 39mm, l_t = 56mm, l_s = 16mm, w_s = 3.6mm, and d = 20mm. The isolation is more than 21dB across the entire well matched bandwidth as shown.

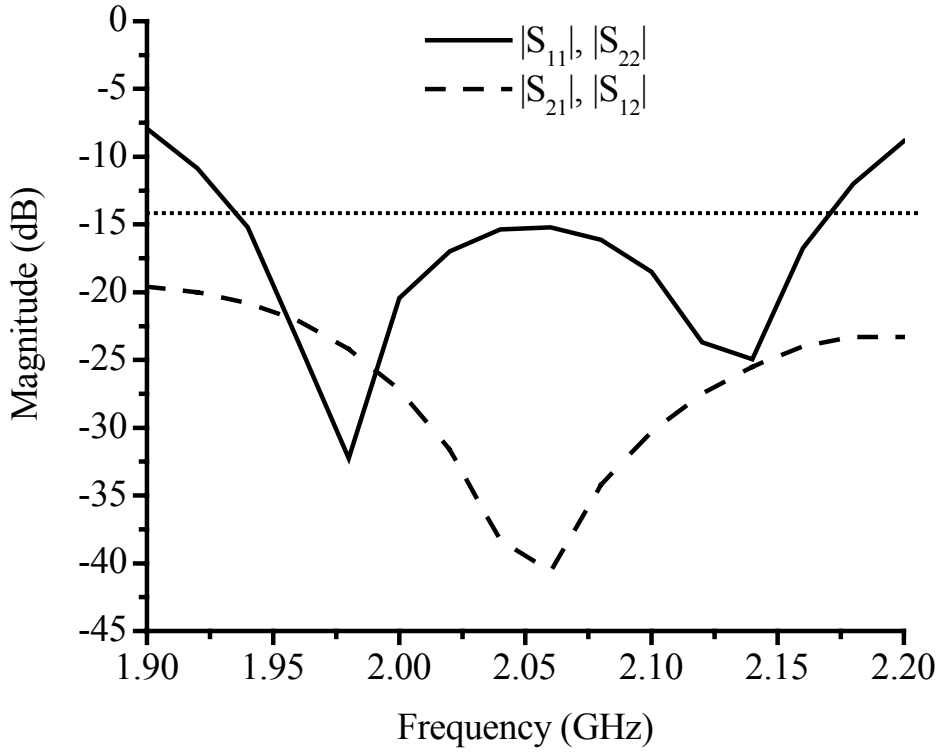

Fig. 4.4.13: Simulated S parameters

With an HP8753D Network Analyzer, the S parameters for the proposed array were measured as shown in Fig. 4.4.14. The optimized antenna configuration occurs when h = 9mm, l_b = 38mm, l_t = 55mm, l_s = 12mm, w_s = 3.6mm, and d = 20mm. The measured results show that the array is able to achieve an $|S_{11}| \leq$ -14dB bandwidth of 12.2% with a center frequency of 2.05GHz. The isolation is more than 18dB across the entire well matched bandwidth.

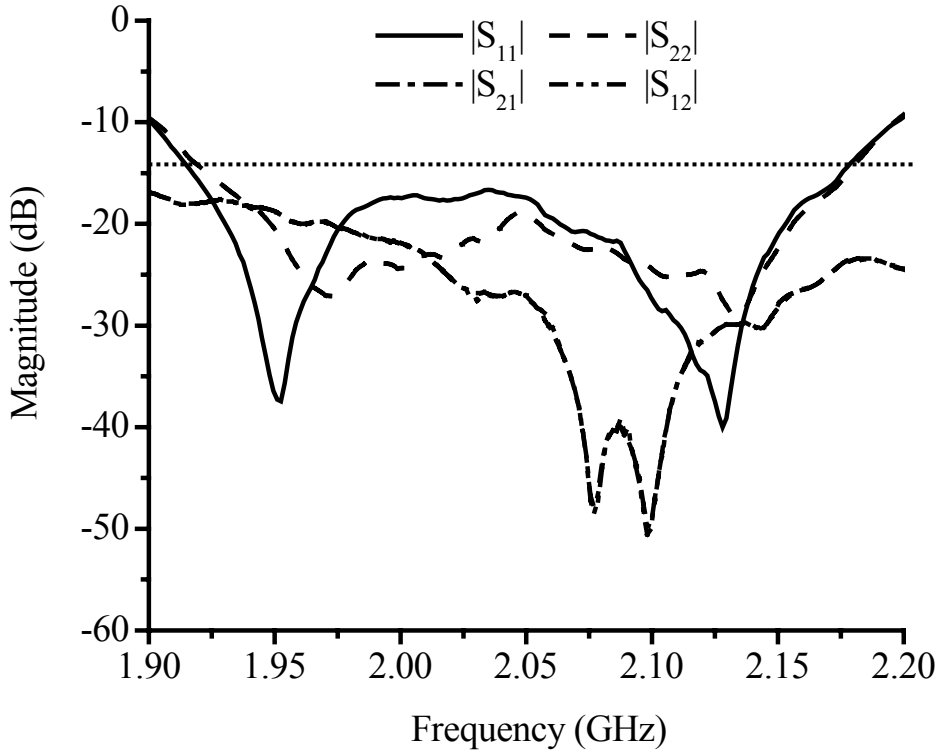

Fig. 4.4.14: Measured S parameters

4.4.4 Radiation Performance

With the patches positioned in a ±45° configuration, the radiation patterns were measured at 1.92GHz, 2.05GHz, and 2.17GHz, which correspond to the lower, center, and upper frequency of the bandwidth, respectively. Figs. 4.4.15 – 4.4.17 display the simulated and measured responses in the *x-z* plane for the vertical and horizontal polarizations, and Figs. 4.4.18 – 4.4.20 display the simulated and measured responses in the *y-z* plane for the vertical and horizontal polarizations. The vertical and horizontal radiation levels were normalized by the total received power.

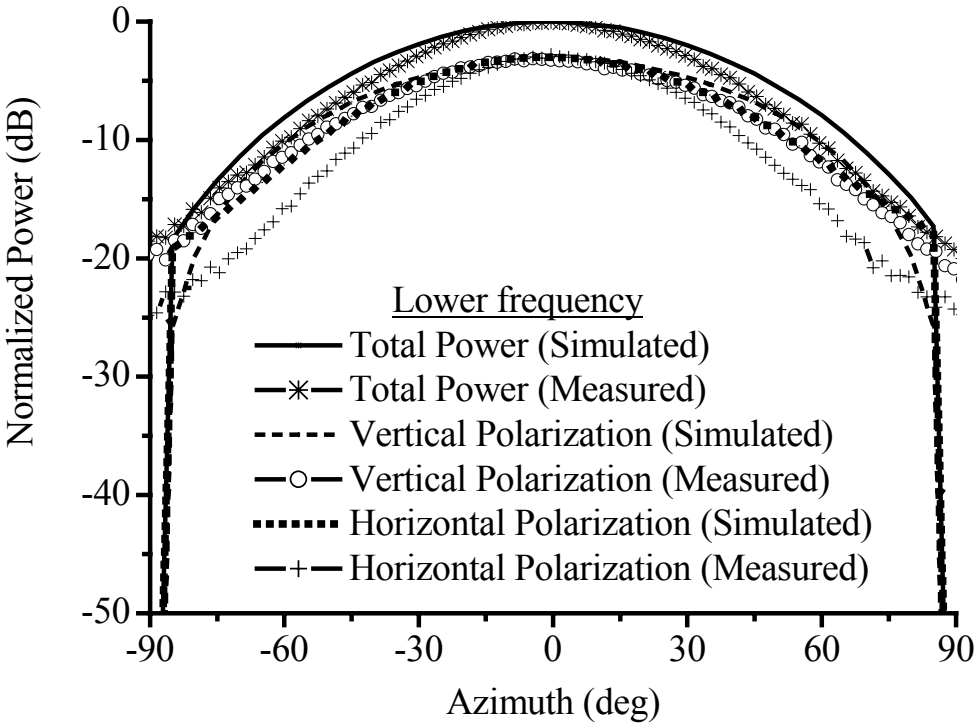

Fig. 4.4.15: Measured and simulated radiation patterns at lower frequency in the *x-z* plane

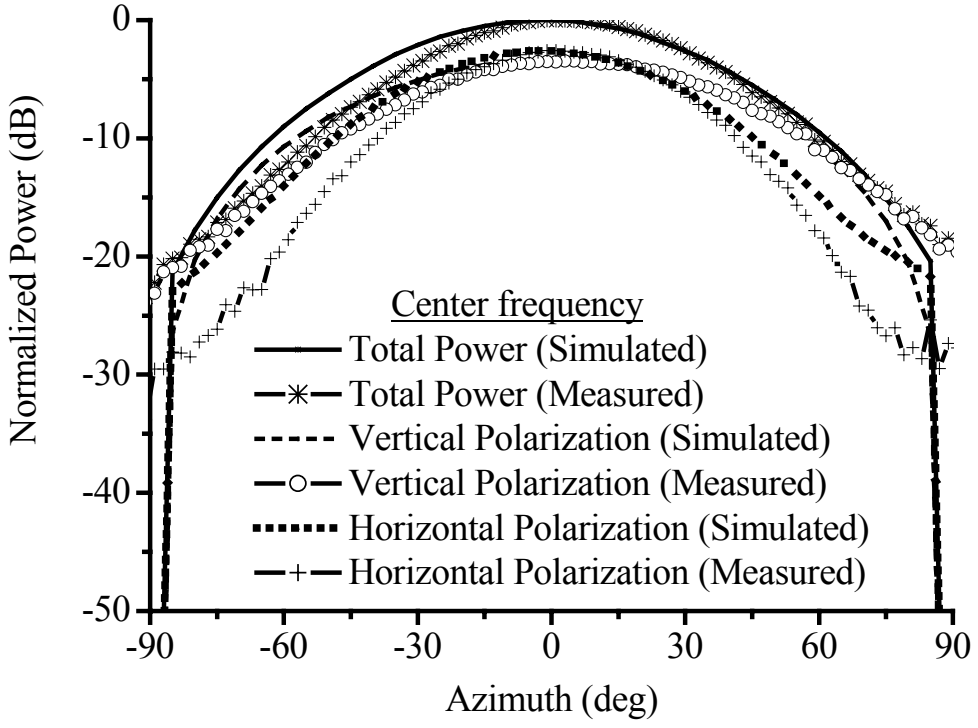

Fig. 4.4.16: Measured and simulated radiation patterns at center frequency in the *x-z* plane

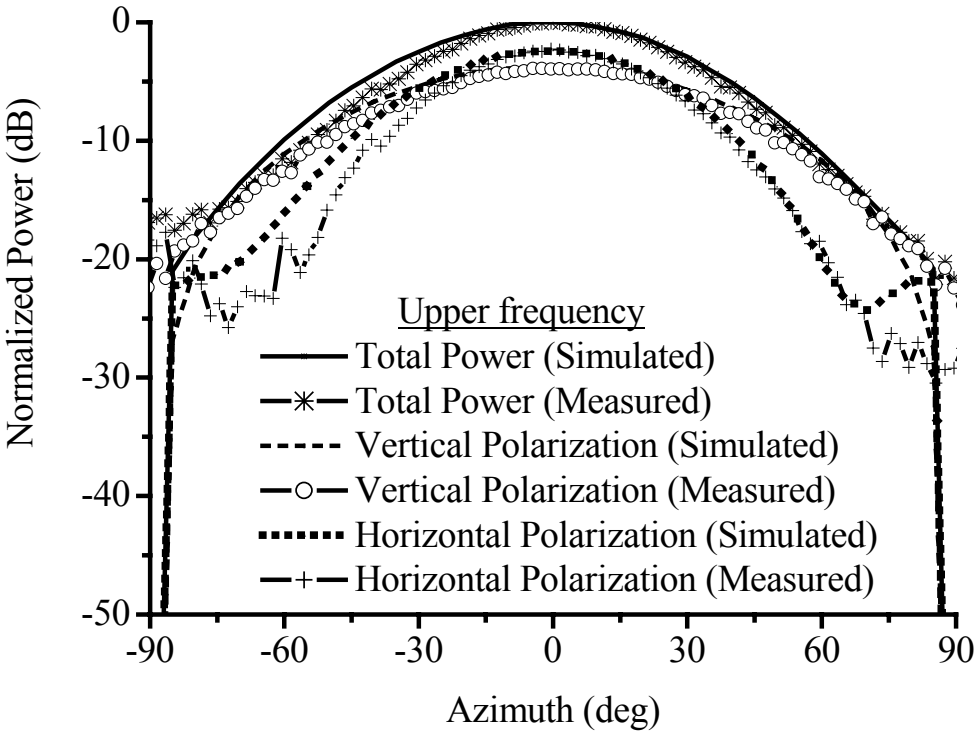

Fig. 4.4.17: Measured and simulated radiation patterns at upper frequency in the *x-z* plane

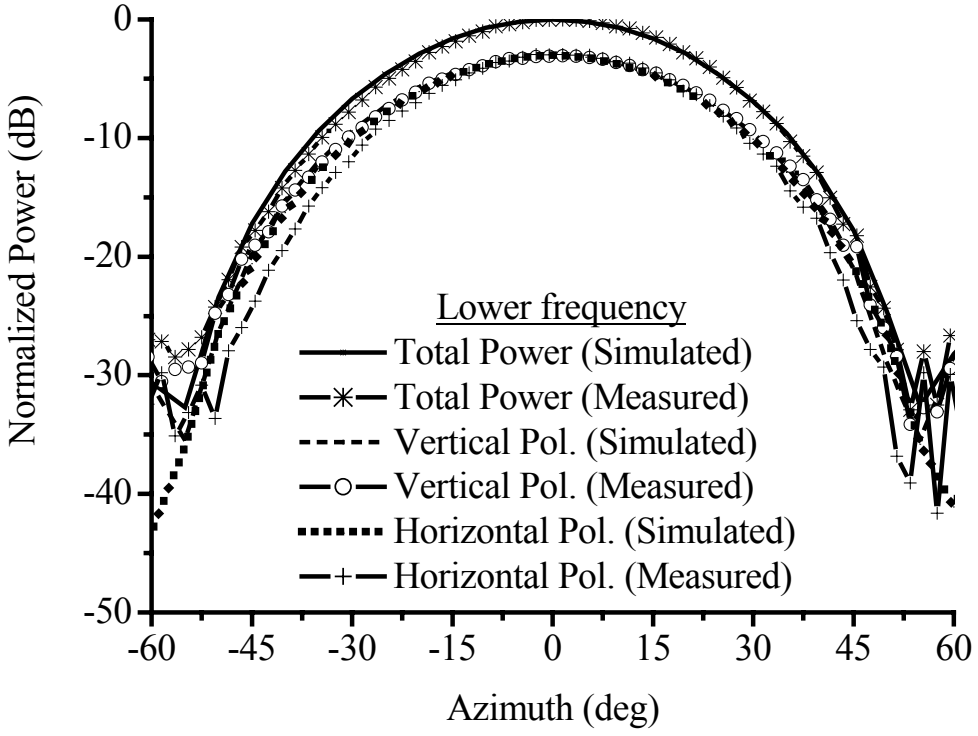

Fig. 4.4.18: Measured and simulated radiation patterns at lower frequency in the *y-z* plane

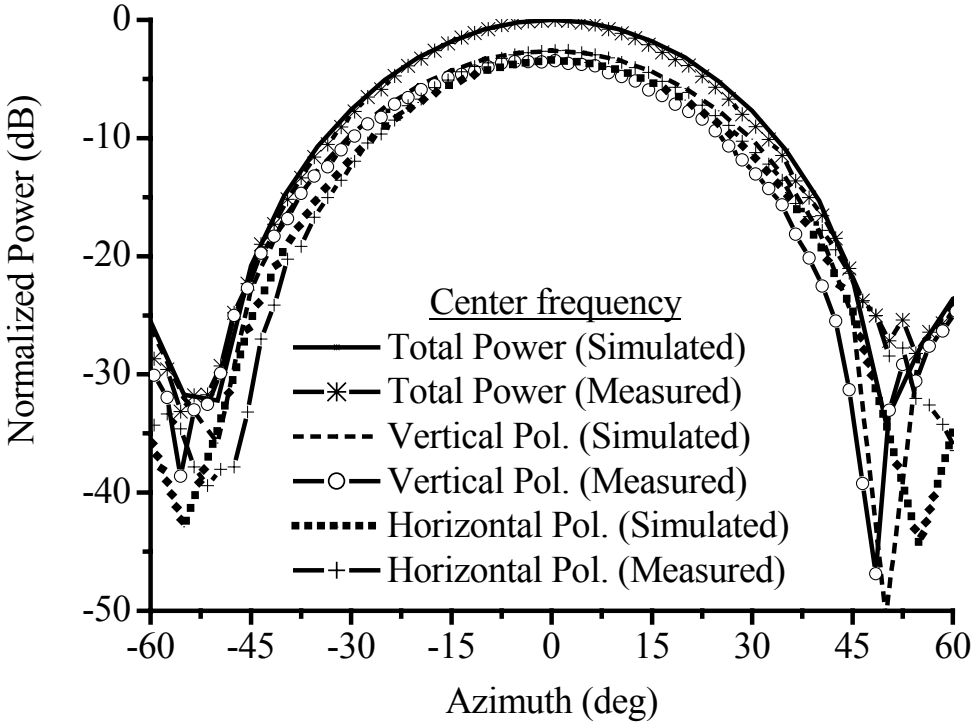

Fig. 4.4.19: Measured and simulated radiation patterns at center frequency in the *y-z* plane

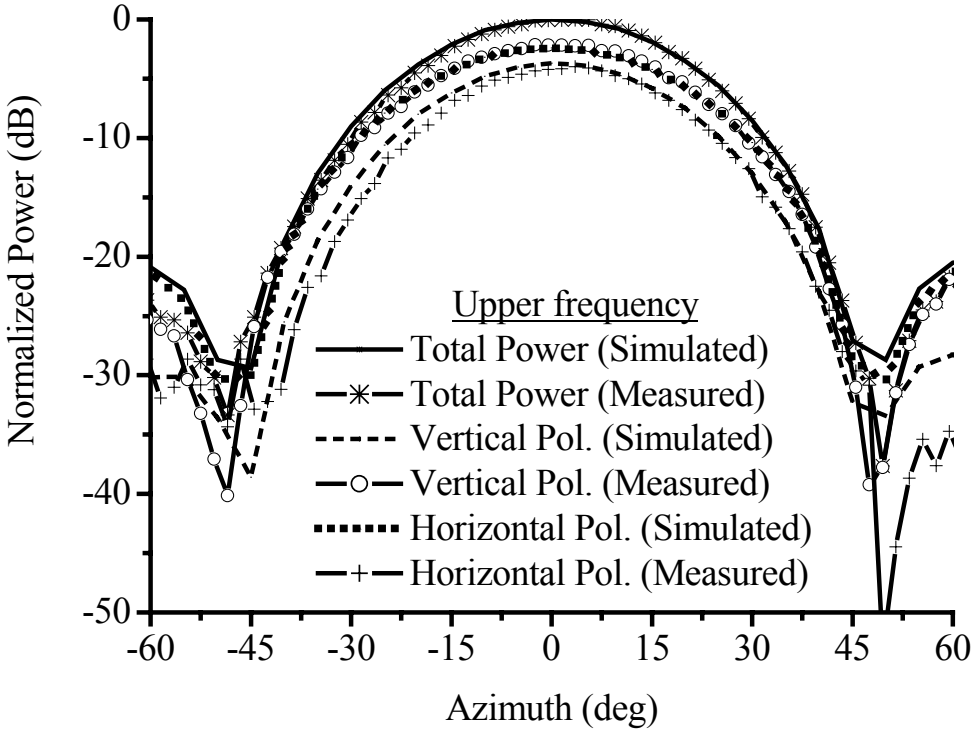

Fig. 4.4.20: Measured and simulated radiation patterns at upper frequency in the *y-z* plane

From the radiation patterns, the half-power beamwidth (HPBW) for the vertical and horizontal polarizations as well as the coverage (defined as the angular range where the difference between the vertical and horizontal polarizations is less than 6dB) are noted and tabulated in Tables 4.4.1 and 4.4.2 for the *x-z* and *y-z* planes, respectively. It can be observed that in the *x-z* plane, the beamwidth for the vertical polarization (VP) is generally wider than that for the horizontal (HP) polarization at all three frequencies. However, in the *y-z* plane, the beamwidth for the vertical and horizontal polarizations are comparable. The coverage in the *x-z* plane is satisfactory and covers the forward 120° sector well at all three frequencies. In the *y-z* plane, the measured coverage is still above 80°.

Table 4.4.1: Measured and simulated HPBW and coverage in the *x-z* plane

	Lower frequency		Center frequency		Upper frequency	
	Simulated	Measured	Simulated	Measured	Simulated	Measured
HPBW (VP)	80°	69°	79°	72°	77°	70°
HPBW (HP)	69°	55°	59°	52°	55°	47°
Coverage	168°	180°	170°	118°	170°	120°

Table 4.4.2: Measured and simulated HPBW and coverage in the *y-z* plane

	Lower frequency		Center frequency		Upper frequency	
	Simulated	Measured	Simulated	Measured	Simulated	Measured
HPBW (VP)	41°	41°	40°	38°	34°	37°
HPBW (HP)	40°	37°	37°	35°	38°	33°
Coverage	110°	125°	95°	84°	95°	81°

The degradation in the measured coverage can be due to the finite ground plane used in the measurements. By increasing the size of the ground plane, it is possible to achieve better coverage as predicted from simulations.

4.4.5 Diversity Performance

Figs. 4.4.21 – 4.4.26 show the calculated far-field coupling σ at the three frequencies using the simulated and measured antenna patterns in the *x-z* and *y-z* planes. The angular range where the far-field coupling is less than 0.7 is tabulated in Table 4.4.3 for the *x-z* and *y-z* planes, respectively. The simulated responses show a better coverage than the measured responses which could be attributed to the deviation of the vertical polarization from the horizontal polarization patterns at higher angles. The measured responses generally cover the forward 120° sector well across the bandwidth.

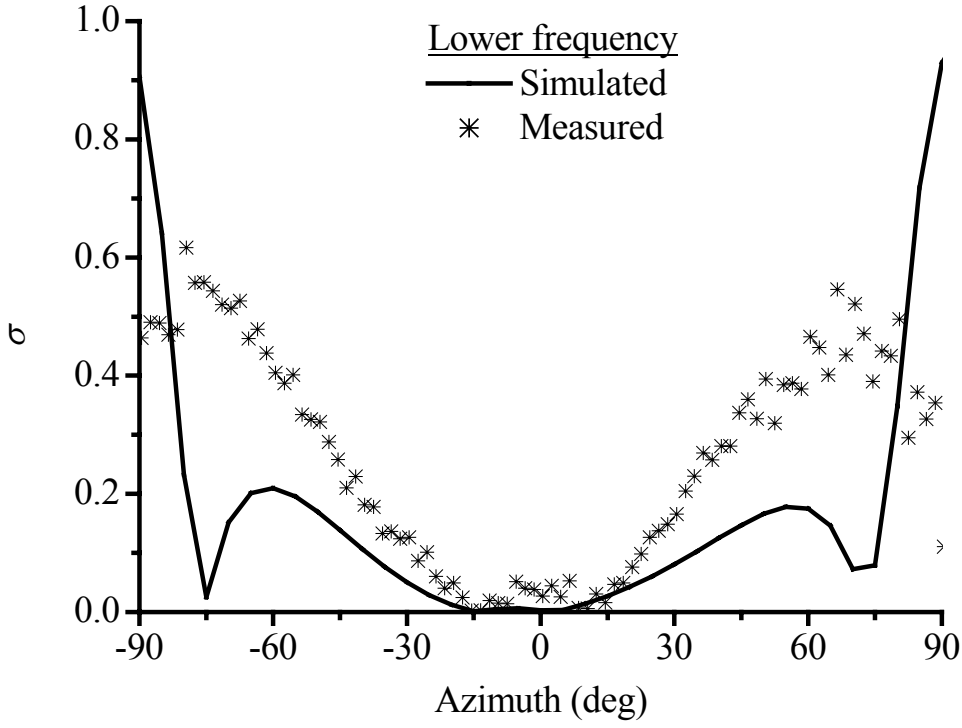

Fig. 4.4.21: Measured and simulated far-field coupling σ at lower frequency in the *x-z* plane

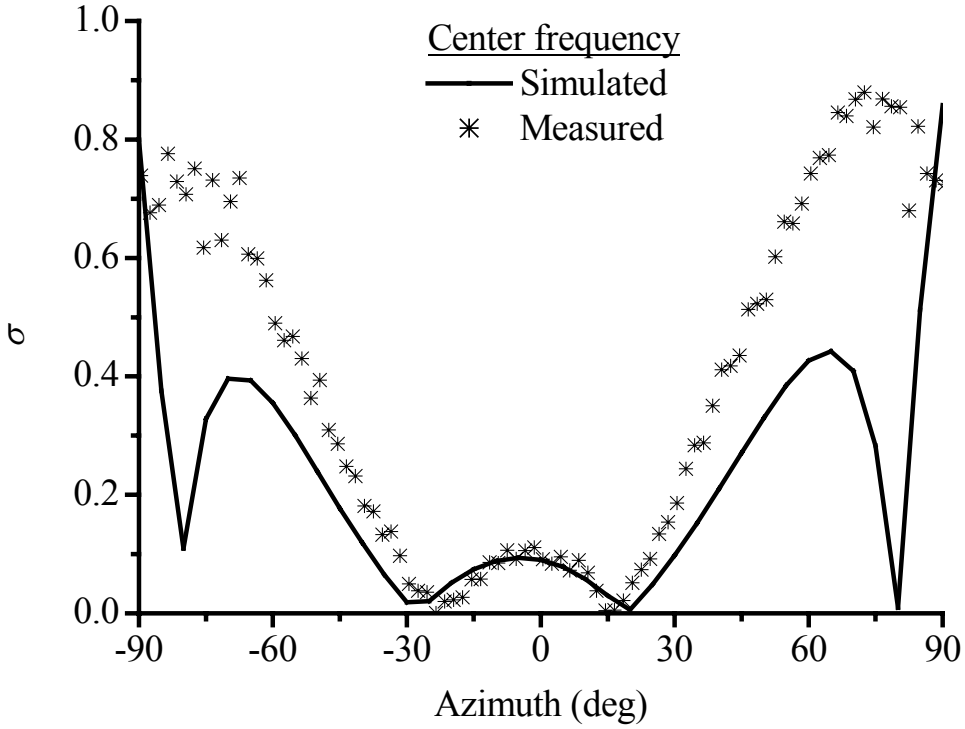

Fig. 4.4.22: Measured and simulated far-field coupling σ at center frequency in the *x-z* plane

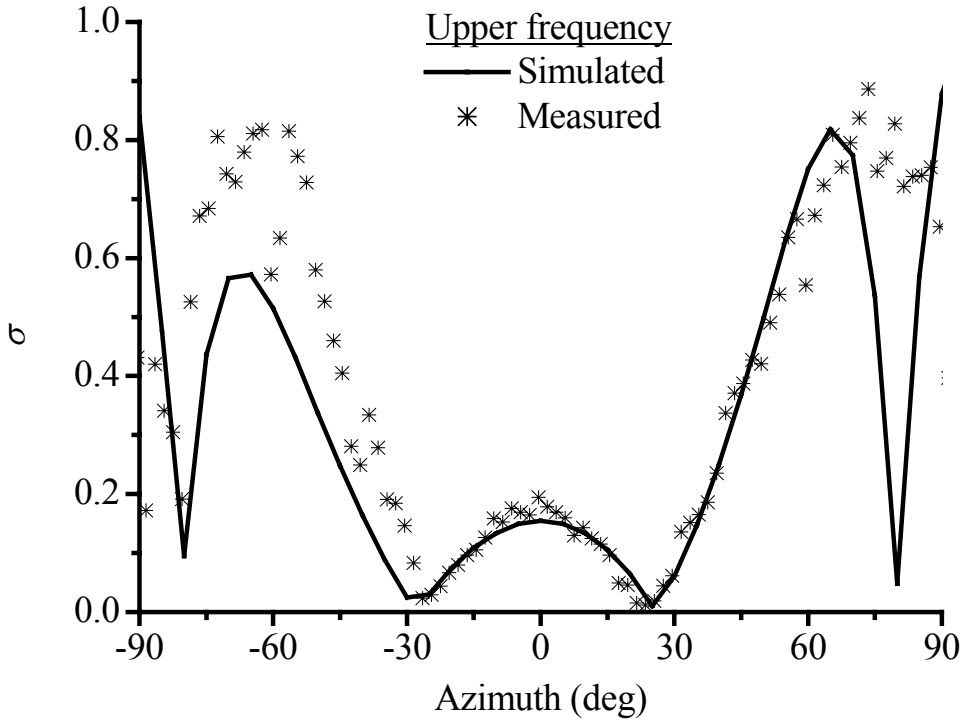

Fig. 4.4.23: Measured and simulated far-field coupling σ at upper frequency in the *x-z* plane

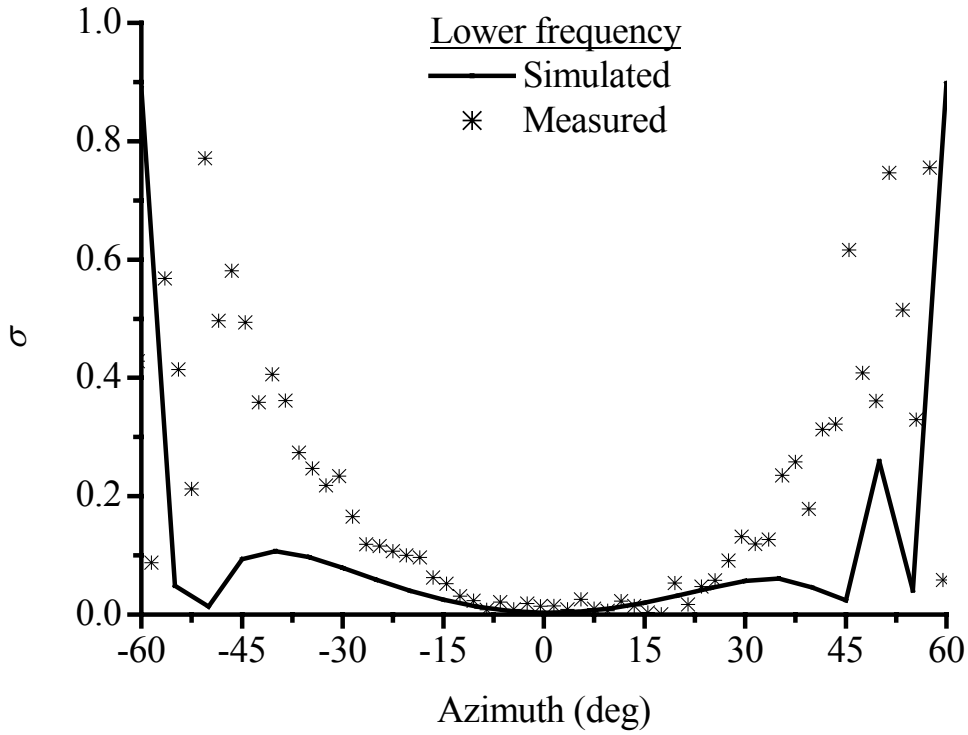

Fig. 4.4.24: Measured and simulated far-field coupling σ at lower frequency in the *y*-*z* plane

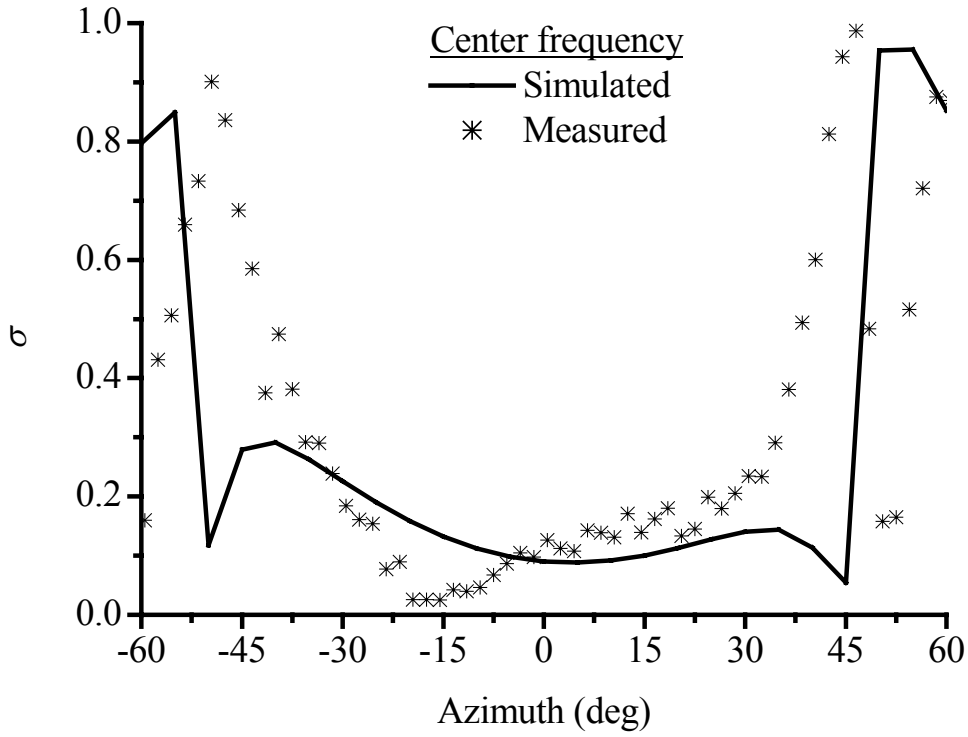

Fig. 4.4.25: Measured and simulated far-field coupling σ at center frequency in the *y*-*z* plane

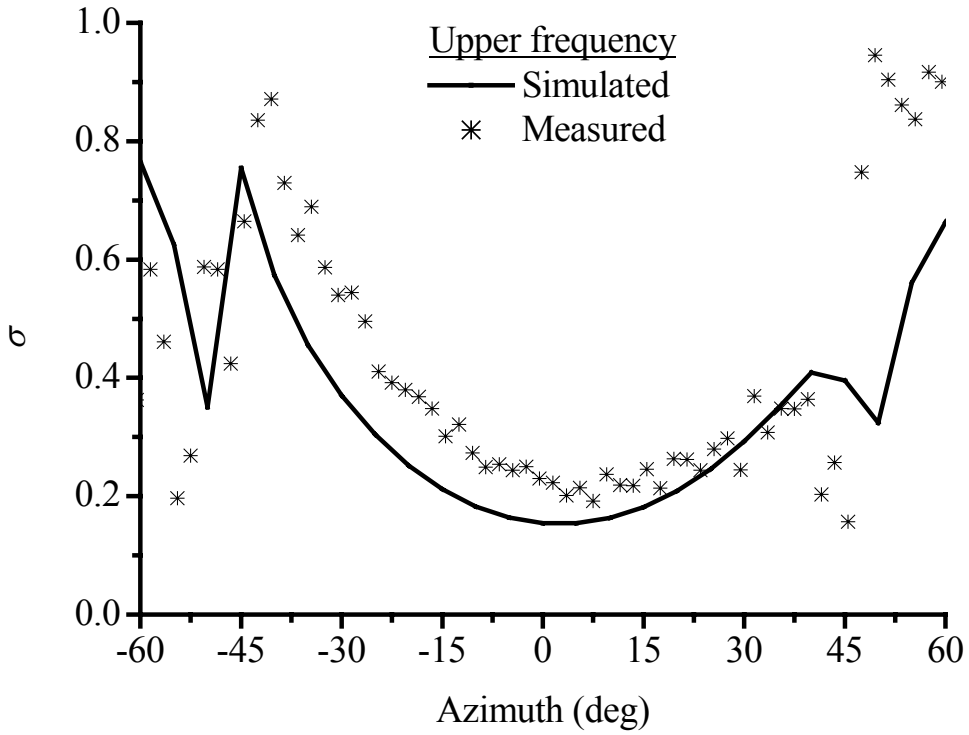

Fig. 4.4.26: Measured and simulated far-field coupling σ at upper frequency in the *y*-*z* plane

Table 4.4.3: Measured and simulated angular coverage for far-field coupling in the *x*-*z* and *y*-*z* planes

	Lower frequency		Center frequency		Upper frequency	
	Simulated	Measured	Simulated	Measured	Simulated	Measured
x-*z* plane	171°	180°	170°	126°	175°	115°
y-*z* plane	110°	101°	108°	88°	106°	85°

Next, the simulated and measured output power correlation as well as the corresponding cross-polar discrimination at each of the three frequencies in a non-fading channel, are calculated and shown in Figs. 4.4.27 – 4.4.32 for the *x*-*z* and *y*-*z* planes, respectively. The angular range, where the correlation coefficient is less than 0.7, is tabulated in Table 4.4.4 for the *x*-*z* and *y*-*z* planes, respectively.

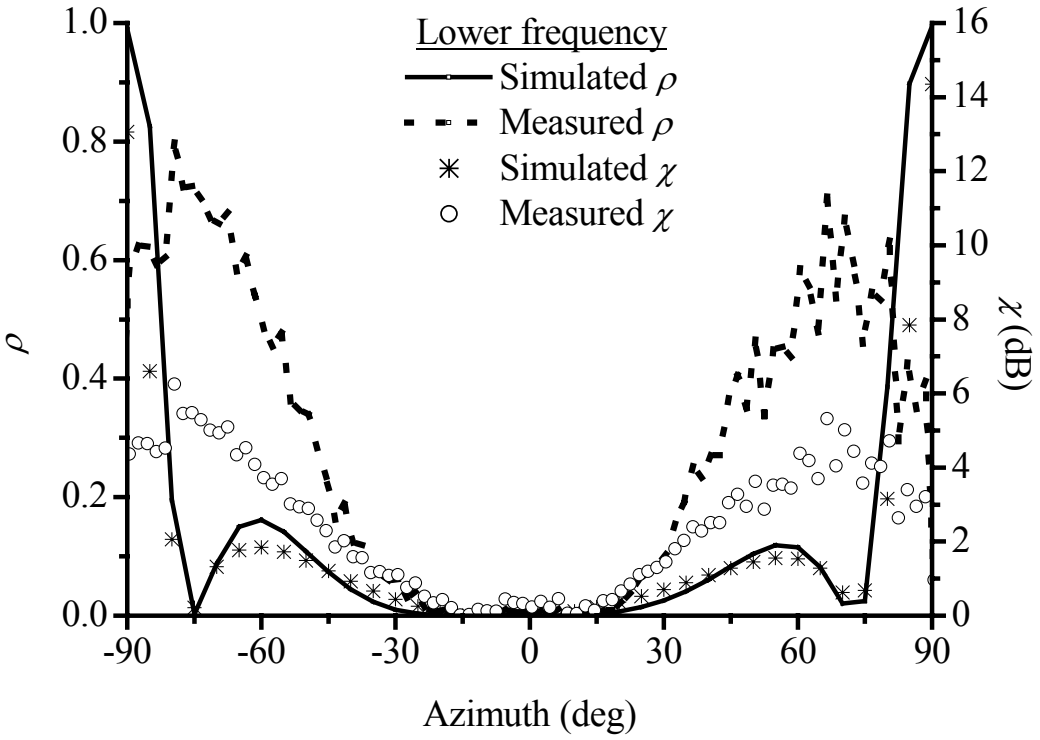

Fig. 4.4.27: Measured and simulated output power correlation coefficient ρ and cross-polar discrimination χ at lower frequency in the *x-z* plane

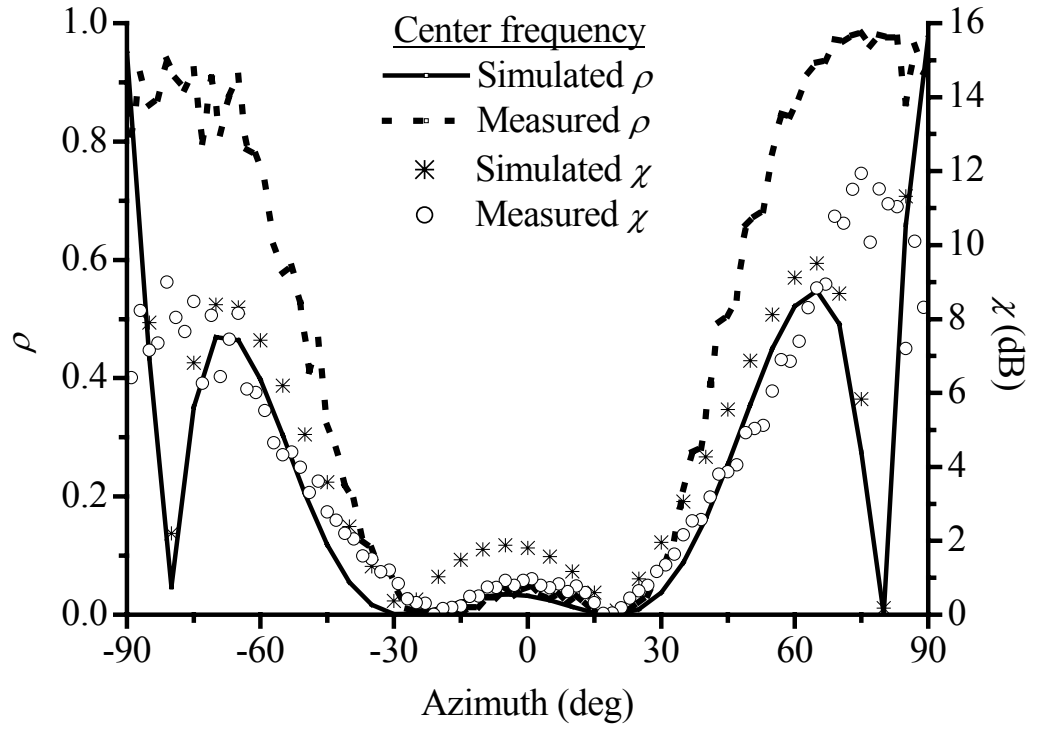

Fig. 4.4.28: Measured and simulated output power correlation coefficient ρ and cross-polar discrimination χ at center frequency in the *x-z* plane

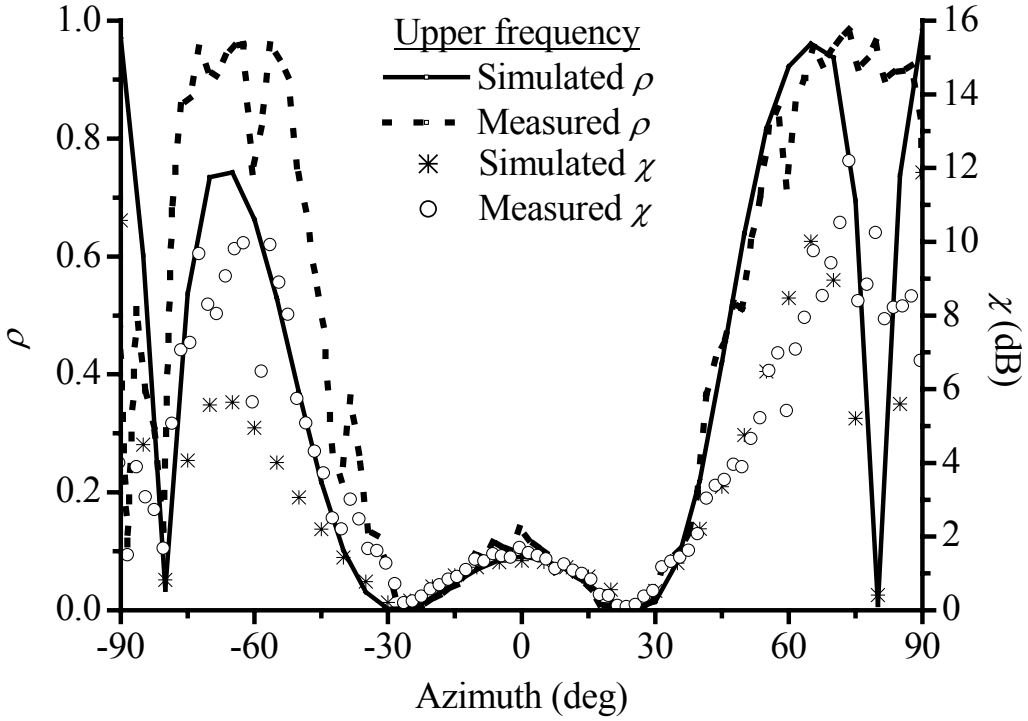

Fig. 4.4.29: Measured and simulated output power correlation coefficient ρ and cross-polar discrimination χ at upper frequency in the *x-z* plane

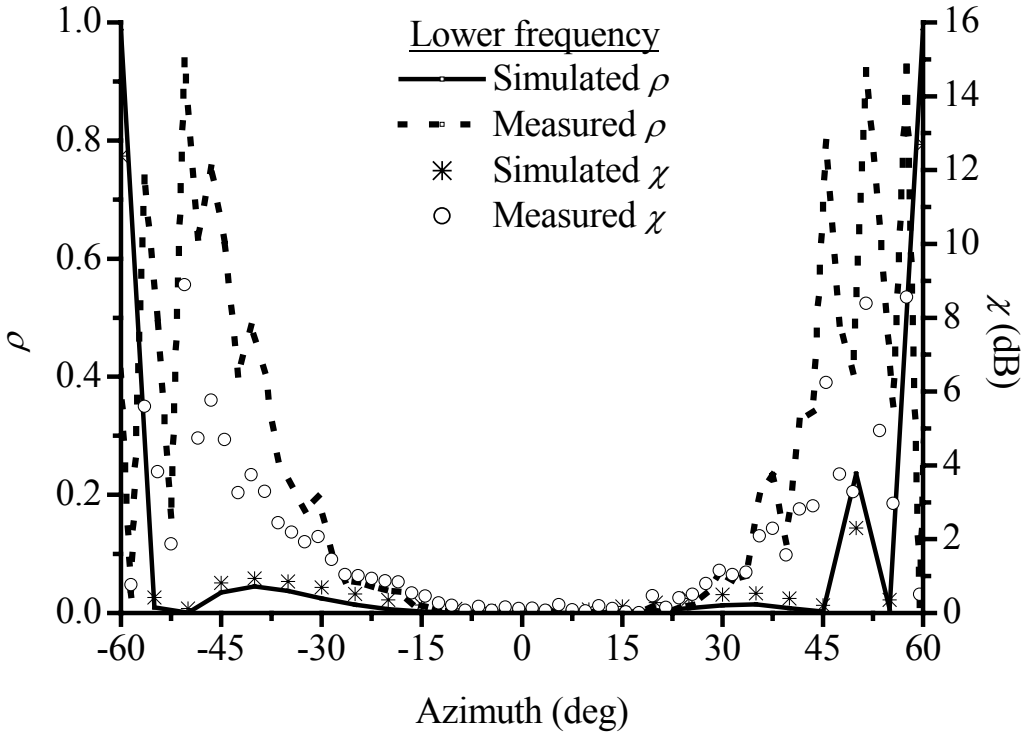

Fig. 4.4.30: Measured and simulated output power correlation coefficient ρ and cross-polar discrimination χ at lower frequency in the *y-z* plane

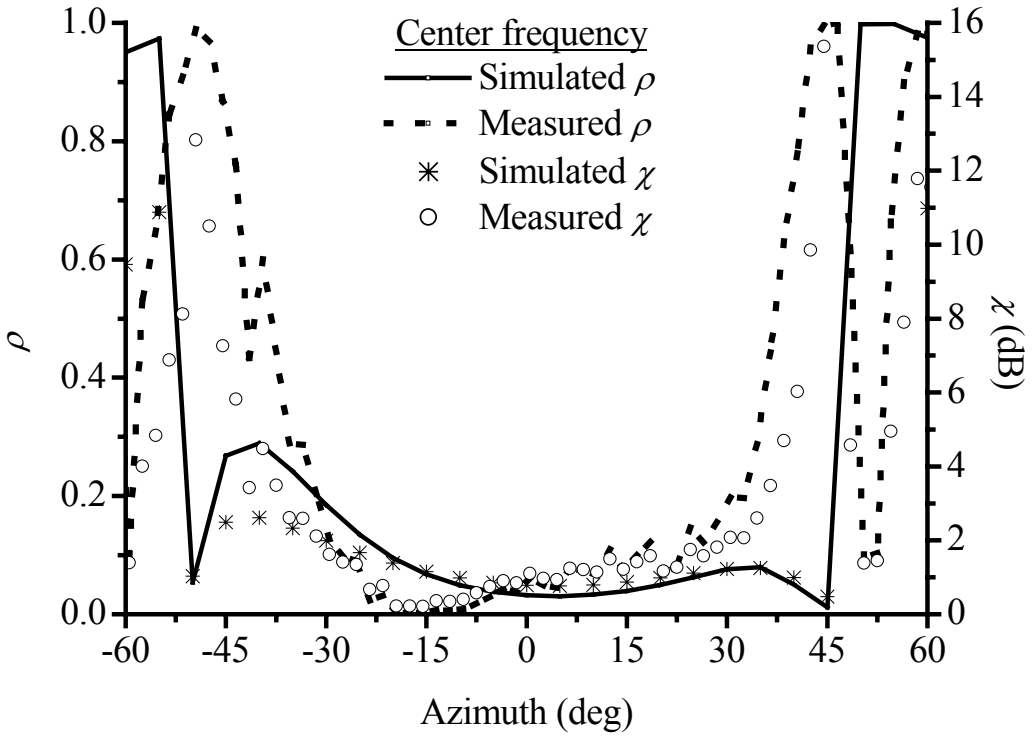

Fig. 4.4.31: Measured and simulated output power correlation coefficient ρ and cross-polar discrimination χ at center frequency in the *y*-*z* plane

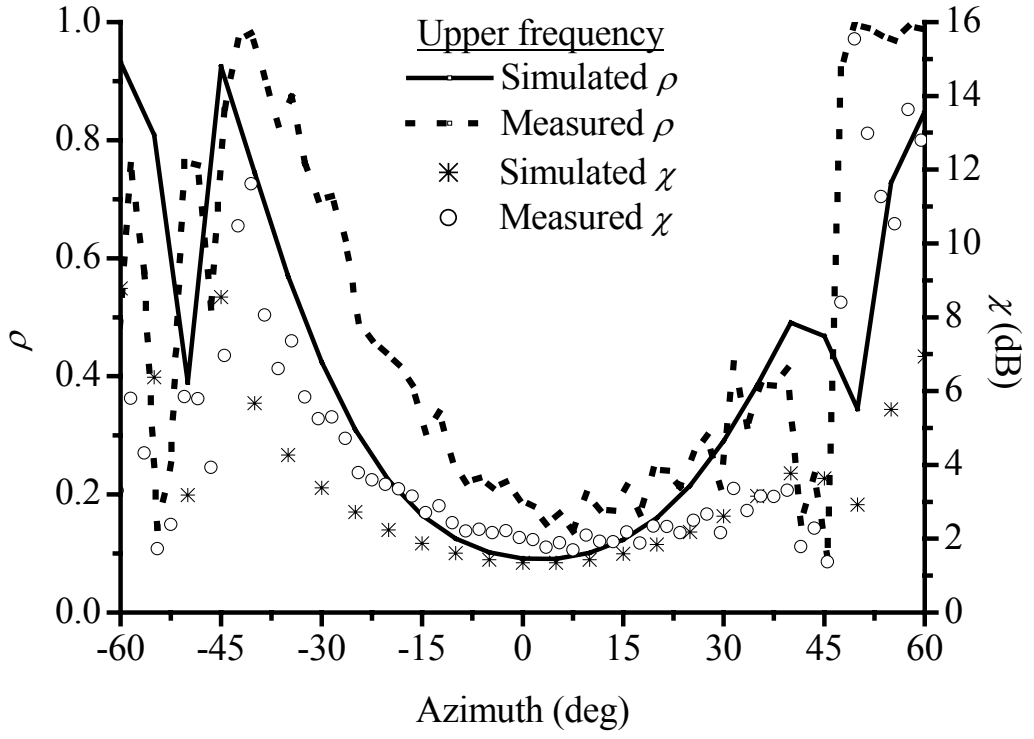

Fig. 4.4.32: Measured and simulated output power correlation coefficientρ and cross-polar discrimination χ at upper frequency in the *y*-*z* plane

Table 4.4.4: Measured and simulated angular coverage for output power correlation in the *x*-*z* and *y*-*z* planes

	Lower frequency		Center frequency		Upper frequency	
	Simulated	Measured	Simulated	Measured	Simulated	Measured
x-*z* plane	167°	164°	173°	111°	171°	103°
y-*z* plane	110°	91°	96°	82°	94°	74°

It can be observed that at the center and upper frequencies, the difference between the simulated and measured results can be attributed to the small ground plane size used in the measurements. Generally, the measured coverage for output power correlation decreases as the frequency increases due to the distortion of the radiation patterns, especially at the higher angles.

Figs. 4.4.33 – 4.4.38 show the simulated and measured diversity gains at the three frequencies in the *x*-*z* and *y*-*z* planes. The coverage, defined as the angular range at 1% outage rate, where the diversity gain is within 3dB of the maximum value, is tabulated in Table 4.4.5 for both the planes. In the *x*-*z* plane, the measured coverage is observed to decrease as the frequency increases. Here, it must be noted that the simulated results are better than the measured results since the ground plane used in the simulations is assumed to be infinite. Hence, the measured coverage can be enhanced further by increasing the size of the ground plane used in the measurement so that the degradation of the radiation patterns, especially at the higher angles will not be severe. The coverage in the *y*-*z* plane is much lower due to the decreased beamwidth arising from the array configuration.

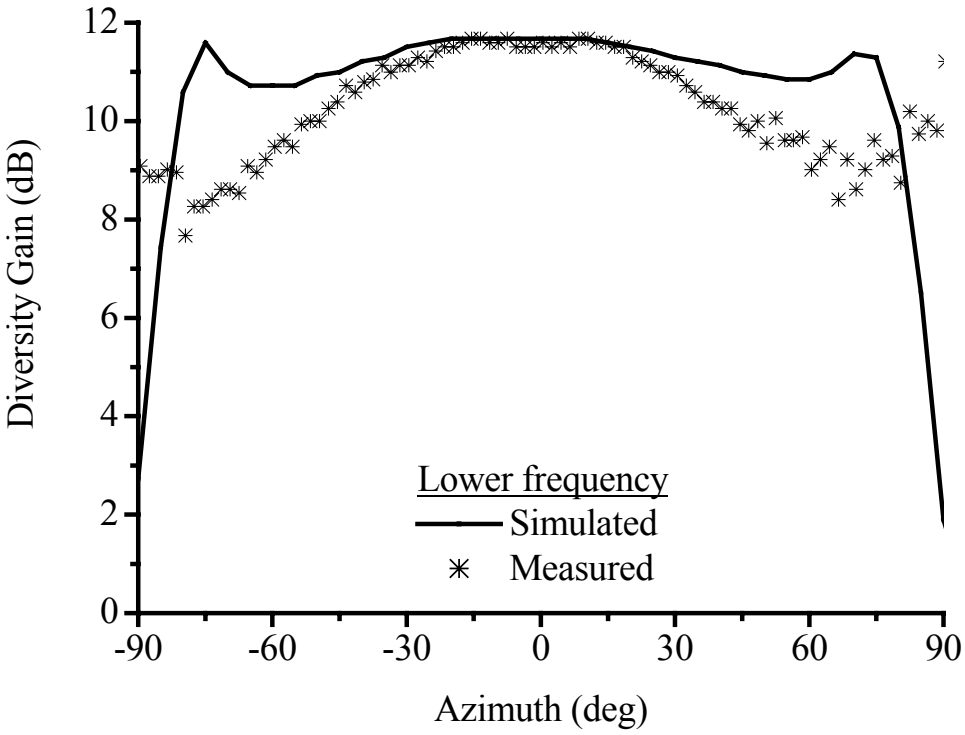

Fig. 4.4.33: Measured and simulated diversity gain at lower frequency in the *x-z* plane

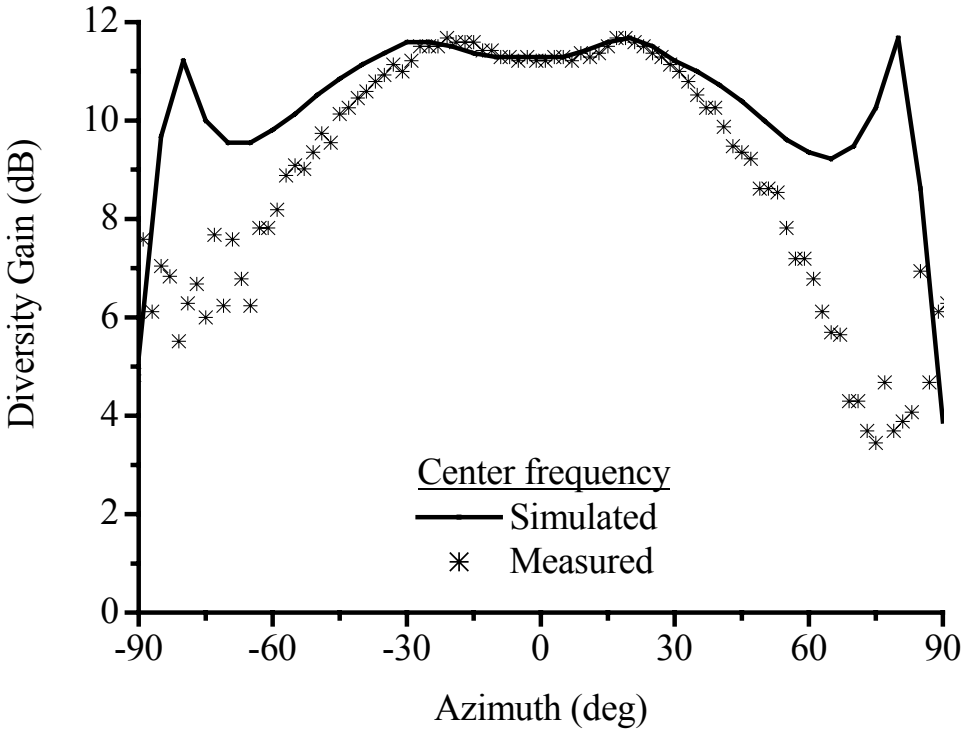

Fig. 4.4.34: Measured and simulated diversity gain at center frequency in the *x-z* plane

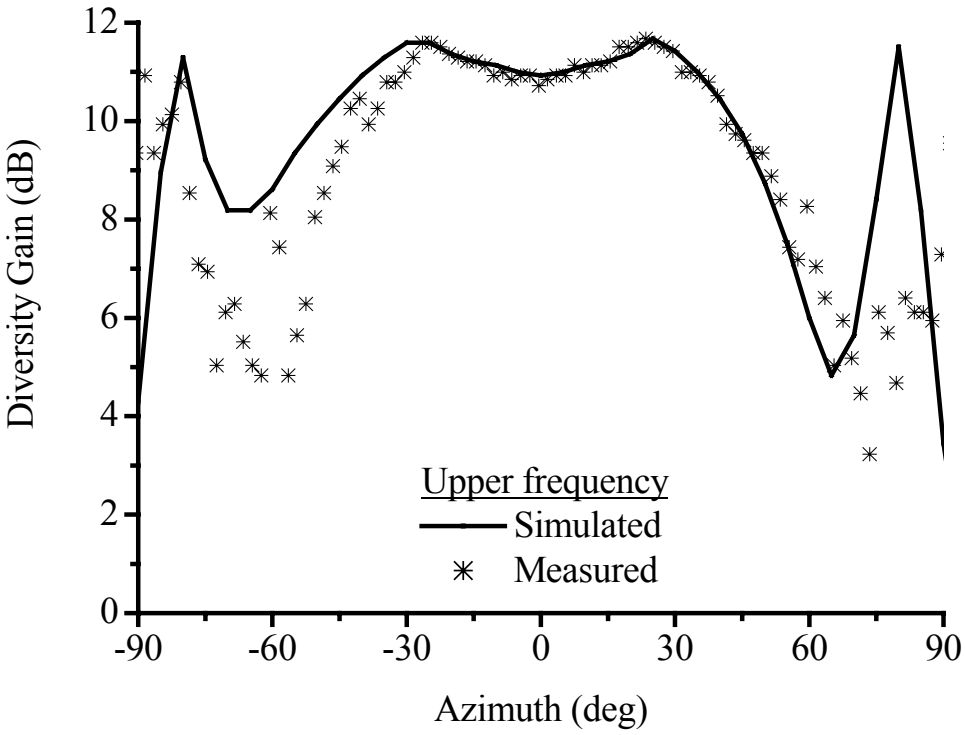

Fig. 4.4.35: Measured and simulated diversity gain at upper frequency in the *x-z* plane

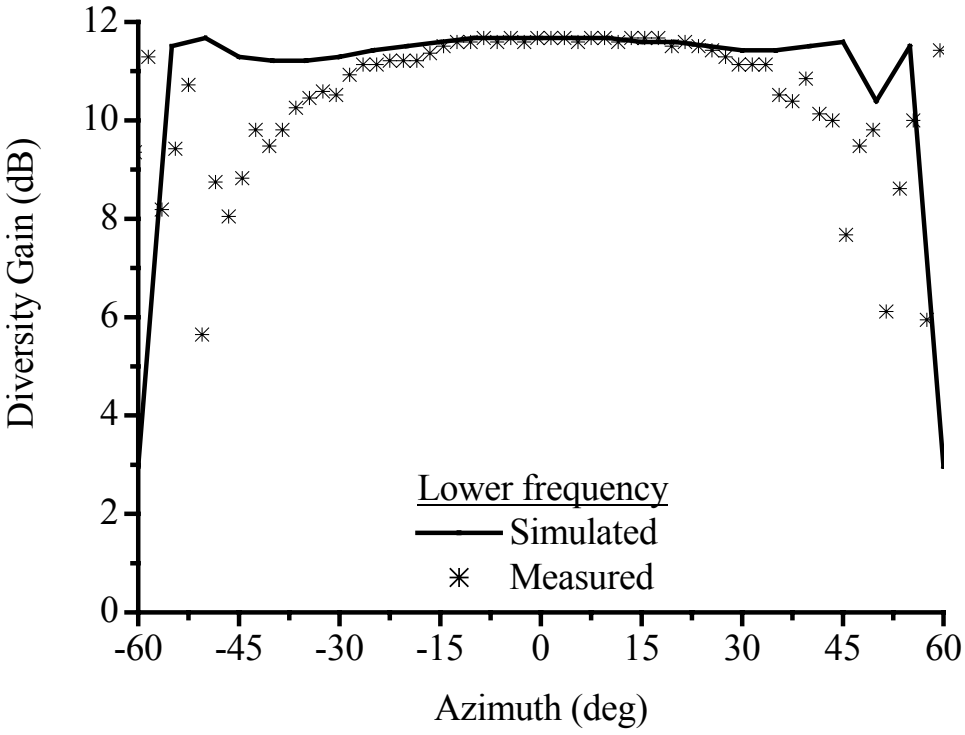

Fig. 4.4.36: Measured and simulated diversity gain at lower frequency in the *y-z* plane

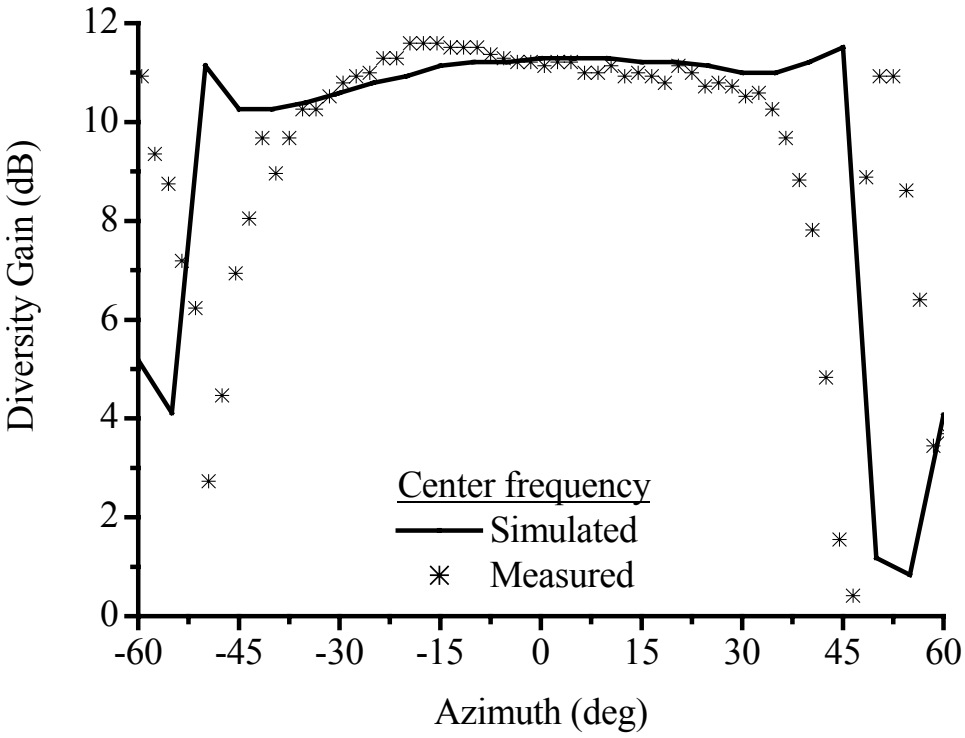

Fig. 4.4.37: Measured and simulated diversity gain at center frequency in the *y-z* plane

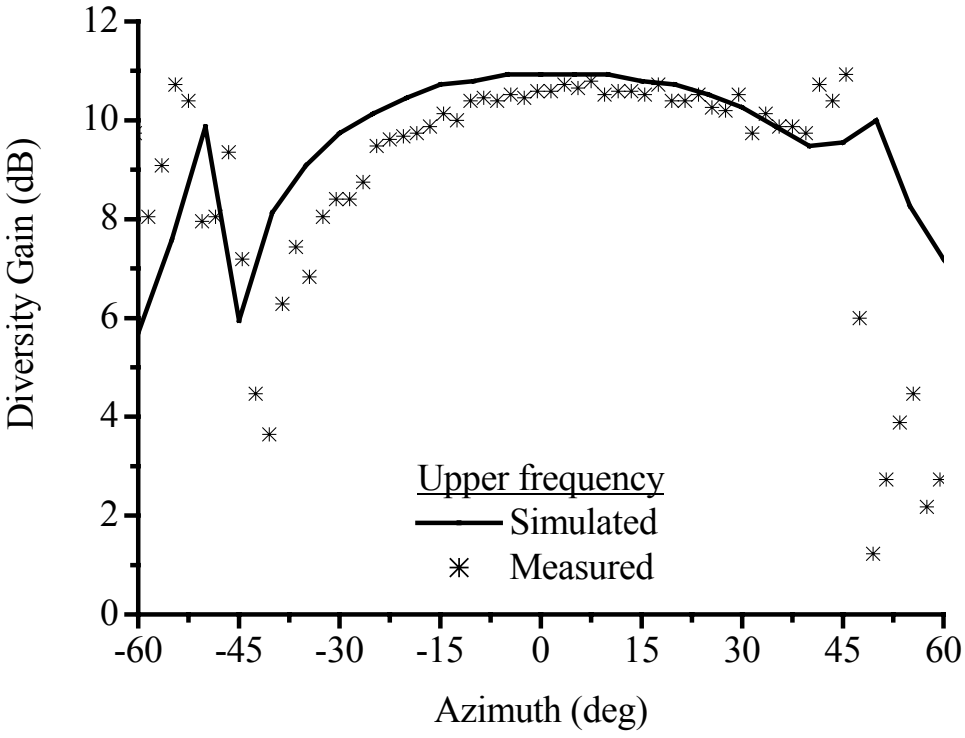

Fig. 4.4.38: Measured and simulated diversity gain at upper frequency in the *y-z* plane

Table 4.4.5: Measured and simulated angular coverage for diversity gain in the *x-z* and *y-z* planes

	Lower frequency		Center frequency		Upper frequency	
	Simulated	Measured	Simulated	Measured	Simulated	Measured
x-z plane	169°	152°	169°	113°	135°	107°
y-z plane	110°	95°	95°	81°	117°	82°

4.5 Conclusions

In this Chapter, the designs of a stacked polarization diversity element and array are presented. Besides analyzing the antenna in terms of the impedance and radiation performances, the diversity performance is also assessed in terms of the far-field coupling, output power correlation, and diversity gain. A significant issue to note is that besides the channel characteristics, the polarization characteristics of the antenna also have a considerable effect on cross-polar discrimination. In order to investigate the effects of antenna design on the diversity performance, the analysis assumes a non-fading channel.

According to the measured results, the impedance bandwidth of the array is 12.2% for the $|S_{11}| \leq$ -14dB, covering the entire PCS1900 band well. In addition, the measured radiation performances of the array in the *x-z* plane show a 6dB coverage of at least 118° across the lower, center, and upper frequencies of the bandwidth. The diversity performance has been found to deteriorate at the upper frequency, which can be attributed to the deviation between the vertical and horizontal radiation patterns, especially at the higher angles. The maximum diversity gain at 1% outage rate is

11.7dB and is observed to decrease by 25% when the correlation coefficient is 0.7. As the requirement of the system becomes more stringent (lower outage rate), the maximum achievable diversity gain increases correspondingly. The maximum gain at an outage rate of 20% is reduced to half when the outage rate is 1%.

Chapter 5

DIVERSITY PERFORMANCE OF GAP-COUPLED PATCH ANTENNAS

5.1 Introduction

A common drawback of patch antennas is their narrow bandwidth, typically ranging up to a few percent depending on the dielectric constant of the substrate, the dielectric thickness, and the geometry of the patch. A number of bandwidth enhancement techniques have been reported in the literature. Multi-resonance techniques which involve the use of stacked or parasitic elements have been used to enhance the bandwidth.

In Chapter 4, the use of stacked patches is capable of increasing the bandwidth since the resonant frequencies of the top and bottom patches are slightly offset. Other techniques include the trapezoidal-shaped antenna design [Kum81], having parasitic strips capacitively coupled to the non-radiating edges of the main radiating patch [Sch79][Aan86], etching slots on the patch [Ton97], log-periodic, and quasi-log-periodic structures [Hal80][Pue81a], etc.

The use of gap-coupling technique to improve the bandwidth performance has also been widely discussed. The main patch can be gap-coupled on its radiating or non-radiating edges [Kum84][Kum85][Aan90]. In this method, resonators of slightly

different lengths are coupled together by capacitive gap coupling. The broad bandwidth is achieved by the staggering of resonant frequencies of the resonators.

The gap-coupled patch antenna design has been analyzed by using the Green's function approach and the segmentation method [Oko76][Gup81], where the antenna geometry is segmented into shapes for which the Green's functions are known. The scattering matrices of the individual components are then combined to obtain the overall *S*-matrix. However, due to the long computation time for the *S*-matrix for each segment, an alternative method is proposed in which the *Z*-matrix of the individual components are combined to give the overall *Z*-matrix from which the overall *S*-matrix can be determined [Cha81].

The *Z*-matrix of the multiport network shown in Fig. 5.1.1 can be obtained with the knowledge of the Green's function. From the figure, the outer periphery of the antenna is divided into sections of small widths to account for the open edge fringing field capacitance. The field variation across the width of each of these small sections (ports) is negligibly small. Each port is terminated with a conductance to account for the radiated power [Pue81b]. The coupling gap can be modeled as a two-dimensional capacitive π-network, in which the series capacitance is shunted by a conductance to account for the radiation from the gap. The *Z*-matrices of the radiation conductance networks and the capacitive π-networks can be evaluated from their respective network models.

With the knowledge of the *Z*-matrices from the various segments, the input impedance and the voltage around the periphery of the antenna can be evaluated. With the voltages calculated using the segmentation method, the equivalent magnetic current

distribution around the periphery of the antenna can be calculated which could be used to evaluate the far-field radiation performance [Sha83].

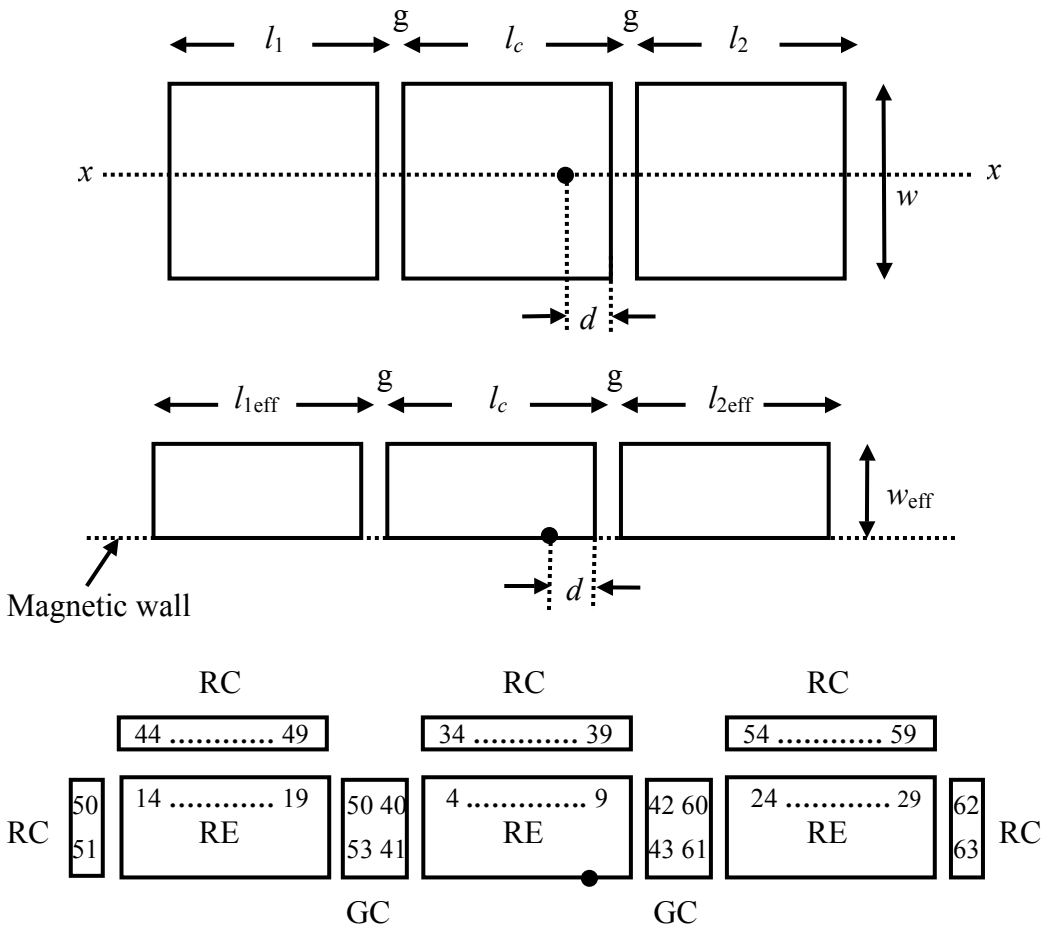

RC: Radiation conductance network
GC: Gap circuit
RE: Rectangular element

Fig. 5.1.1: (a) Parasitic elements gap-coupled to radiating edges of the patch antenna (b) Even mode half section with respect to axis *xx* (c) Segmented network

5.2 Dual-linear Polarization Gap-coupled Antenna

In order to achieve the desired bandwidth, the technique of gap coupling can be extended to dual-linear polarization antenna design. In this Chapter, the parametric study is conducted in Section 5.2.2 with the help of the Zeland IE3D simulator. The impedance, radiation, as well as the diversity performance of a dual-linear polarized gap-coupled antenna configuration is analyzed and compared in Sections 5.2.3 – 5.2.5.

5.2.1 Geometry

As shown in Fig. 5.2.1, the design consists of a main patch ($l_c \times l_c$) and four parasitic patches ($l_s \times w_s$) gap-coupled to the main patch. For dual-linear polarization, the sides of the main patch are of the same length. The parasitic patches whose sides are parallel and orthogonal to the main patch are denoted by w_s and l_s, respectively. The patches are etched on a 1.58mm-thick substrate (Duroid 5880, $\varepsilon_r = 2.2$). The parasitic patches are separated from the main patch by a gap width of g. Two adjacent 50Ω co-axial probes of radius 0.6mm excite the main patch at d from its sides. In order to excite the resonances within the 2.4GHz ISM band, the dimensions for the main and the parasitic patches are properly selected.

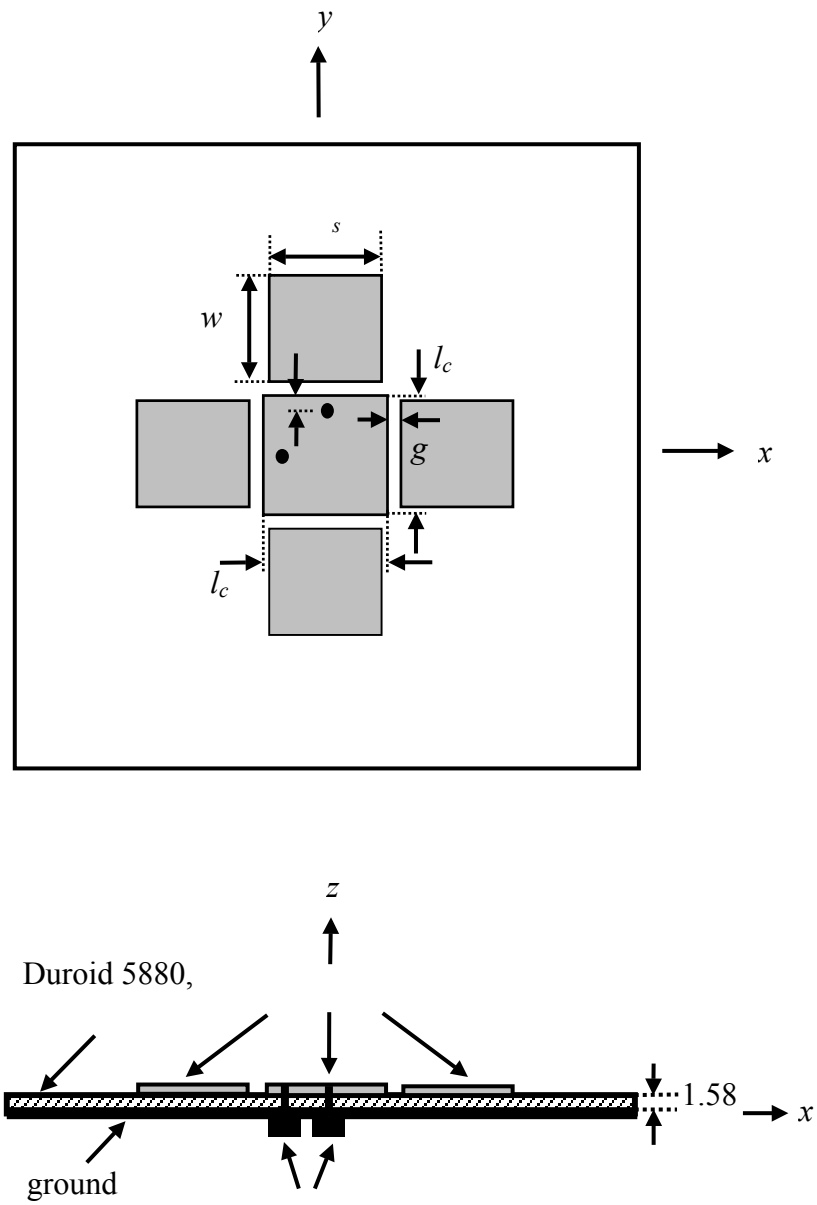

Fig. 5.2.1: Geometry of a gap-coupled antenna

5.2.2 Parametric Study

In this section, a parametric study will be conducted to investigate the influence of physical parameters such as the size of main and parasitic patches, gap width, and location of feed point on the impedance matching. This is done so as to obtain an optimized configuration.

(a) Effects of varying the size of main patch

The size of the main patch l_c was varied from 39mm to 40mm with $w_s = l_c$, l_s = 38.5mm, d = 0.5mm, and g = 0.75mm. According to Fig. 5.2.2, varying l_c generally has a significant effect on the resonant frequency. An increase in l_c generally lowers the resonant frequency. Besides, the matching is also sensitive to the size of the main patch as can be predicted from the impedance loci. With an increase in l_c, the size of the loop increases moves in an anticlockwise manner. When l_c = 39.5mm, the loop is observed to rotate to the center and the points on the locus corresponding to the higher frequency are more concentrated at the center of the Smith chart, thus able to provide a broader bandwidth as compared to the case when l_c = 40mm. In addition, the locus around the lower frequency is observed to move towards the center of the Smith chart as l_c increases.

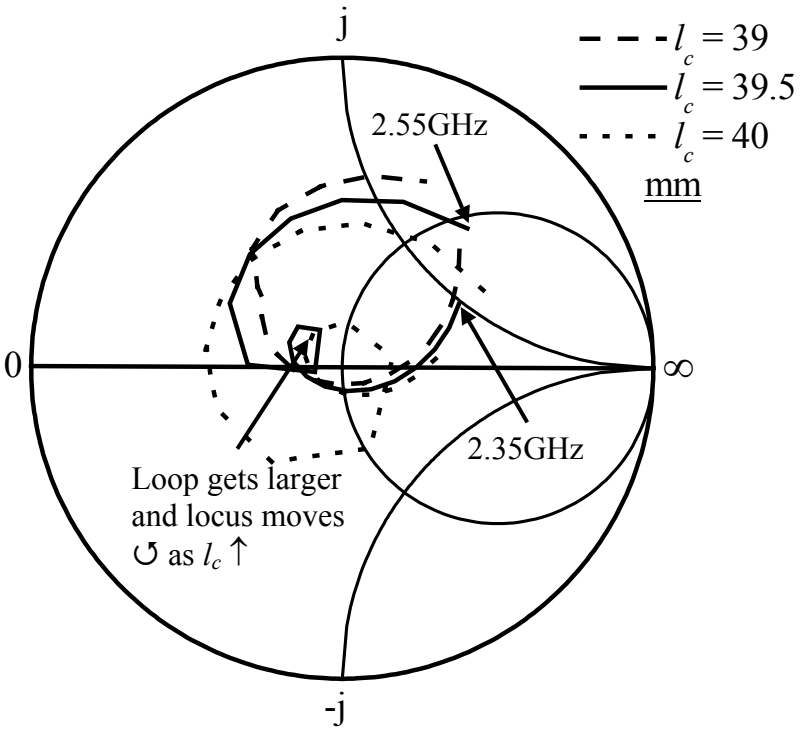

Fig. 5.2.2: Simulated impedance loci for varying length l_c of main patch

(b) Effects of varying the length of parasitic patch

As illustrated in Fig. 5.2.3, the length of the parasitic patch l_s was varied from 37.5mm to 39.5mm with $w_s = l_c = 39.5$mm, $d = 0.5$mm, and $g = 0.75$mm. As l_s increases, the loop size decreases and eventually disappears when $l_s = 39.5$mm. Since the impedance locus turns in a clockwise manner as l_s increases, the matching at the lower frequency improves but begins to degrade at the higher frequency.

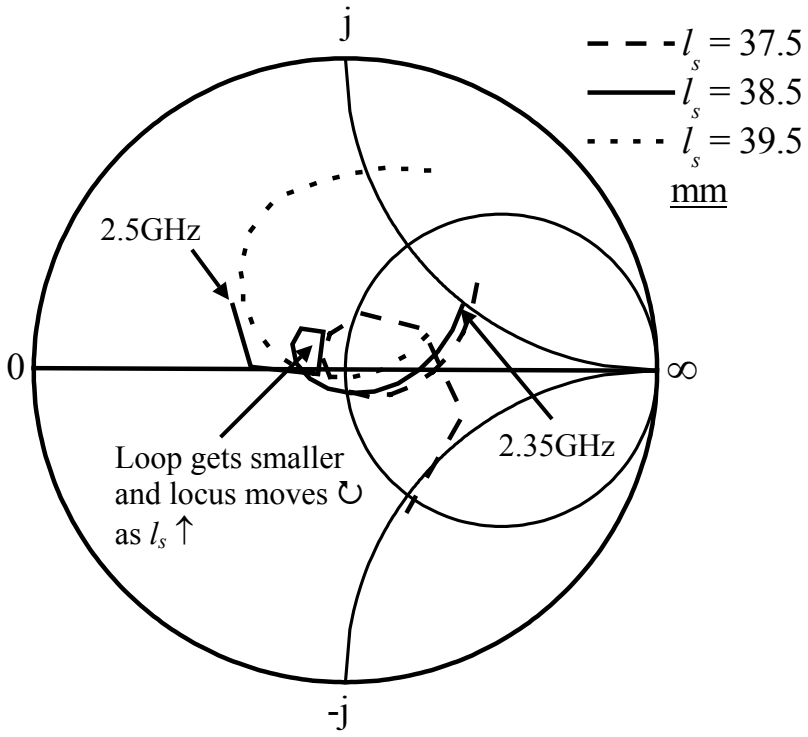

Fig. 5.2.3: Simulated impedance loci for varying length l_s of parasitic patch

(c) Effects of varying the width of parasitic patch

The width of the parasitic patch w_s was varied from 38.5mm to 40.5mm with l_s = 38.5mm, l_c = 39.5mm, d = 0.5mm, and g = 0.75mm. According to Fig. 5.2.4, varying w_s generally has a significant effect on the resonant frequency. It can be observed that the size of the loop is very responsive to the changes in w_s. As w_s increases, the loop size increases and moves outwards in a clockwise manner. The loop is formed at the location corresponding to the lower frequency on the impedance locus. Also, the length of the impedance locus increases, which indicates that the frequency points are less concentrated as the width of the parasitic patch increases.

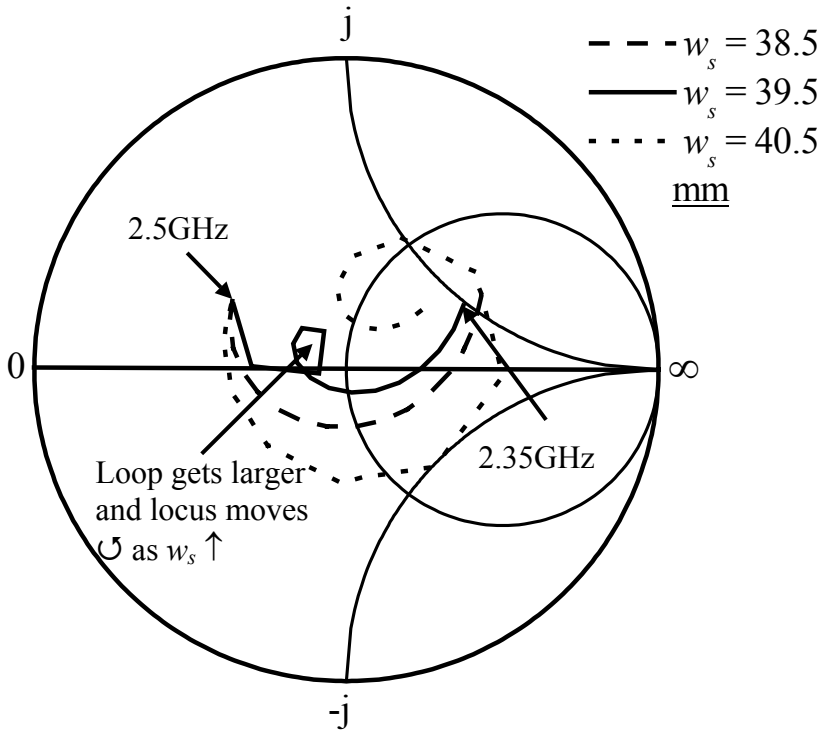

Fig. 5.2.4: Simulated impedance loci for varying width w_s of parasitic patch

(d) Effects of varying the gap width

The gap width g was varied from 0.5mm to 1mm with $w_s = l_c = 39.5$mm, $l_s = 38.5$mm, and $d = 0.5$mm. According to Fig. 5.2.5, as g increases from 0.5mm to 1mm, the size of the loop increases, indicating an increase in the interaction between the main patch and the parasitic patches. The loop is observed to move in an anticlockwise manner away from the center of the Smith chart as g increases. Since the impedance locus turns in an anticlockwise manner as g increases to 1mm, the matching at the lower frequency degrades, while beginning to improve at the higher frequency. Further increases in g lead to the impedance locus located entirely outside the VSWR = 2 circle.

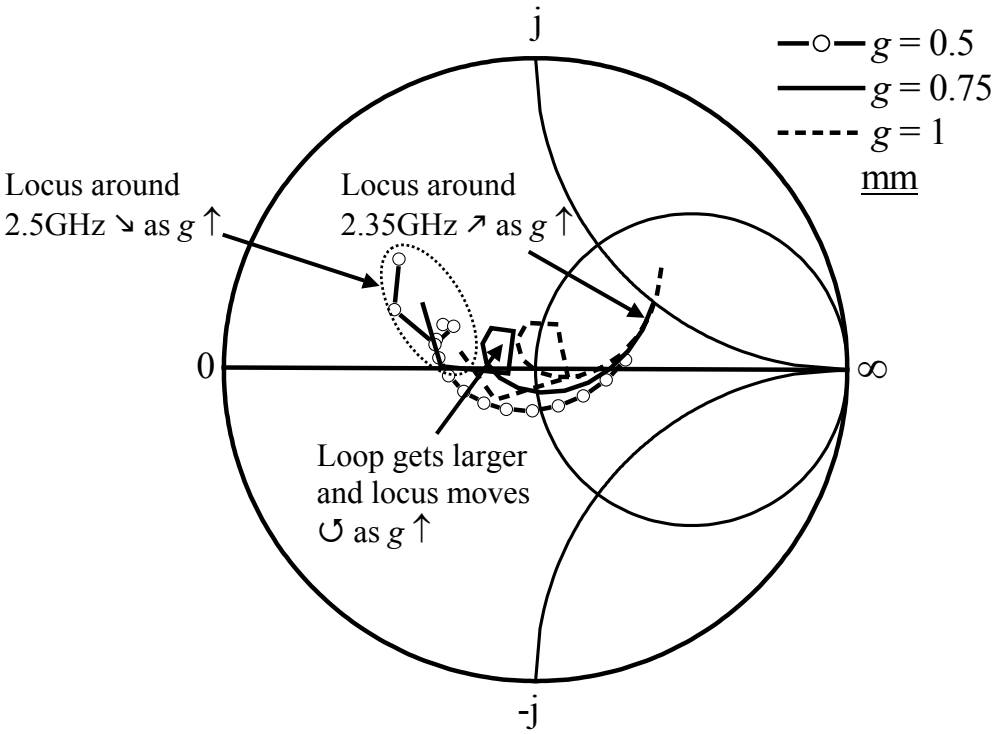

Fig. 5.2.5: Simulated impedance loci for varying gap width g

(e) Effects of varying the probe location

The probe location d from the side of the main patch was varied from 0mm to 8mm with $w_s = l_c = 39.5$mm, $l_s = 38.5$mm, and $g = 0.75$mm. According to Fig. 5.2.6, as d increases, the size of the loop increases slightly. Generally, the impedance performance is relatively unresponsive to the changes in the probe feed location when d is less than 2mm. Subsequent increases in d result in the loop moving outwards towards the left side of the Smith chart in a clockwise manner.

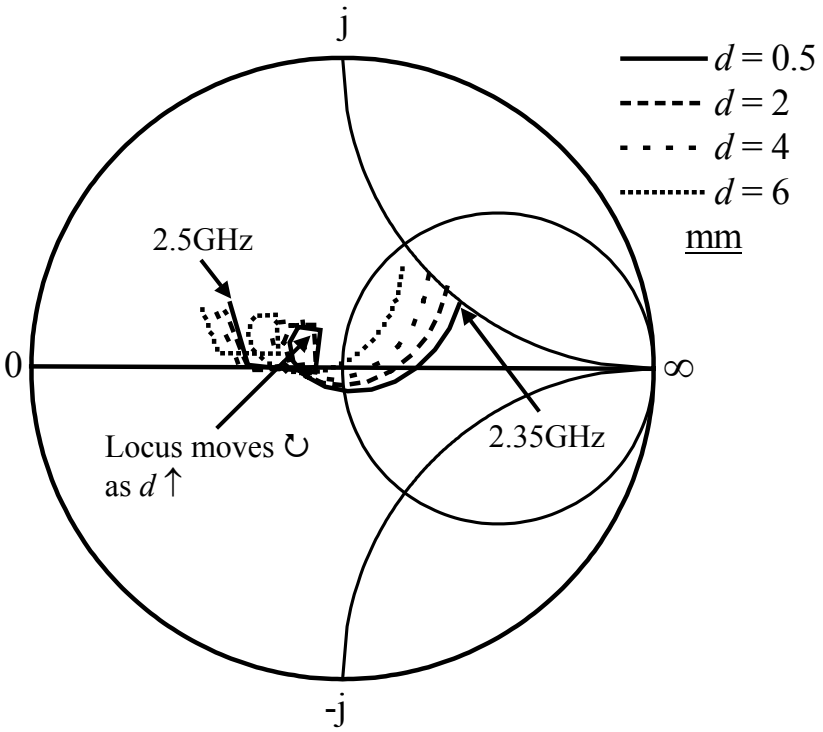

Fig. 5.2.6: Simulated impedance loci for varying probe location *d*

5.2.3 Impedance Performance

With the parametric analysis conducted in the previous section, the impedance performance of the antenna is optimized to operate in the 2.4GHz ISM band. It can be seen from Fig. 5.2.7 for $|S_{11}| \leq -14$dB (VSWR ≤ 1.5), the optimum bandwidth achieved is 4.1% (2.38GHz – 2.48GHz) when $w_s = l_c = 39.5$mm, $l_s = 38.5$mm, $g = 0.75$mm, and $d = 0.5$mm. The isolation $|S_{21}|$ is generally more than 23dB across the entire well-matched bandwidth.

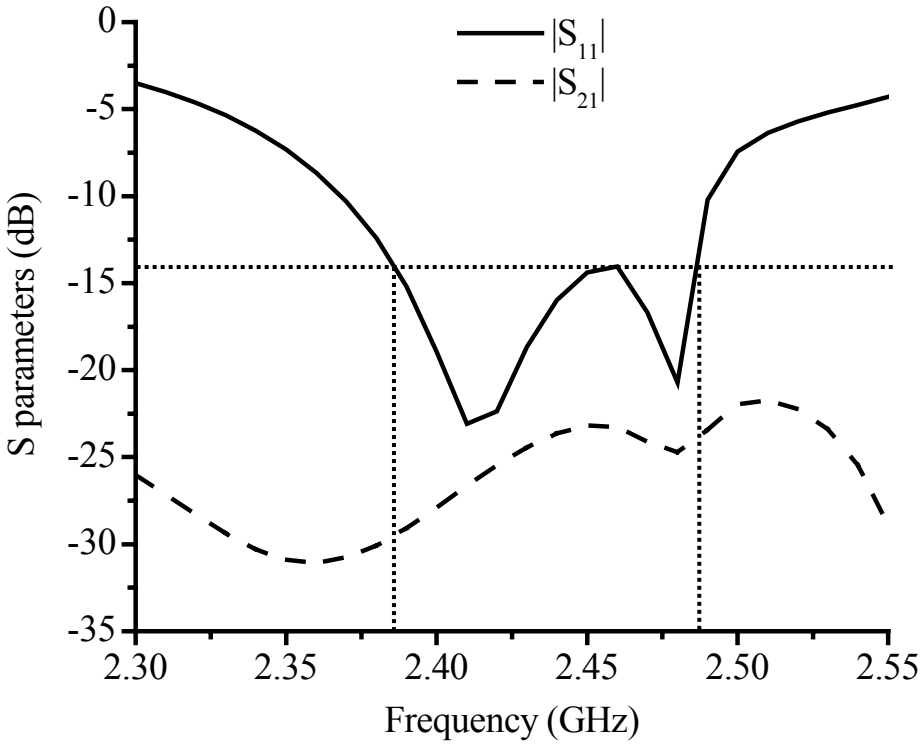

Fig. 5.2.7: Simulated S parameters

5.2.4 Radiation Performance

With the antenna positioned in a ±45° configuration, the radiation patterns were measured at 2.38GHz, 2.43GHz, and 2.48GHz, which correspond to the lower, center, and upper frequency of the bandwidth, respectively. Figs. 5.2.8 – 5.2.10 display the simulated responses for the vertical and horizontal polarizations. Each of the radiation levels was normalized by the total received power. It can be observed that at the lower and center frequencies, the HPBW is about 56° and 60° for the vertical and horizontal polarizations, respectively. However, at the upper frequency, the HPBW for the VP and HP drops to about 53°. Due to the asymmetrical feeding configuration since only one feed point is excited in the analysis, the radiation patterns for both the vertical as

well as horizontal polarizations are asymmetrical and become worse at higher frequencies.

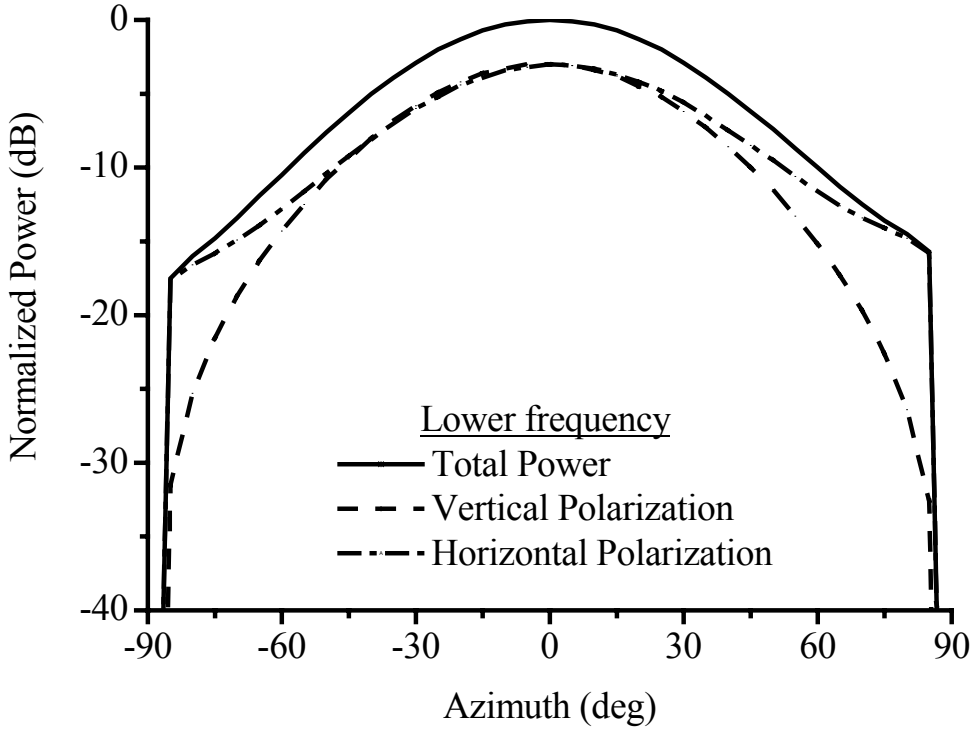

Fig. 5.2.8: Simulated radiation patterns at lower frequency

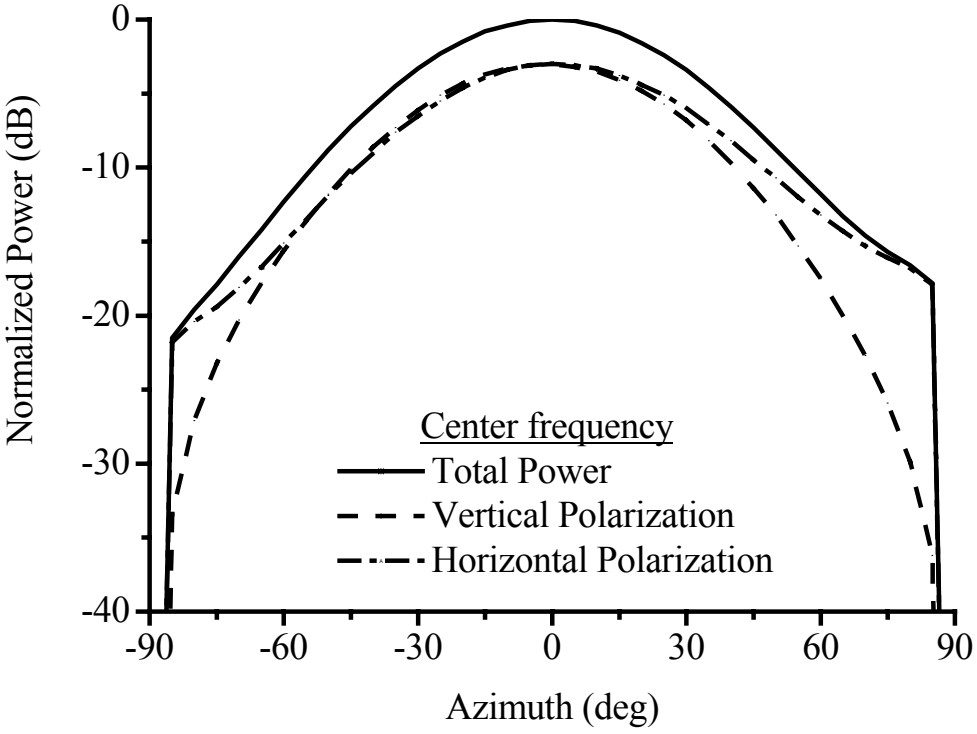

Fig. 5.2.9: Simulated radiation patterns at center frequency

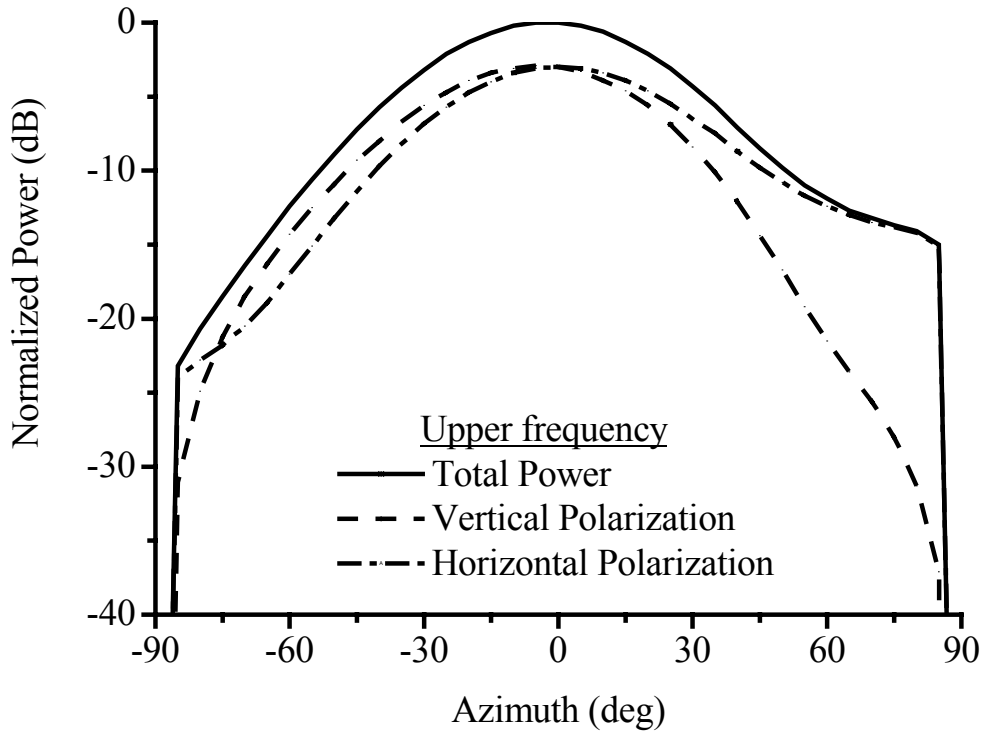

Fig. 5.2.10: Simulated radiation patterns at upper frequency

The coverage, defined as the angular range where the difference between the vertical and horizontal polarizations is less than 6dB, is observed to be 145° at the lower frequency and degrades to 134° at the upper frequency.

In the case of a dual-feed configuration shown in Fig. 5.2.11, where both the feed points are excited in phase simultaneously, the symmetry about the *y-z* plane results in the vertically polarized component E_ϕ in the *x-z* plane and the horizontally polarized component E_θ in the *y-z* plane. From the figure, it can be seen that the cross-polarization radiation levels are at least 26dB lower than the co-polarization cases in both planes.

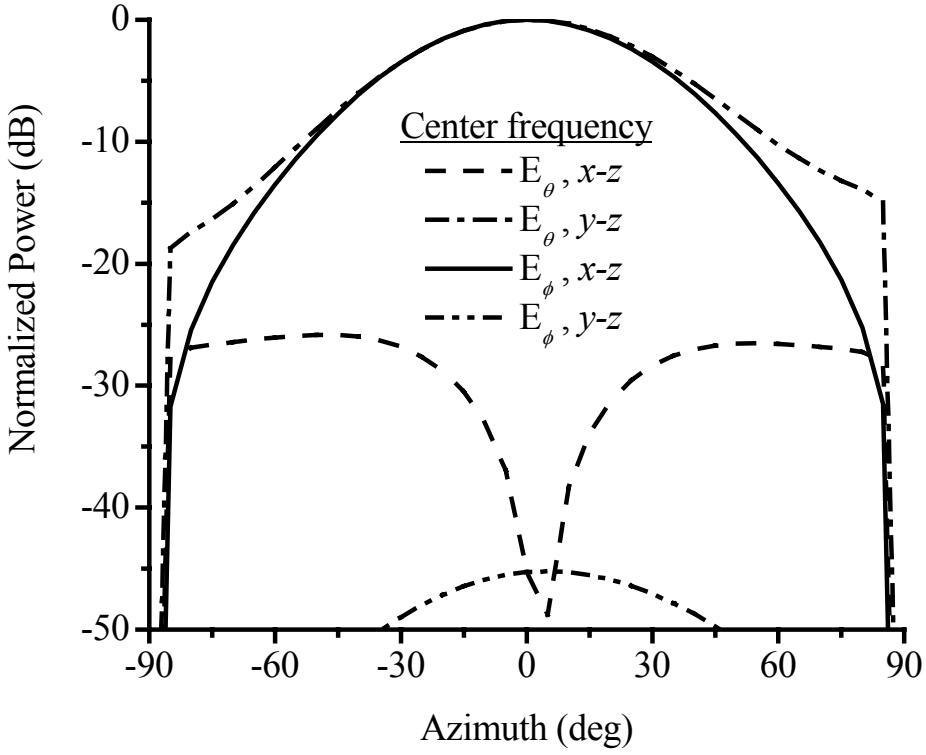

Fig. 5.2.11: Simulated radiation patterns at center frequency with dual-feed excitation

5.2.5 Diversity Performance

Figs. 5.2.12 – 5.2.14 show the calculated far-field coupling, output power correlation, and diversity gain, respectively at the three frequencies using the simulated antenna patterns. The angular range, where the far-field coupling and output power correlation are less than 0.7, is tabulated in Table 5.2.1. The simulated responses show a better coverage at the lower and center frequencies and degrade at the upper frequency due to the increasing deviation of the vertical polarization from the horizontal polarization. The responses generally cover the forward 120° sector well across the bandwidth. In addition, the 3dB coverage for diversity gain is also shown in the table. Generally, the

3dB coverage for the diversity gain is able to cover more than a 120° azimuth across the bandwidth. However, at the upper frequency, the diversity gain experiences a dip of 1.5dB at around -68°.

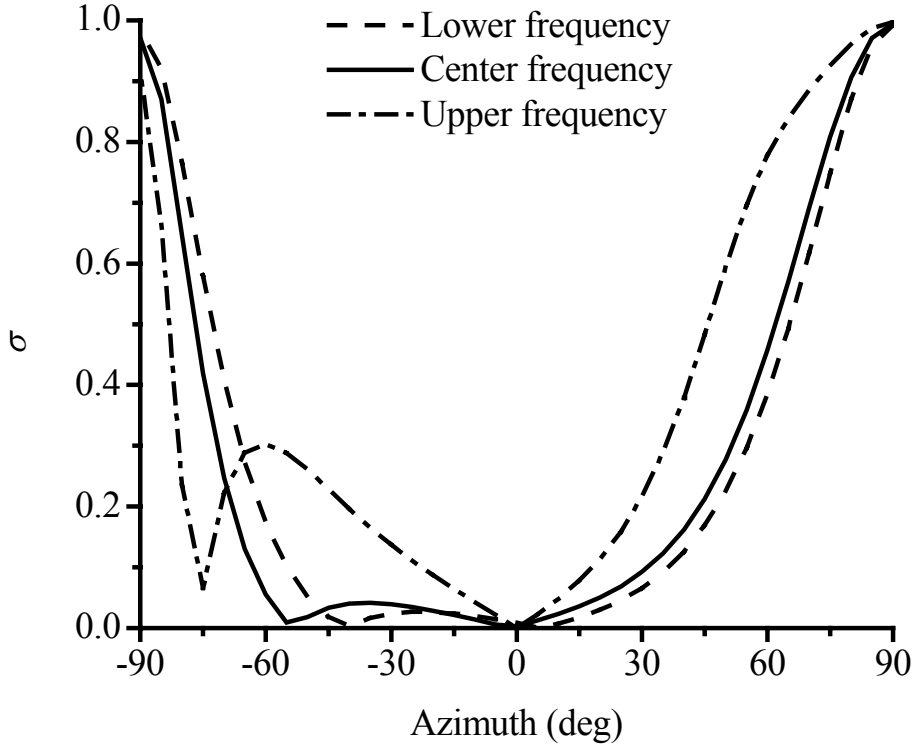

Fig. 5.2.12: Far-field coupling σ at lower, center, and upper frequencies

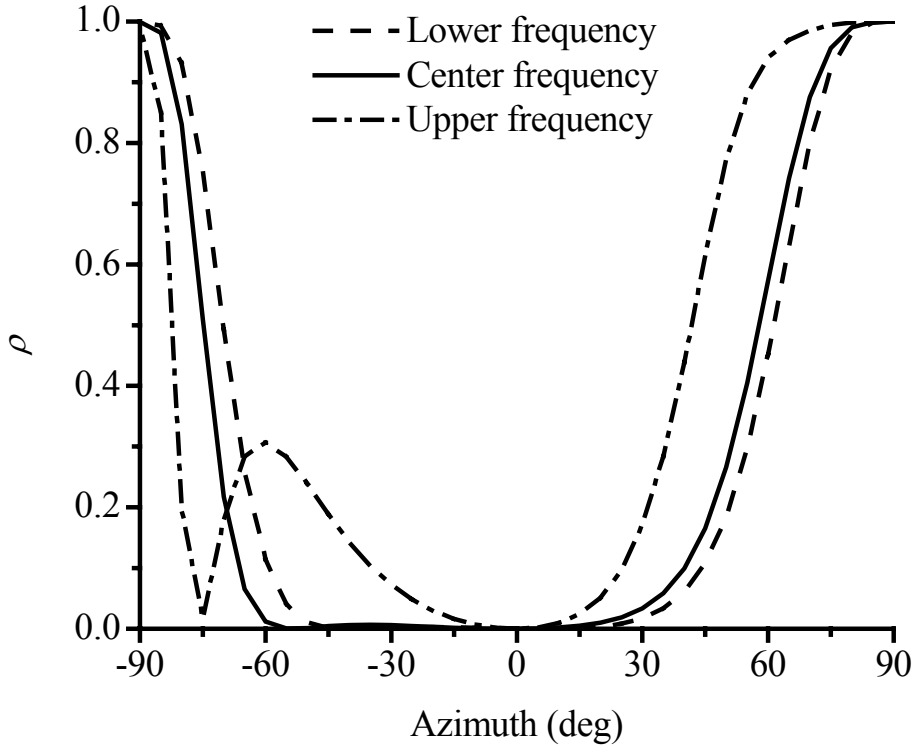

Fig. 5.2.13: Output power correlation ρ at lower, center, and upper frequencies

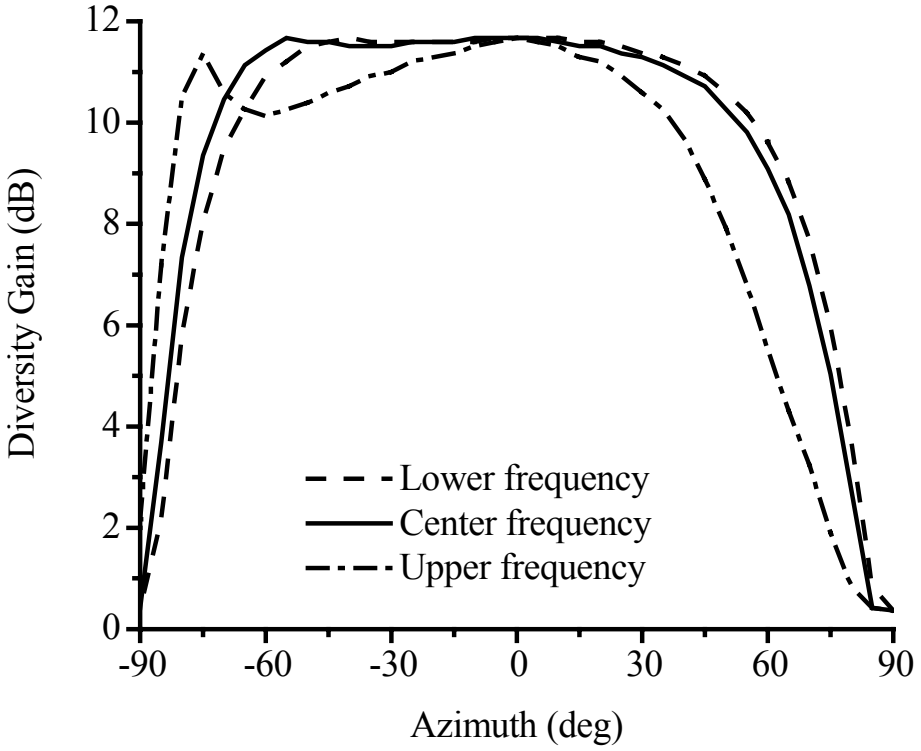

Fig. 5.2.14: Diversity gain at lower, center, and upper frequencies

Table 5.2.1: Simulated angular coverage for far-field coupling, output power correlation, and diversity gain

	Lower frequency	Center frequency	Upper frequency
Far-field coupling	152°	152°	141°
Output power correlation	141°	141°	130°
Diversity gain	138°	138°	129°

5.3 Dual-linear Polarization Suspended Gap-coupled Antenna

In order to reduce the sensitivity of the parameters and increase the impedance bandwidth, an alternative variation of the conventional gap-coupled antenna is considered in this section. Previous research carried out on suspended plate antennas [Huy95][Her98][Luk98][Che01] have shown to achieve a broad impedance bandwidth due to an increase in Q-factor. Henceforth, this suspended technique applied to dual-linear polarization diversity antenna design is investigated. Its diversity performance will be compared with that of the gap-coupled antenna.

5.3.1 Geometry

As shown in Fig. 5.3.1, the design consists of a main patch ($l_c \times l_c$) and four parasitic patches ($l_s \times w_s$) gap-coupled to the main patch. The patches are etched on a 1.52mm-thick substrate (Rogers 4003, $\varepsilon_r = 3.38$). The parasitic patches are separated from the main patch by a gap width g. The dielectric is suspended at a height h above the ground plane. Two adjacent 50Ω co-axial probes of radius 0.6mm excite the main patch at d from its sides. The dimensions for the main and the parasitic patches are selected such that the resonances occur within the 2.4GHz ISM band.

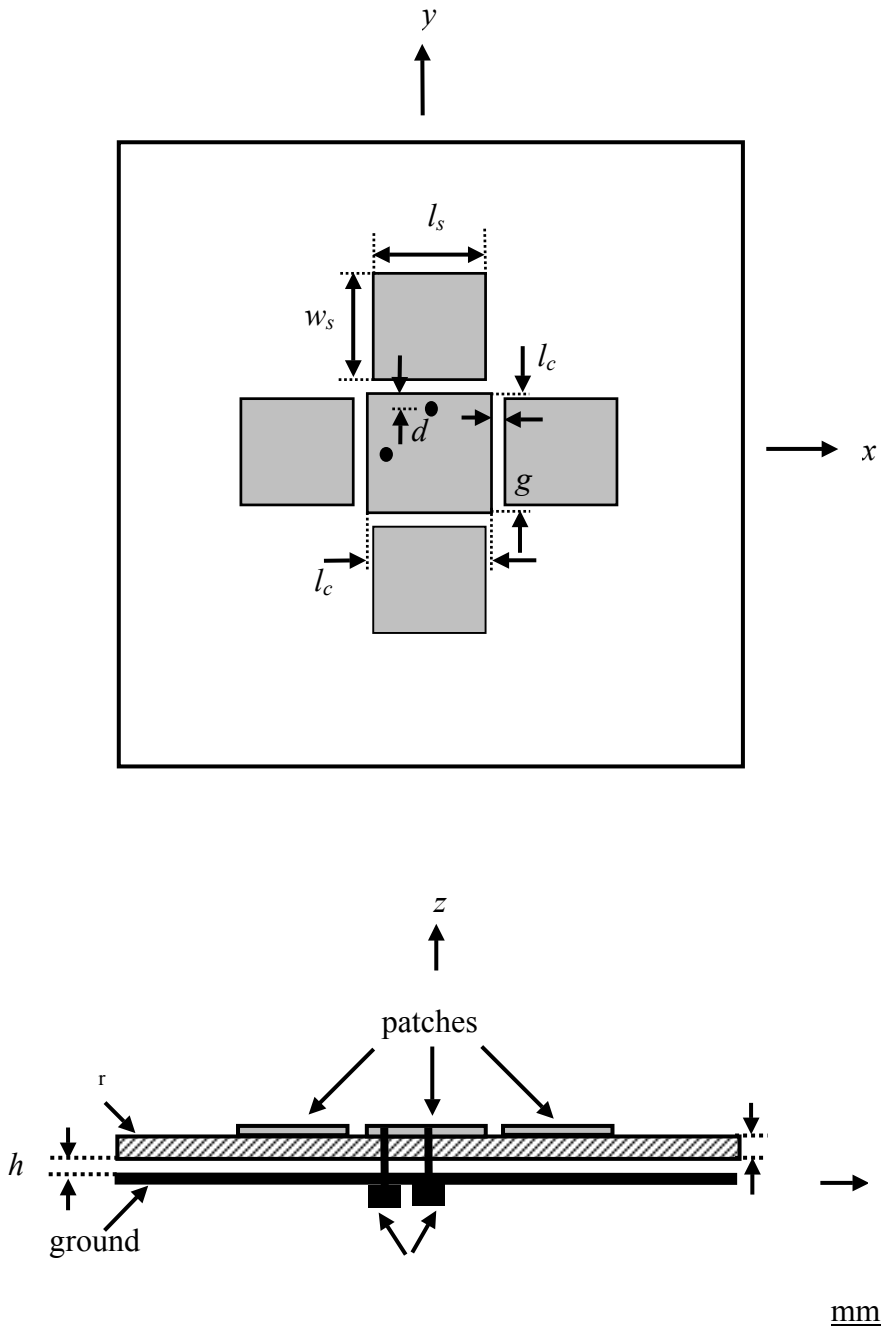

Fig. 5.3.1: Geometry of a suspended gap-coupled antenna

5.3.2 Parametric Study

In this section, a parametric study will be conducted to investigate the influence of physical parameters such as the size of main and parasitic patches, gap width, suspended height above the ground plane, and location of feed point on the impedance matching.

(a) Effects of varying the size of main patch

The size of the main patch l_c was varied from 42mm to 44mm with $w_s = l_c$, $l_s = 33$mm, $d = 2$mm, $h = 3$mm, and $g = 2$mm. According to Fig. 5.3.2, varying l_c generally has a significant effect on the resonant frequency. An increase in l_c generally lowers the resonant frequency. Similar to the gap-coupled antenna, the loop moves in an anticlockwise manner with an increase in l_c. In addition, as l_c increases, the frequency points around the lower frequency is observed to move towards the center of the Smith chart, while those around the upper frequency moves away. However, for the suspended gap-coupled antenna, the loop size of the impedance loci is relatively unresponsive to the changes in l_c.

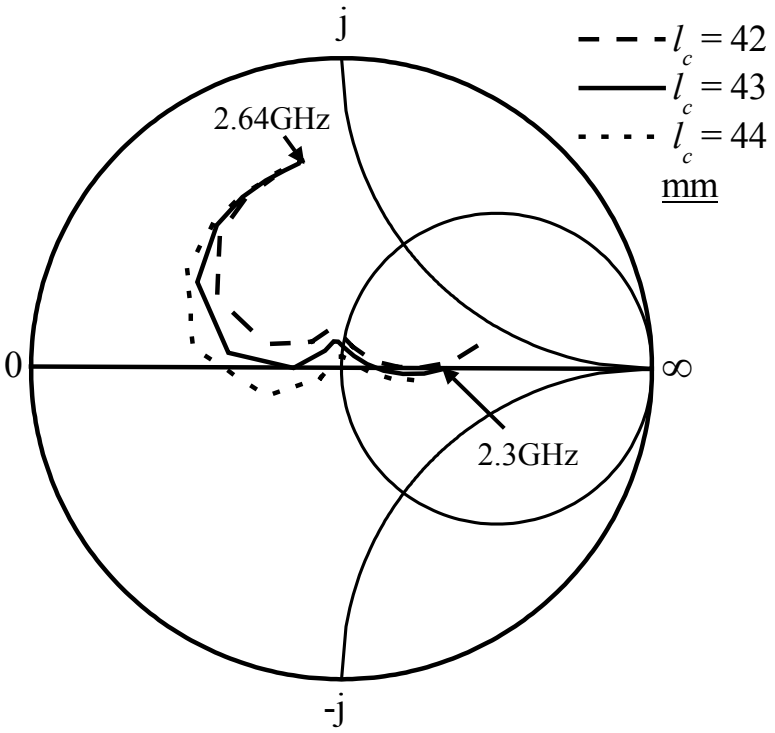

Fig. 5.3.2: Simulated impedance loci for varying size l_c of main patch

(b) Effects of varying the length of parasitic patch

As illustrated in Fig. 5.3.3, the length of the parasitic patch l_s was varied from 32mm to 34mm with $w_s = l_c = 43$mm, $d = 2$mm, $h = 3$mm, and $g = 2$mm. Similar to the case for the gap-coupled antenna, the impedance locus turns in a clockwise manner as l_s increases and as a result, the matching at the lower frequency improves while beginning to degrade at the higher frequency.

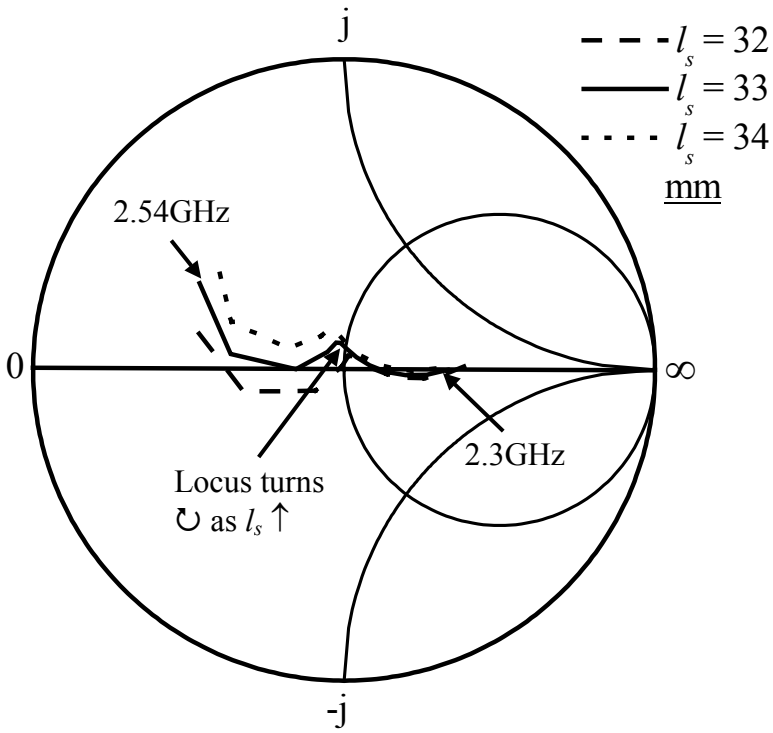

Fig. 5.3.3: Simulated impedance loci for varying length l_s of parasitic patch

(c) Effects of varying the width of parasitic patch

The width of the parasitic patch w_s was varied from 42mm to 44mm with l_s = 33mm, l_c = 43mm, d = 2mm, h = 3mm, and g = 2mm. According to Fig. 5.3.4, varying w_s generally has a significant effect on the impedance matching. It can be observed that the loop gradually disappears when w_s is lower than 42mm. As w_s increases, the frequency points in the vicinity of the loop have a lower frequency. In addition, the length of the impedance locus increases, which implies that the frequency points, especially that of the higher frequency, are now spaced further apart.

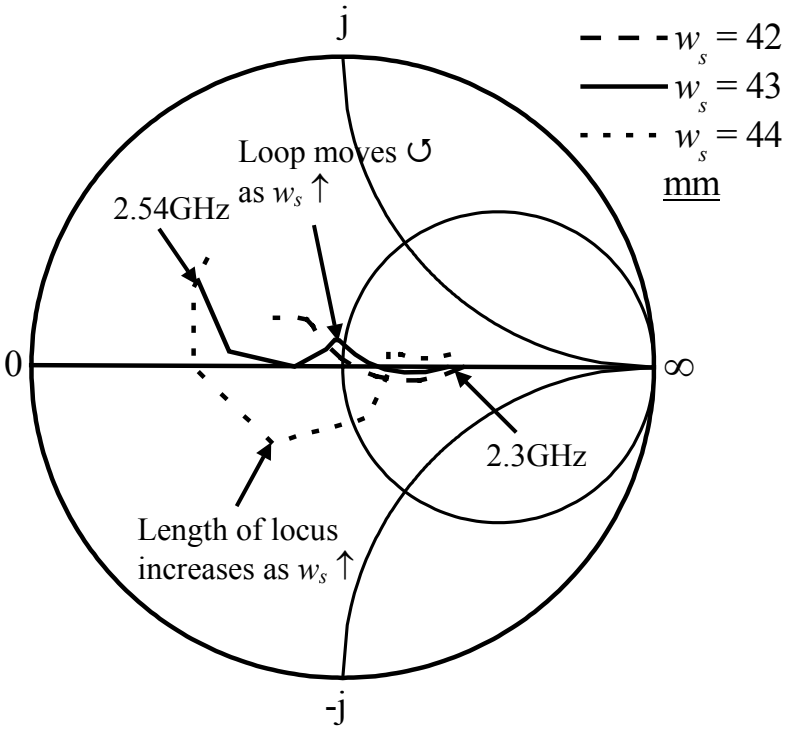

Fig. 5.3.4: Simulated impedance loci for varying width w_s of parasitic patch

(d) Effects of varying the gap width

The gap width g was varied from 1.5mm to 2.5mm with $w_s = l_c = 43$mm, $l_s = 33$mm, $d = 2$mm, and $h = 3$mm. According to Fig. 5.3.5, as g increases, the interaction between the main patch and the parasitic patches is relatively unaffected since the loop size remains the same. Similar to the gap-coupled antenna, the loop is observed to move in an anticlockwise manner away from the center of the Smith chart as g increases. Since the impedance locus turns in an anticlockwise manner as g increases, the matching at the lower frequency degrades while beginning to improve at the higher frequency. Further increases in g will lead to the impedance locus moving towards to the inductive region, i.e. upper half-space of the Smith chart.

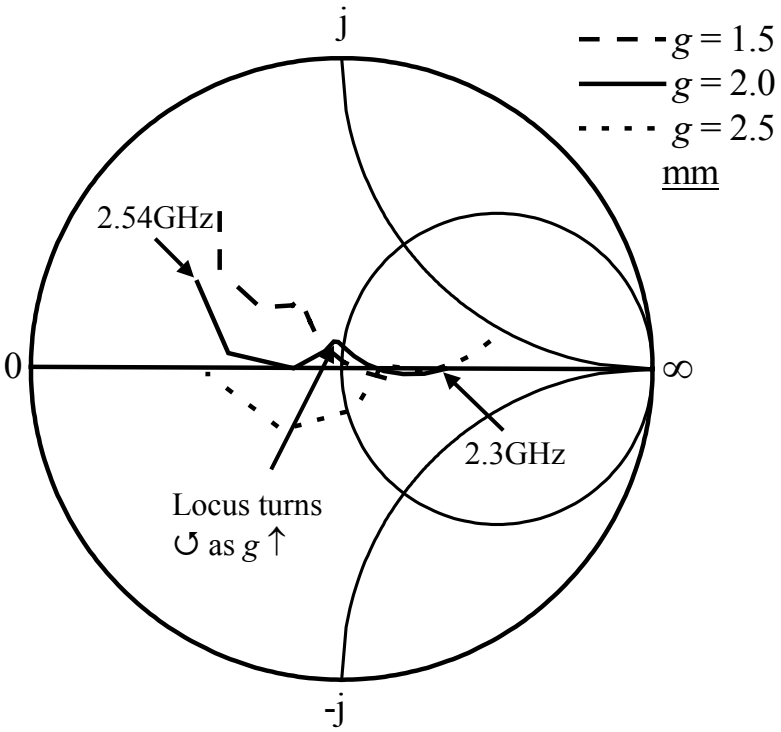

Fig. 5.3.5: Simulated impedance loci for varying gap width *g*

(e) Effects of varying the probe location

The probe location *d* from the side of the main patch was varied from 0mm to 4mm with $w_s = l_c = 43$mm, $l_s = 33$mm, $g = 2$mm, and $h = 3$mm. According to Fig. 5.3.6, the impedance performance is relatively unresponsive to changes in the probe feed location.

(f) Effects of varying the spacing above ground plane

The distance between the dielectric and the ground plane *h* was varied from 2mm to 4mm with $w_s = l_c = 43$mm, $l_s = 33$mm, $g = 2$mm, and $d = 2$mm. From Fig. 5.3.7, it can be observed that the impedance matching is very responsive to the change in *h*. The length of the locus increases with a decrease in *h*, because the frequency points, especially corresponding to the higher frequencies, are more widely spaced. The loop

rotates in a clockwise manner with an increase in *h* and moves from a capacitive (lower half-space) to an inductive region (upper half-space).

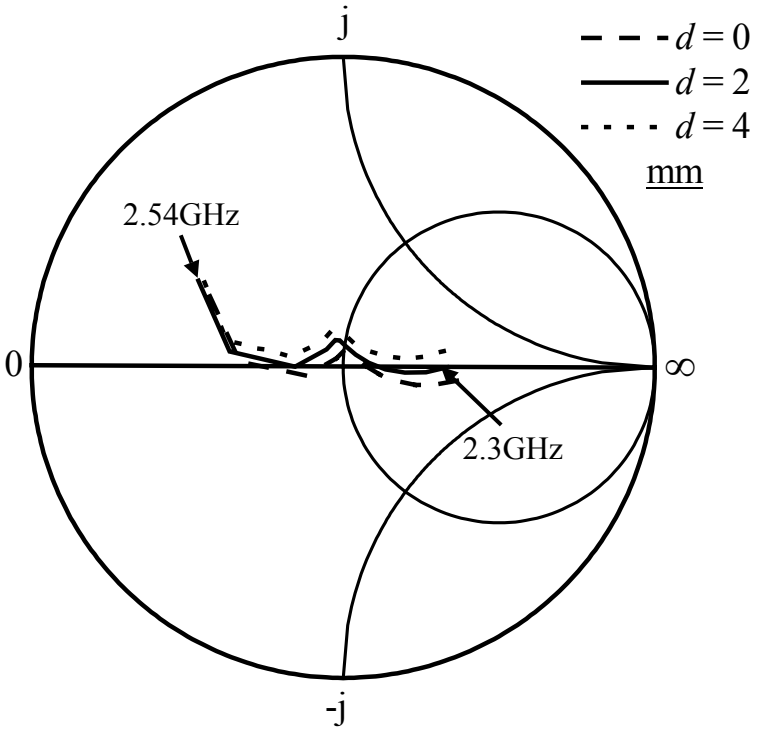

Fig. 5.3.6: Simulated impedance loci for varying probe location *d*

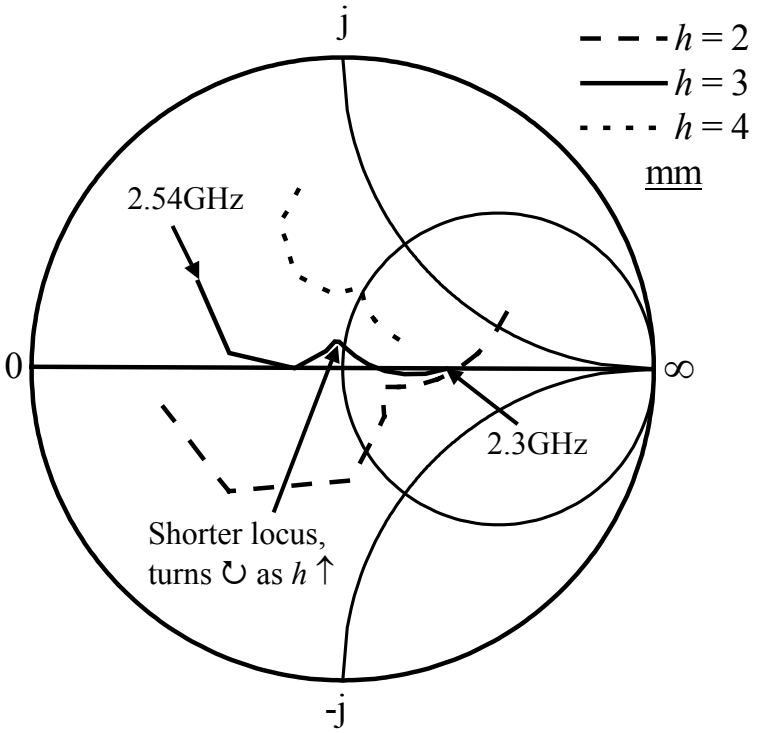

Fig. 5.3.7: Simulated impedance loci for varying spacing *h* above ground plane

5.3.3 Impedance Performance

With the parametric analysis conducted in the previous section, a prototype with the optimized parameters was fabricated and the input impedance measured in the 2.4GHz ISM band. It can be seen from Fig. 5.3.8 for VSWR ≤ 1.5 ($|S_{11}| \leq$ -14dB), the optimum measured bandwidth achieved is about 6.2% (2.33GHz – 2.48GHz) when $w_s = l_c =$ 43mm, $l_s =$ 33mm, $g =$ 2mm, $d =$ 2mm, and $h =$ 4mm. The results generally tally well with those predicted from simulations.

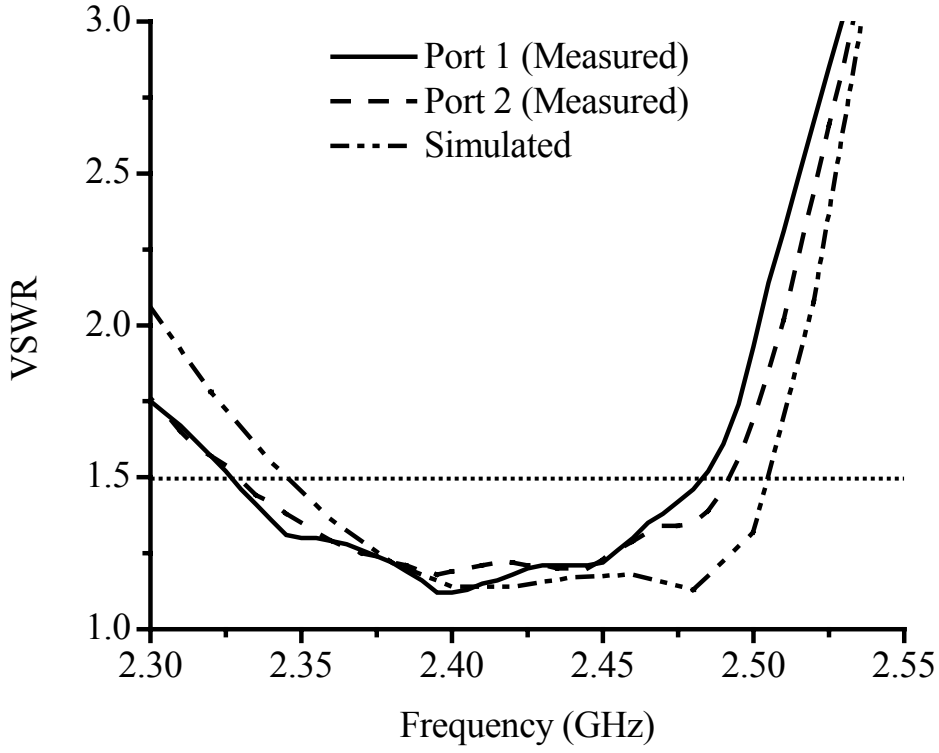

Fig. 5.3.8: Measured and simulated VSWR

The port coupling $|S_{21}|$ is also analyzed from simulations as shown in Fig. 5.3.9. It can be observed that the degree of sensitivity of $|S_{21}|$ towards each parameter is different.

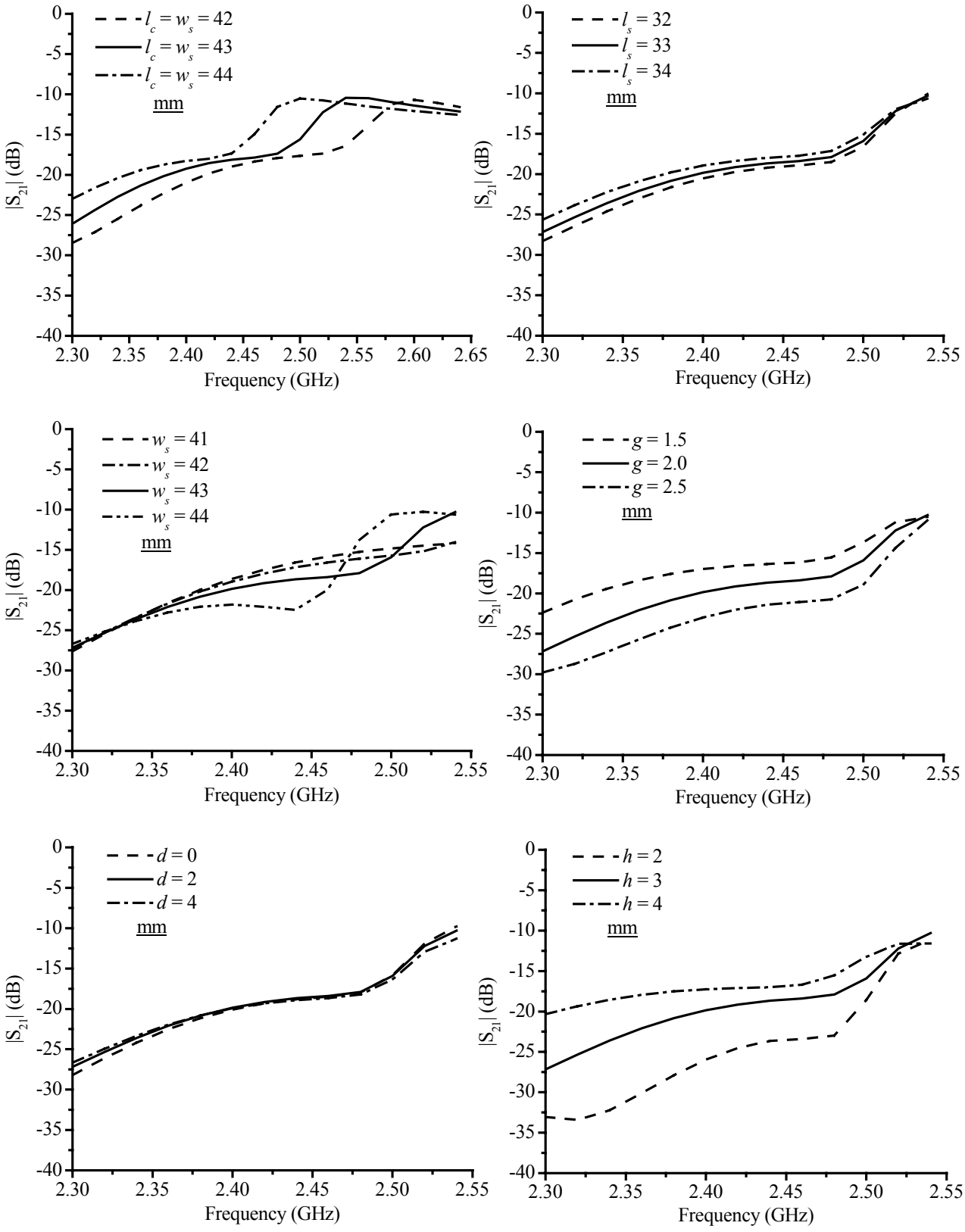

Fig. 5.3.9: Parametric study for $|S_{21}|$

From the figures, it is observed that varying the gap width as well as the spacing between the dielectric and ground plane has a significant effect on the response. The width of the parasitic patches shows a great fluctuation across the ISM band when w_s = 44mm. However, the effect of the length of the parasitic patches and the probe location on the $|S_{21}|$ response is relatively small. Fig. 5.3.10 illustrates the simulated and measured $|S_{21}|$ for the optimized parameters. It can be seen that the measured $|S_{21}|$ is generally less than –17dB across the impedance bandwidth.

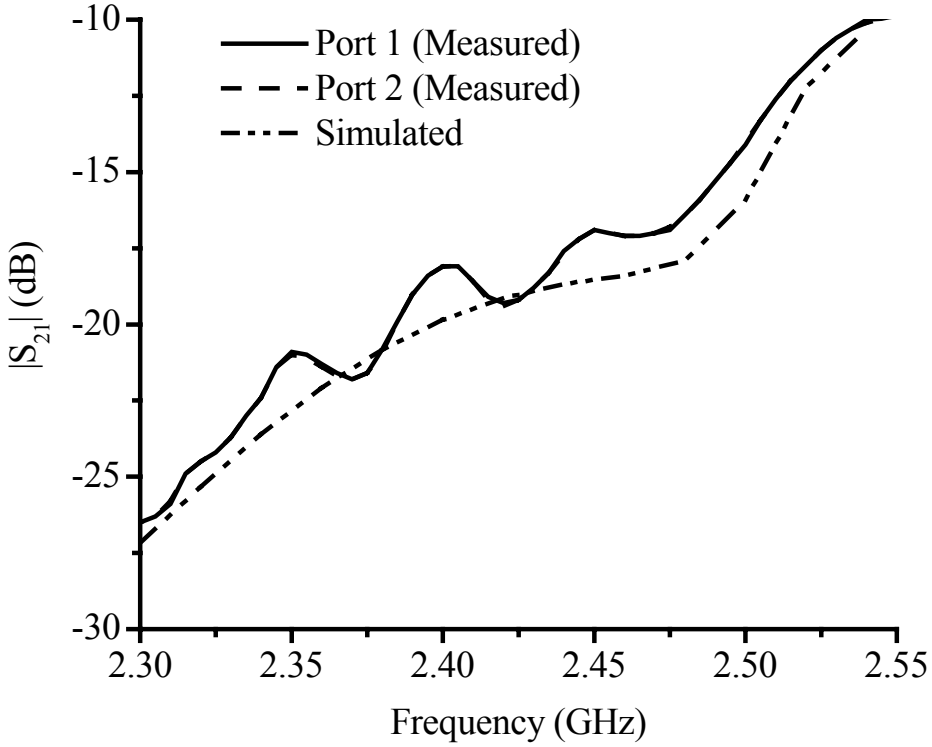

Fig. 5.3.10: Measured and simulated $|S_{21}|$

5.3.4 Radiation Performance

The radiation patterns were measured in an anechoic chamber at 2.33GHz, 2.40GHz, and 2.48GHz, which correspond to the lower, center, and upper frequency of the bandwidth, respectively. Figs. 5.3.11 – 5.3.13 display the simulated and measured

responses for the vertical and horizontal polarizations. Each of the radiation levels was normalized by the total received power. It can be observed that at the three frequencies, the measured responses for the vertical polarizations are close to the simulated responses. The half-power beamwidth (HPBW) for the vertical and horizontal polarizations as well as the coverage (defined as the angular range where the difference between the vertical and horizontal polarizations is less than 6dB) are noted and tabulated in Table 5.3.1.

It can be observed that the beamwidth for the vertical polarization (VP) is generally wider than that for the horizontal polarization (HP) at all three frequencies. Generally, the beamwidths for both VP and HP decrease as the frequency increases. Across the impedance bandwidth, the coverage covers the forward 120° sector well as predicted from the simulations.

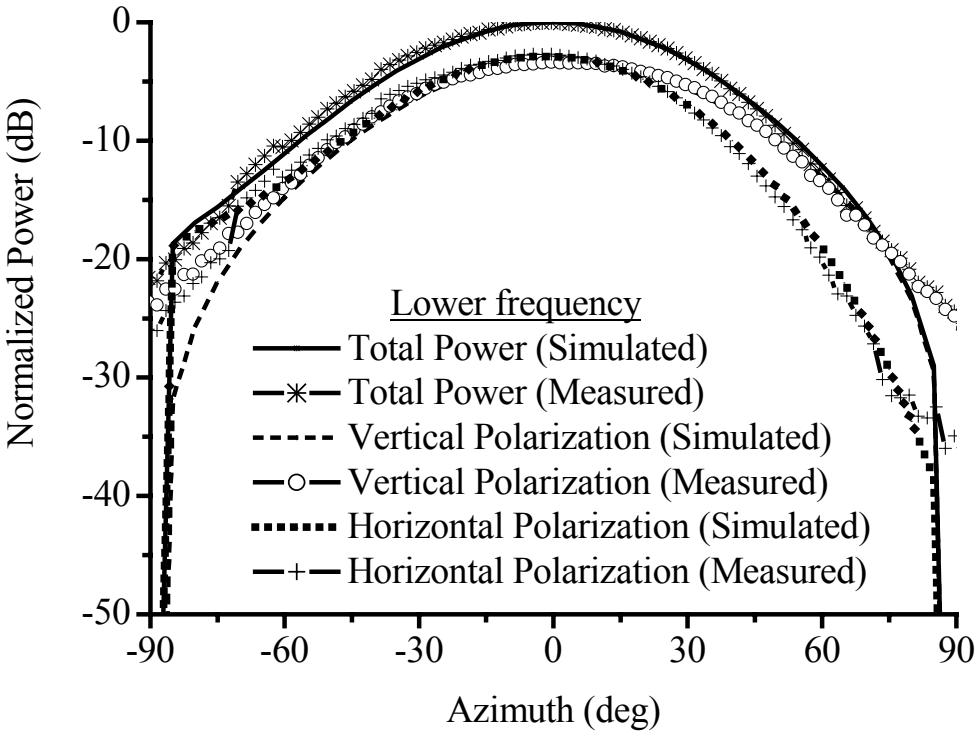

Fig. 5.3.11: Measured and simulated radiation patterns at lower frequency

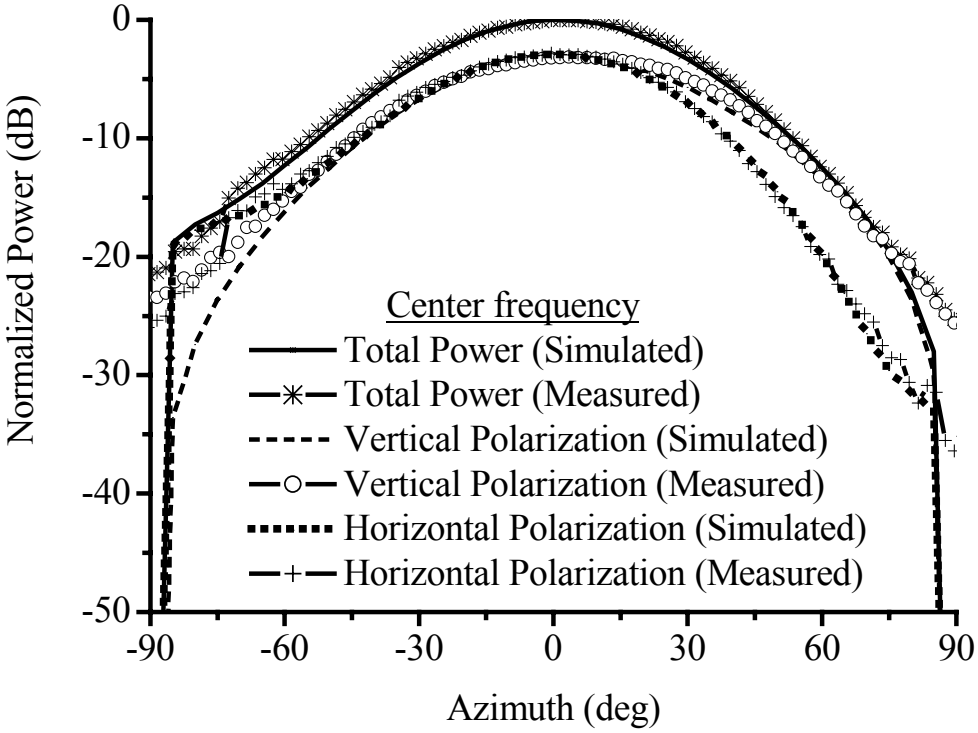

Fig. 5.3.12: Measured and simulated radiation patterns at center frequency

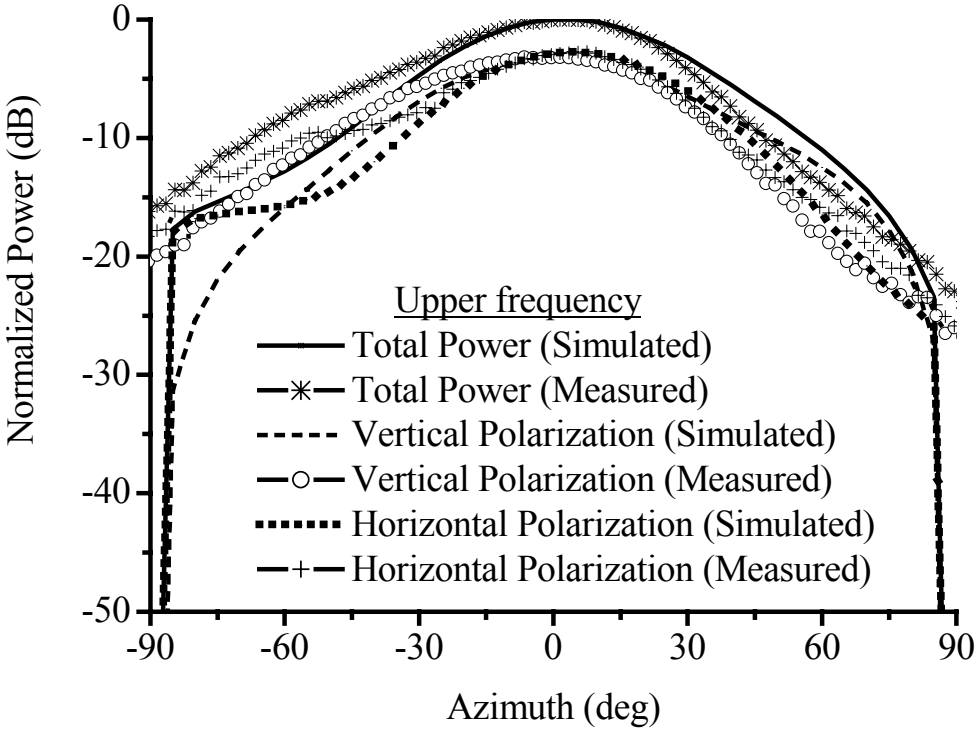

Fig. 5.3.13: Measured and simulated radiation patterns at upper frequency

Table 5.3.1: Measured and simulated HPBW and coverage

	Lower frequency		Center frequency		Upper frequency	
	Simulated	Measured	Simulated	Measured	Simulated	Measured
HPBW (VP)	62°	69°	59°	65°	55°	59°
HPBW (HP)	57°	59°	52°	56°	49°	49°
Coverage	136°	142°	130°	150°	150°	180°

5.3.5 Diversity Performance

Figs. 5.3.14 – 5.3.16 show the simulated and measured far-field coupling at the lower, center, and upper frequency of the bandwidth, respectively. The measured results generally agree well with the simulations from –70° to 90° at the three frequencies. However, after –70°, the measured results are better than the simulations arising from a smaller difference between the VP and HP due to the cable effects during measurement. At the upper frequency, the overall far-field coupling response degraded, which is due to the deviation of the VP and the HP patterns.

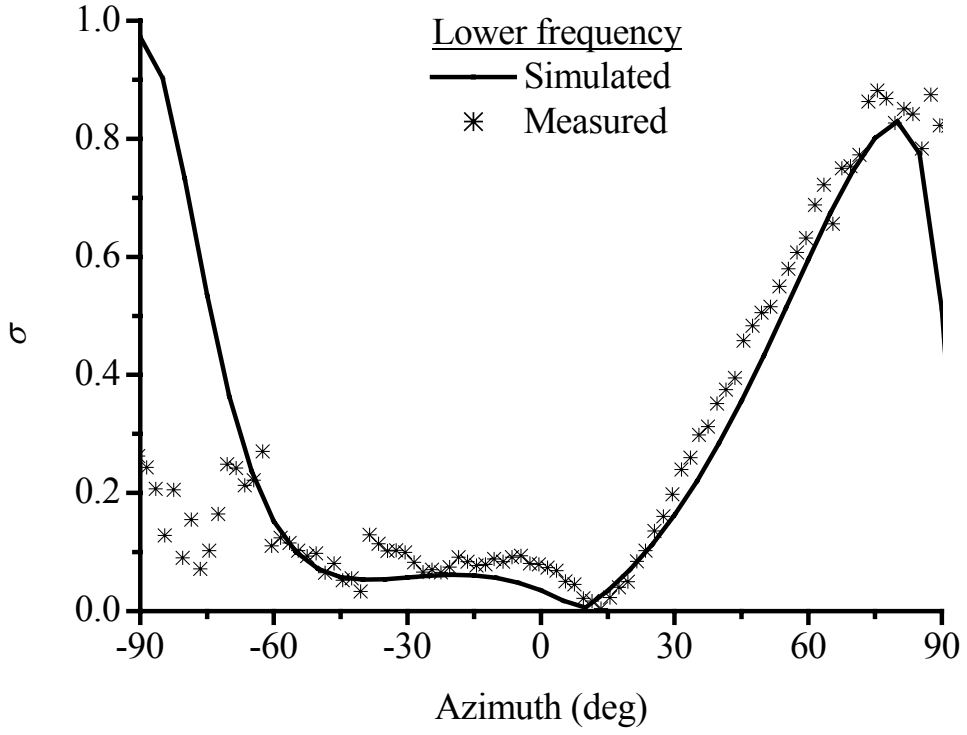

Fig. 5.3.14: Measured and simulated far-field coupling σ at lower frequency

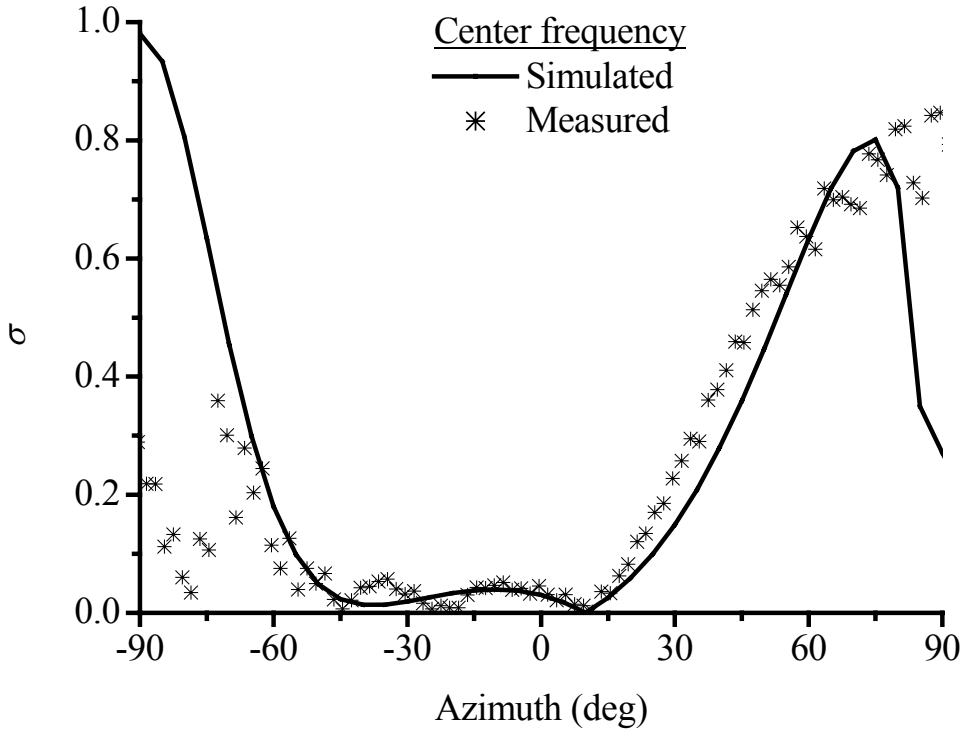

Fig. 5.3.15: Measured and simulated far-field coupling σ at center frequency

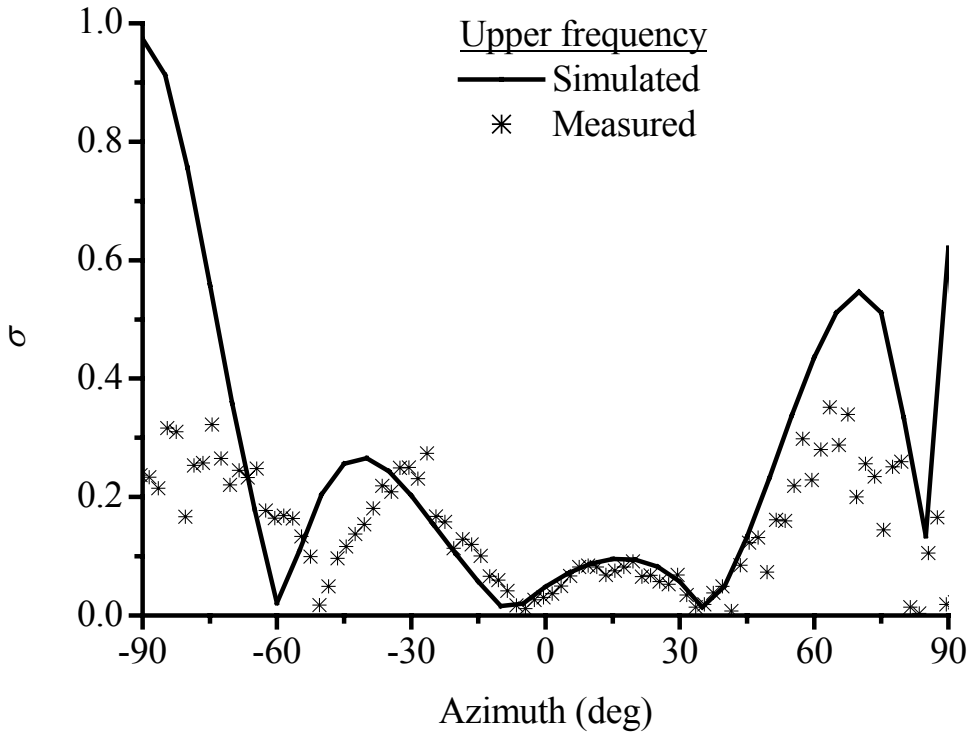

Fig. 5.3.16: Measured and simulated far-field coupling σ at upper frequency

The measured and simulated output power correlation at the lower, center, and upper frequencies of the bandwidth are shown in Figs. 5.3.17 – 5.3.19, respectively in a non-fading channel. It can be seen that for the χ < 5dB, the correlation is generally less than 0.7. The coverage of the measured correlation, defined as the angular range where the correlation is less than 0.7, is greater than 130° across the impedance bandwidth.

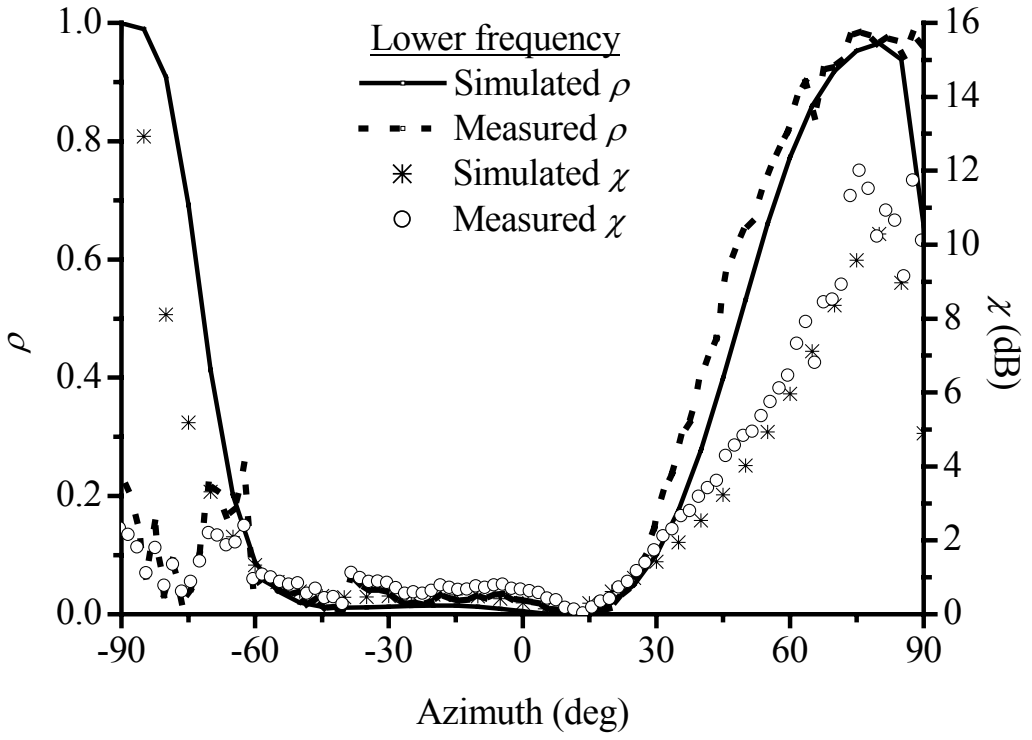

Fig. 5.3.17: Measured and simulated output power correlation ρ and cross-polar discrimination χ at lower frequency

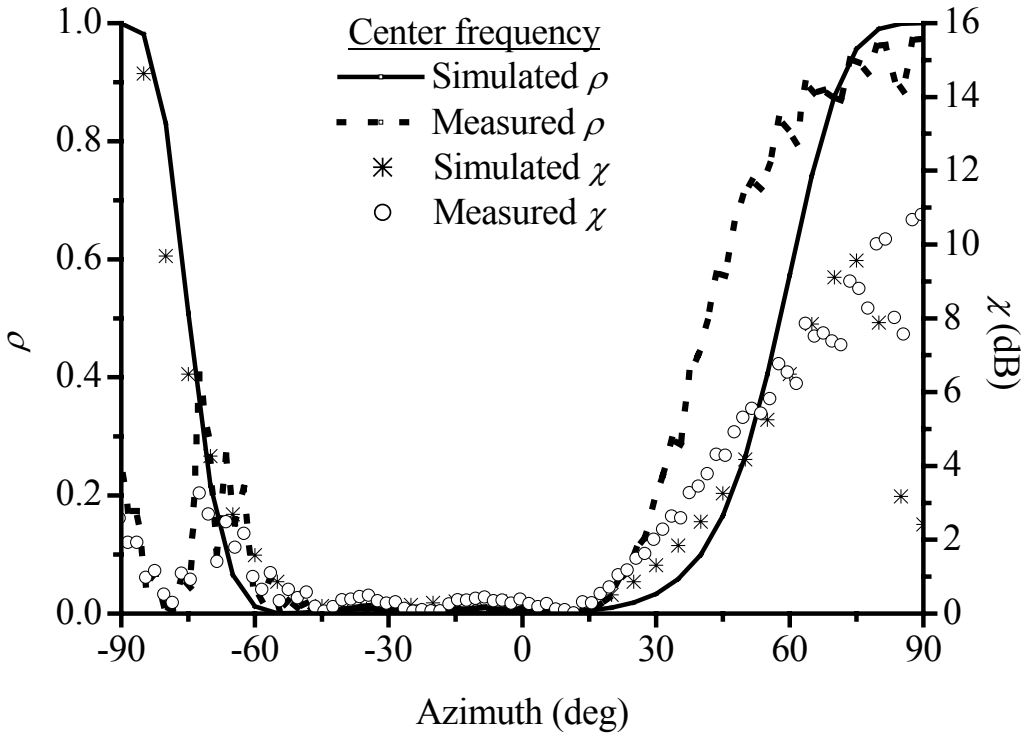

Fig. 5.3.18: Measured and simulated output power correlation ρ and cross-polar discrimination χ at center frequency

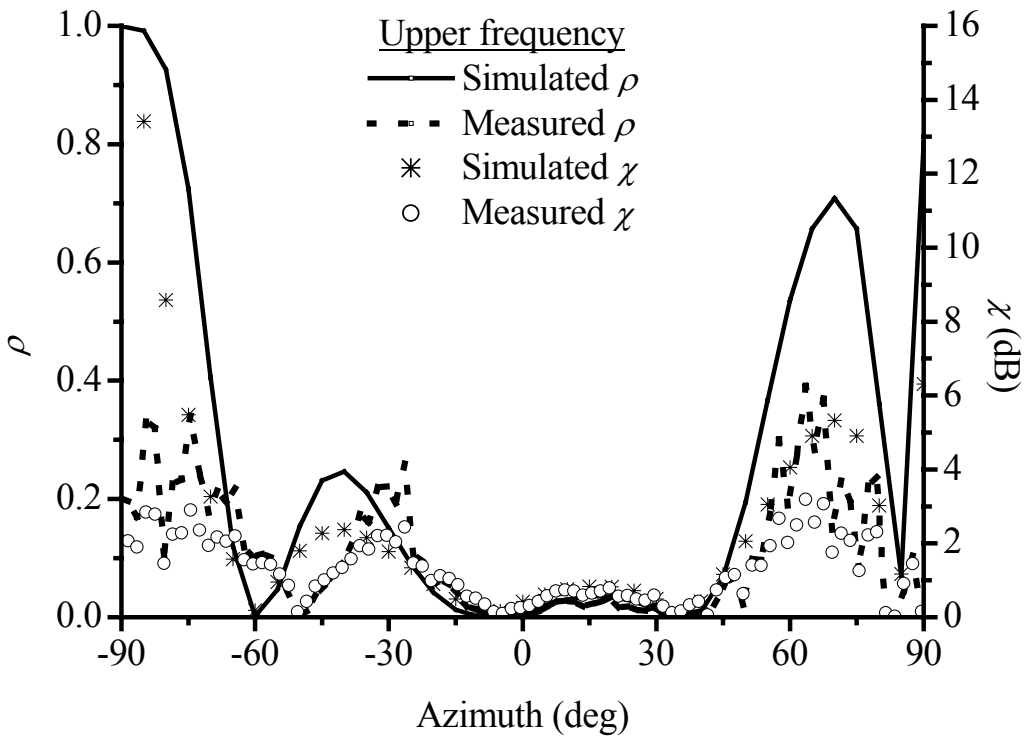

Fig. 5.3.19: Measured and simulated output power correlation ρ and cross-polar discrimination χ at upper frequency

he measured and simulated diversity gain performances at 1% outage rate at the three frequencies are shown in Figs. 5.3.20 – 5.3.22. The maximum diversity gain of 11.7dB occurs when the far-field coupling is at its minimum and when χ = 0dB. Generally, the 3dB coverage for the diversity gain is able to cover more than a 120° azimuth across the bandwidth. However, at the upper frequency, the measured diversity gain experiences a dip of 1.2dB and 1.7dB at around –30° and 68°, respectively. The coverage at the upper frequency is better than those at the lower and center frequencies as predicted from simulations. The measured and simulated coverage for the far-field coupling, output power correlation, and diversity gain are tabulated in Table 5.3.2.

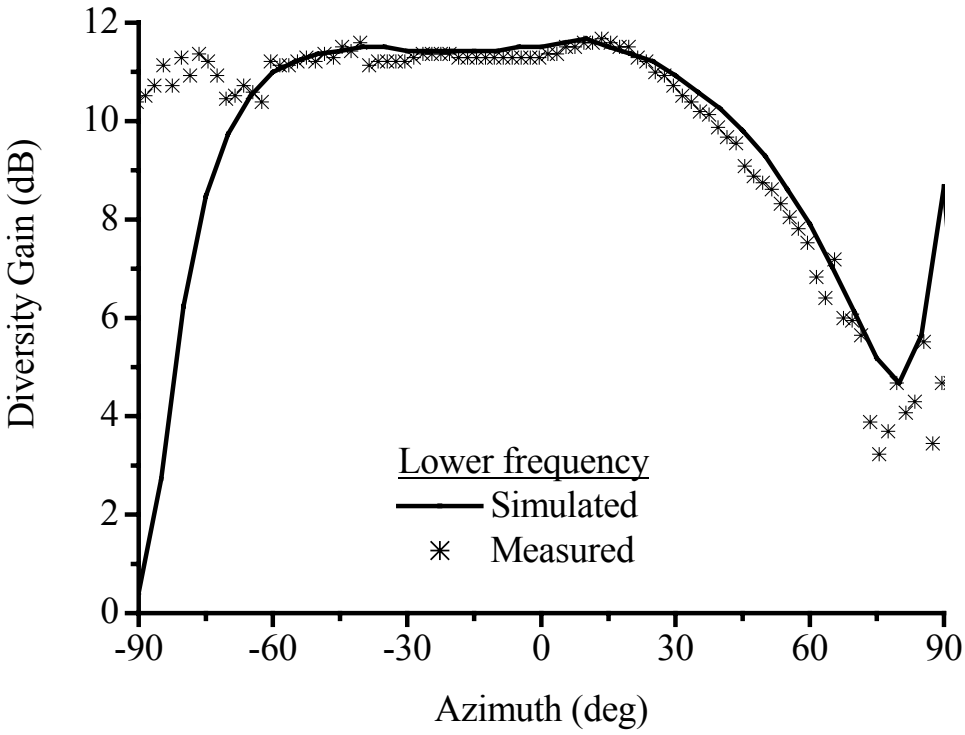

Fig. 5.3.20: Measured and simulated diversity gain at lower frequency

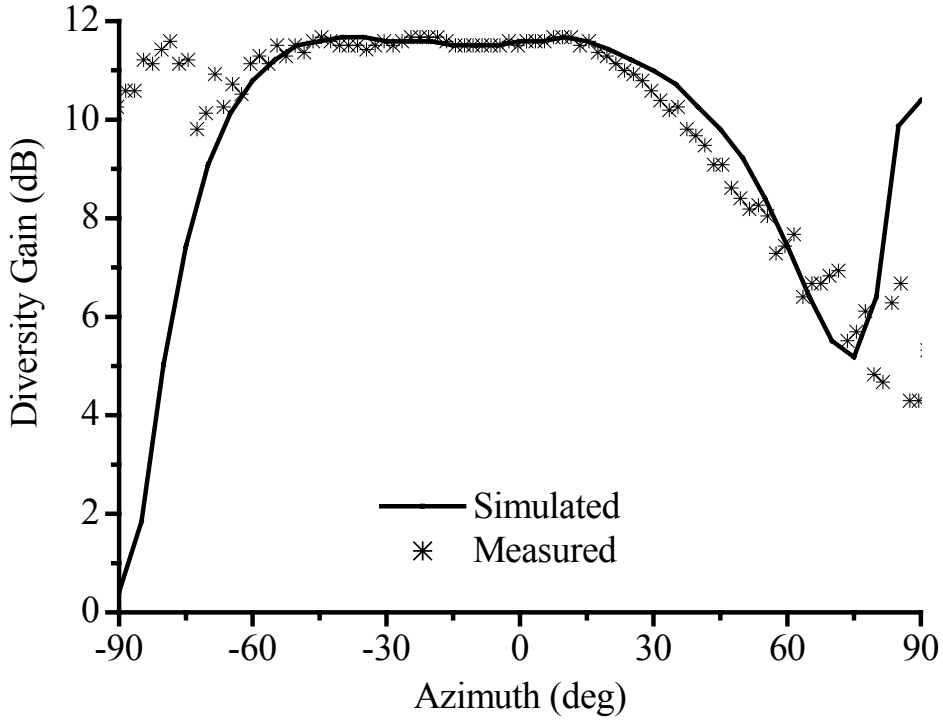

Fig. 5.3.21: Measured and simulated diversity gain at center frequency

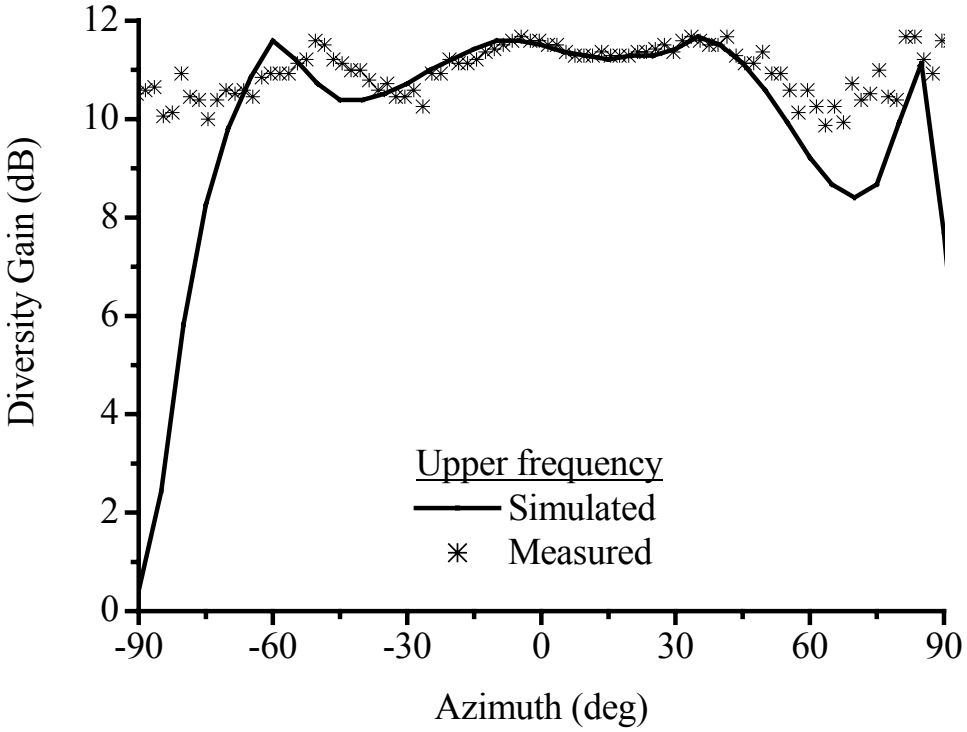

Fig. 5.3.22: Measured and simulated diversity gain at upper frequency

Table 5.3.2: Measured and simulated angular coverage for far-field coupling, output power correlation, and diversity gain

	Lower frequency		Center frequency		Upper frequency	
	Simulated	Measured	Simulated	Measured	Simulated	Measured
Far-field coupling	146°	153°	141°	153°	169°	180°
Output power correlation	132°	143°	142°	140°	163°	180°
Diversity gain	129°	142°	125°	138°	164°	180°

5.4 Conclusions

In this Chapter, two dual-linear polarized gap-coupled antenna designs have been presented, and their impedance, radiation, and diversity performances analyzed across the bandwidth. For the gap-coupled antenna, the impedance performance is very sensitive to the changes in the antenna parameters from the parametric study conducted. Good diversity gain coverage of more than 129° has been achieved, but experienced the degradation at the upper frequency of the bandwidth. An alternative design was proposed to increase the impedance bandwidth and at the same time improve the diversity performance. By suspending the dielectric layer above the ground plane, impedance matching has been found to be easier as the sensitivity of the parameters is reduced. The measured results have shown that the diversity gain coverage at the upper frequency is improved significantly, with no deterioration at the lower and center frequencies. Therefore, the suspended gap-coupled antenna is suitable for polarization diversity applications.

Chapter 6

CONCLUSIONS

In this research project, the focus is on the design of single-feed dual-linear polarization antennas, as well as the design and analysis of the diversity performance of dual-feed polarization diversity antennas for WLAN or 3G base station applications.

In the first part of the Thesis, a single-feed stacked patch antenna was presented. With a diagonal feed technique, dual-linear polarization characteristics can be achieved. In order to increase the antenna gain, a two-element linear, and 2 × 2 planar arrays were constructed. The antenna element and the arrays are able to achieve an impedance bandwidth of 13% and 16%, respectively, within the 2.4GHz ISM band. In order to ensure that the radiation performance is satisfactory across the bandwidth, it was evaluated at three frequencies, corresponding to the lower, center, and upper frequencies of the bandwidth. The measured results have shown that the arrays can achieve a front-to-back ratio of greater than 20dB in both the *x*-*z* and *y*-*z* planes, which can be further improved if a larger ground plane was used in the measurements.

Besides considering the front-to-back ratio, it is also desirable that the variation in the radiation patterns is minimal across the impedance bandwidth, especially at the boresight. The variation is generally less than 2.7dB for the stacked element and arrays. In addition, to maintain good dual-linear polarization characteristics, the difference between the vertical and horizontal polarized components must be kept as low as possible. It has been demonstrated that the difference is less than 2.2dB in both

principal planes for the two-element linear and 2 × 2 planar arrays with an average gain of 9dBi and 11dBi, respectively.

In order to overcome the problem of a complicated feed network manifest in the design of the two-element linear and 2 × 2 planar arrays, an alternative design was proposed. In this design, four radiating elements were electromagnetically coupled to a bottom patch excited by a diagonal feed line. With a VSWR ≤ 1.5 bandwidth of 16%, the maximum variation in the radiation patterns with frequency is 1.7dB. In addition, the small difference between the vertical and horizontal polarized components makes it suitable for dual-linear polarization applications. The measured average gain in both planes is about 9.5dBi.

In the second part of the Thesis, a stacked dual-port antenna with dual-linear polarization characteristics for 3G mobile applications was designed in order to investigate its diversity performance within a broad bandwidth of 8% for the $|S_{11}| \leq -14$dB and having a low isolation of 24dB. From the radiation measurements, it can be observed that the response for the vertical polarization has shown good consistency with the simulation results at the lower, center, and upper frequency of the bandwidth. As for the horizontal polarization, the deviation from the simulation results has occurred only after ±70°. In order to function as a dual-polarized antenna, the difference between the vertical and horizontal polarized components must be smaller than 6dB. The coverage, defined as the angular range where the difference is less than 6dB, has degraded to 100° at the upper frequency due to the distortion of the radiation patterns at the higher angles.

In comparison with the aperture-coupled antenna in [Lin01], the feed network of the stacked antenna is simpler. The analysis was based on the assumption of an ideal antenna under a Rayleigh fading propagation channel. In this Thesis, the influence of the stacked patch antenna design on the cross-polar discrimination χ under non-fading conditions has been examined. It has been found that other than the channel, the antenna design also has a considerable influence on the χ.

The diversity performance of the stacked antenna was evaluated at the lower, center, and upper frequencies of the bandwidth in order to ensure that the antenna functions well as a polarization diversity antenna across the entire bandwidth. The diversity performance has been found to vary across the bandwidth. It has been widely accepted that the full benefits of diversity can be realized with a maximum correlation of 0.7. Across the bandwidth, the measured far-field coupling or orthogonality is less than 0.7 within 107°. The output power correlation, which is dependent on the cross-polar discrimination, is less than 0.7 within 93°. In the analysis, the maximal ratio combining scheme was used. The maximum diversity gain at 1% outage rate (99% reliability) is 11.7dB, which has been found to decrease by 50% with a 20% outage requirement of the system. The antenna is capable of achieving good diversity gain of at least 5dB within an angular coverage of 120° across the entire bandwidth, according to the measured results.

A 2 × 1 linear array was also designed and measurement results have shown that it can achieve a bandwidth of 12.2% for the $|S_{11}| \leq$ -14dB. Within a minimum coverage of 118°, the difference between the vertical and horizontal polarizations is less than 6dB, which makes it suitable to operate as a polarization diversity antenna. The diversity

gain is 8.7dB within a minimum coverage of 107° in the *x-z* plane and 81° in the *y-z* plane, and similar to the stacked element, the diversity performance has degraded at the upper frequency.

In the last part of the Thesis, a gap-coupled polarization diversity antenna was designed to operate at 2.4GHz. However, this design has the drawback of the difficulty to obtain impedance matching as the parameters are very sensitive. In addition, degradation in diversity performance has been experienced at the upper frequency of the bandwidth. An alternative design was proposed which require the dielectric substrate to be suspended above the ground plane. In this design, the bandwidth can be increased with the Q-factor reduced. However, care must be taken to ensure that the advantage of increased bandwidth is not offset by the poorer isolation performance.

The suspended gap-coupled antenna has a broader impedance bandwidth, and the impedance matching can be performed more easily. A prototype was fabricated and measured in order to validate the simulation results. The antenna has shown a broad diversity gain coverage of more than 138°, and at the upper frequency of the bandwidth, the coverage is significantly improved.

From the diversity analysis of the various microstrip antenna designs, it can be seen that a good impedance performance is unable to guarantee a good diversity performance across the impedance bandwidth. The diversity performance is related to the difference between the vertical and horizontal polarized radiated powers across the azimuth, which is subjective to the environment (channel) as well as the antenna design.

REFERENCES

[Aan86] C. K. Aanandan, and K. G. Nair, "Compact broadband microstrip antenna", *Electron Lett.*, vol. 22, no. 20, pp. 1064-1065, Sept. 1986.

[Aan90] C. K. Aanandan, P. Mohanan, and K. G. Nair, "Broad-band gap coupled microstrip antenna", *IEEE Trans. Antennas Propagat.*, vol. 38, no. 10, pp. 1581-1586, Oct. 1990.

[Bra95] P. Brachat, and J. M. Baracco, "Dual-polarization slot-coupled printed antennas fed by stripline", *IEEE Trans. Antennas Propagat.*, vol. 43, no. 7, pp. 738-742, Jul. 1995.

[Bre59] D. G. Brennan, "Linear diversity combining techniques", *Proc. IRE*, vol. 47, pp. 1075-1102, Jun. 1959.

[Cha81] R. Chadha, and K. C. Gupta, "Segmentation method using impedance matrices for analysis of planar microwave circuits", *IEEE Trans. Microw. Theory Tech.*, vol. 29, no. 1, pp. 71-74, Jan. 1981.

[Che01] Z. N. Chen, "Experimental investigation on rectangular plate antenna with omega-shaped slot", *Radio Science*, vol. 36, no. 5, pp. 833-839, Aug. – Sept. 2001.

[Che03] Z. N. Chen, T. S. P. See, and M. Y. W. Chia, "Broadband dual-polarization stacked microstrip antennas for bluetooth applications", *Microw. Opt. Tech. Lett.*, vol. 37, no. 5, pp. 364-366, Jun. 2003.

[Col69] R. E. Collin, and F. Zucker, "Antenna Theory Part 1", Chapter 4, New York: McGraw-Hill, 1969.

[Cro90] F. Croq, and A. Papiernik, "Large bandwidth aperture-coupled microstrip antenna", *Electron Lett.*, vol. 26, no. 16, pp. 1293-1294, Aug. 1990.

[Cro91] F. Croq, and D. M. Pozar, “Millimeter-wave design of wide-band aperture-coupled stacked microstrip antennas”, *IEEE Trans. Antennas Propagat.*, vol. 39, no. 12, pp. 1770-1776, Dec. 1991.

[Cro97] B. P. Crow, I. Widjaja, L. G. Kim, and P. T. Sakai, “IEEE 802.11 wireless local area networks”, *IEEE Commun. Magazine*, vol. 35, no. 9, pp. 116-126, Sept. 1997.

[Cru91] E. M Cruz, and J. P. Daniel, “Experimental analysis of corner-fed printed square patch antennas”, *Electron. Lett.*, vol. 27, no. 16, pp. 1410-1412, Aug. 1991.

[Die00] C. B. Dietrich, “Adaptive arrays and diversity antenna configurations for handheld wireless communication terminals”, *PhD Thesis, Virginia Polytechnic Institute and State University*, 2000.

[Egg93] P. C. F. Eggers, J. Toftgard, and A. M. Oprea, “Antenna systems for base station diversity in urban small and micro cells”, *IEEE J. Select. Areas Commun.*, vol. 11, no. 7, pp. 1046-1057, Sept. 1993.

[Egg98] P. C. F. Eggers, I. Z. Kovacs, and K. Olsen, “Penetration effects on XPD with GSM 1800 handset antennas, relevant for BS polarization diversity for indoor coverage”, *Proc. 48th IEEE Veh. Technol. Conf.*, Ottawa, Canada, pp. 1959-1963, May 1998.

[Gup81] K. C. Gupta, and P. C. Sharma, “Segmentation and desegmentation technique for analysis of planar microstrip antennas, *IEEE Antennas Propagat. Soc. Int. Symp. Digest*, pp. 19-22, Jun. 1981.

[Haa00] J. C. Haartsen, “The bluetooth radio system”, *IEEE Personal Commun. Magazine*, vol. 7, no. 1, pp. 28-36, Feb. 2000.

[Hal80] P. S. Hall, “New wideband microstrip antenna using log-periodic technique”, *Electron. Lett.*, vol. 16, no. 4, pp. 127-128, Feb. 1980.

[Her98] N. Herscovici, “A wide-band single-layer patch antenna”, *IEEE Trans Antennas Propagat.*, vol. 46, no. 4, pp. 471-474, Apr. 1998.

[Huy95] T. Huynh, and K. F. Lee, “Single-layer single-patch wideband microstrip antenna”, *Electron. Lett.*, vol. 31, no. 16, pp. 1310-1312, Aug. 1995.

[Jak74] W. C. Jakes, “Microwave mobile communications”, New York: Wiley, 1974.

[Jam89] J. R. James and P. S. Hall, “Handbook of microstrip antennas”, Chapter 3, London, Peter Peregrinus Ltd., pp. 311-351, 1989.

[Kah54] L. R. Kahn, “Ratio Squarer”, *Proc. IRE*, vol. 42, p. 1704, Nov. 1954.

[Kam97] A. Kamerman, “Spread spectrum schemes for microwave frequency WLANs”, *Microw. Jour.*, vol. 40, pp. 80-90, Feb. 1997.

[Kar01] M. Kar, and P. Wahid, “Two-branch space and polarization diversity schemes for dipoles”, in *Proc. IEEE Antennas Propagat. Soc. Symp.*, vol. 3, pp. 364-367, Jul. 2001.

[Koz84] S. Kozono, T. Tsuruhara, and M. Sakamoto, “Base station polarization diversity reception for mobile radio”, *IEEE Trans. Veh. Technol.*, vol. 33, no. 4, pp. 301-306, Nov. 1984.

[Kum81] G. Kumar, and K. C. Gupta, “Trapezoidal shaped microstrip antennas for wider bandwidth and beamwidth”, *Int. Conf. Commun. Circuits and Sys.*, p. 7, Dec. 1981.

[Kum84] G. Kumar, and K. C. Gupta, “Broad-band microstrip antennas using additional resonators gap-coupled to the radiating edges”, *IEEE Trans. Antennas Propagat.*, vol. 32, no. 12, pp. 1375-1379, Dec. 1984.

[Kum85] G. Kumar, and K. C. Gupta, "Nonradiating edges and four edges gap-coupled multiple resonator broad-band microstrip antennas", *IEEE Trans. Antennas Propagat.*, vol. 33, no. 2, pp. 173-178, Feb. 1985.

[Lee71] W. C. -Y. Lee, "Antenna spacing requirement for a mobile radio base-station diversity", *Bell Syst. Tech. J.*, vol. 50, no. 6, pp. 1859-1876, Jul.-Aug. 1971.

[Lee72] W. C. -Y. Lee, and Y. S. Yeh, "Polarization diversity system for mobile radio", *IEEE Trans. Commun.*, vol. 20, no. 5, pp. 912-923, Oct. 1972.

[Lee73] W. C. -Y. Lee, "Effects on correlation between two mobile radio base-station antennas", *IEEE Trans. Commun.*, vol. 21, no. 11, pp. 1214-1224, Nov. 1973.

[Lee90] R. Q. Lee, and K. F. Lee, "Experimental study of the two-layer electromagnetically coupled rectangular patch antenna", *IEEE Trans. Antennas Propagat.*, vol. 38, no. 8, pp. 1298-1302, Aug. 1990.

[Leg94] H. Legay, and L. Shafai, "New stacked microstrip antenna with large bandwidth and high gain", *Proc. IEE on Microw. Antennas Propagat.*, vol. 141, no. 3, pp. 199-204, Jun. 1994.

[Lem98] J. J. A. Lempiainen, and J. K. Laiho-Steffens, "The performance of polarization diversity schemes at a base station in small/micro cells at 1800 MHz", *IEEE Trans. Veh. Technol.*, vol. 47, no. 3, pp. 1087-1092, Aug. 1998.

[Lin01] B. Lindmark, and M. Nilsson, "On the available diversity gain from different dual-polarized antennas", *IEEE J. Select. Areas Commun*., vol. 19, no. 2, pp. 287-294, Feb. 2001.

[Lot96] F. Lotse, J.-E. Berg, U. Forssen, and P. Idahl, "Base station polarization diversity reception in macrocellular systems at 1800MHz", *in Proc. 46th Veh. Tech. Conf.*, vol. 3, pp. 1643-1646, Apr. 1996.

[Luk98] K. M. Luk, C. L. Mak, Y. L. Chow, and K. F. Lee, "Broadband microstrip patch antenna", *Electron. Lett.*, vol. 34, no. 15, pp. 1442-1443, Jul. 1998.

[Mat02] M. Mathian, E. Korolkewicz, P. Gale, and E. G. Lim, "Design of a circularly polarized 2×2 patch array operating in the 2.45GHz ISM band", *Microw. Jour.*, pp. 280-286, May 2002.

[Oko76] T. Okoshi, Y. Uehara, and T. Takeuchi, "The segmentation method – An approach to the analysis of microwave planar circuits", *IEEE Trans. on Microw. Theory Tech.*, vol. 24, no. 10, pp. 662-668, Oct. 1976.

[Pri85] C. J. Prior, and P. S. Hall, "Microstrip disc antenna with a short-circuited annular ring", *Electron. Lett.*, vol. 21, pp. 719-721, 1985.

[Pro95] J. G. Proakis, "Digital Communications", New York: McGraw-Hill, 1995.

[Pue81a] H. Pues et al., "Wideband quasi-log-periodic microstrip antenna", *Proc Inst. Elec. Eng., MOA*, vol. 128, pp. 159-163, Jun. 1981.

[Pue81b] H. Pues, and A. Van de Capelle, "A simple accurate formula for the radiation conductance of a rectangular microstrip antenna", *IEEE Antennas Propagat. Soc. Int. Symp. Digest*, pp. 23-26, Jun. 1981.

[Raj02] E. Rajo-Iglesias, G. Villaseca-Sanchez, and C. Martin-Pascual, "Input impedance behavior in offset stacked patches", *IEEE Antennas Wireless Propagat. Lett.*, vol. 1, no. 1, pp. 28-30, 2002.

[Rhe74] S. -B Rhee, and G. I. Zysman, "Results of suburban base station spatial diversity measurements in the UHF band", *IEEE Trans. Commun.*, vol. 22, no. 10, pp. 1630-1636, Oct. 1974.

[Sch65] M. Schwartz, W. R. Bennett, and S. Stein, “Communication systems and techniques”, Chapters 9-10, New York: McGraw-Hill, 1965.

[Sch79] D. H. Schaubert, and F. G. Farrar, “Some conformal printed circuit antenna designs”, in *Proc. Workshop Printed Circuit Antennas*, pp. 5.1-5.21, 1979.

[Sha83] P. C. Sharma, and K. C. Gupta, “Analysis and optimized design of single feed circularly polarized microstrip antennas”, *IEEE Trans. Antennas Propagat.*, vol. 31, no. 6, pp. 949-955, Nov. 1983.

[See03] T. S. P. See, and Z. N. Chen, “Diversity performance of a broadband dual-polarized patch antenna”, Submitted to *IEEE Trans. Antennas Propagat.* in May 2004.

[Sin50] G. Sinclair, “The transmission and reception of elliptically polarized waves”, *Proc. IRE*, vol. 38, pp. 148-151, Feb. 1950.

[Smi87] H. K. Smith, and P. E. Mayes, “Stacking resonators to increase the bandwidth of low profile antennas”, *IEEE Trans. Antennas Propagat.*, vol. 35, pp. 1473-1476, 1987.

[Ton97] K. F. Tong, K. M. Luk, and K. M. Lee, “Design of a broadband U-slot patch antenna on a microwave substrate”, *Proc. Asian Pacific Microw. Conf.*, vol. 1, pp. 221-224, Dec. 1997.

[Tsa88] C. H. Tsao, Y. M. Hwang, F. Kilburg, and F. Dietrich, “Aperture-coupled patch antennas with wide-bandwidth and dual-polarization capabilities”, in *Proc. IEEE Antennas Propagat. Soc. Symp.*, vol. 3, pp. 936-939, Jun. 1988.

[Tur95] A. M. D. Turkmani, A. A. Arowojolu, P. A. Jefford, and C. J. Kellett, “An experimental evaluation of the performance of two-branch space and polarization diversity schemes at 1800 MHz”, *IEEE Trans. Veh. Technol.*, vol. 44, no. 2, pp. 318-326, May 1995.

[Vau87] R. G. Vaughan, and J. B. Andersen, “Antenna diversity in mobile communications”, *IEEE Trans. Veh. Technol.*, vol. 36, no. 4, pp. 149-172, Nov. 1987.

[Vau90] R. G. Vaughan, “Polarization diversity in mobile communications”, *IEEE Trans. Veh. Technol.*, vol. 39, no. 3, pp. 177-186, Aug. 1990.

[Ven98] A. Vengadarajan, and A. Ahuja, “Impedance bandwidth characteristics of normal and inverted stacked microstrip patch antenna”, *12th Int. Conf. on Microw. and Radar*, vol. 2, pp. 380-383, May 1998.

[Wah97] U. Wahlberg, S. Widell, and C. Beckman, “The performance of polarization diversity antennas at 1800 MHz”, in *Proc. IEEE Antennas Propagat. Soc. Symp.*, vol. 2, pp. 1368-1371, Jul. 1997.

[Wei98] J. Weitzen, and M. Wallace, “Analysis of diversity performance of space diversity and cross polarization for PCS base stations”, in *Proc. 9th IEEE Int. Symp. on Personal, Indoor and Mobile Commun.*, vol. 1, pp. 293-297, Sept. 1998.

LIST OF PUBLICATIONS

1. Broadband Dual-Polarization Stacked Microstrip Antennas for Bluetooth Applications, *Microwave and Optical Technology Letters*, Vol. 37, No. 5, Jun. 5 2003, pp. 364-366.

2. Design of Broadband Dual-Polarization Stacked Microstrip Antenna for Bluetooth Applications, *8th International Conference on Communications Systems (ICCS)*, Dec. 2002.

3. Design of Dual-Polarization Stacked Arrays for ISM Band Applications, *Microwave and Optical Technology Letters*, Vol. 38, No. 2, Jul. 20 2003, pp. 142-147.

4. Design of Stacked Offset Antenna Arrays for ISM Band Applications, *Microwave and Optical Technology Letters*, Vol. 39, No. 2, Oct. 20 2003, pp. 125-129.

5. Diversity Performance of a Dual-Linear Polarization Stacked Microstrip Antenna, *Asia-Pacific Microwave Conference 2003*, Vol. 3, Nov. 2003, pp. 1840-1843.

6. Diversity Performance of a Broadband Dual-Polarized Patch Antenna, *IEEE Transactions on Antennas and Propagation*, (Submitted in May 2004).

7. Experimental Study on Diversity Performance of a Dual-Linear Polarization Stacked Microstrip Antenna Array, *IEEE Symposium on Antennas and Propagation*, Vol. 4, Jun. 20-25, pp. 4360-4363, 2004.

8. Diversity Performance of a Dual-Linear Polarization Gap-Coupled Microstrip Antenna, *4th International Workshop on ITS Telecommunications*, Jul. 8-9, pp. 237-240, 2004.

9. Diversity Performance of a Suspended Dual-Linear Polarization Gap-Coupled Microstrip Antenna, *IEE Proc. Microwaves, Antennas & Propagation*, (Submitted in Jun. 2004).